Compression Moulding of Randomly-Oriented Strand Thermoplastic Composites: A study of the flow and deformation mechanisms.

Gilles-Philippe Picher-Martel

Doctor of Philosophy

Department of Mechanical Engineering

McGill University

Montréal, Québec

2015-03-24

A thesis submitted to McGill University in partial fulfillment of the requirements of the degree of Doctor of Philosophy

ACKNOWLEDGMENTS

I would like to extend my deepest thanks to Prof. Pascal Hubert, my research supervisor, for the opportunity he provided me, his support and his constructive advices during the last four years. I would also like to thank Dr. Arthur Levy, a former post-doctoral fellow at McGill. My knowledge and expertise in process modelling and numerical methods was greatly improved by our collaboration and active discussions.

This project was made possible with the support of the National Science and Engineering Research Council of Canada (NSERC); the Consortium for Research and Innovation in Aerospace in Québec (CRIAQ); Bell Helicopter; Bombardier Aerospace ; Pratt & Whitney Canada; Hutchinson; Delastek; Avior; the Center for Development of Composites in Québec; the National Research Council's Institute for Aerospace Research and Advanced Manufacturing Technologies Centre; the University of British Columbia; Université du Québec à Trois-Rivières; Université Laval; École de Technologie Supérieure and McGill University. I would like to thank everyone involved for financial, material, equipment supply and technical advices. Pursuing my studies at McGill was also made possible by personal financial support from the Fond Québécois de Recherche Nature et Technologies (FQRNT) and the McGill Engineering Doctoral Award provided by the Vadasz Award Family, I am very thankful to all.

CONTRIBUTIONS OF THE AUTHOR

The work presented in this thesis led to the development of novel experimental characterization methods, models and guidelines to predict the flow and deformation of randomly-oriented strand thermoplastic composites processed by compression moulding. All the work presented in this thesis was performed by the author, with the following exceptions:

Chapter 3 - Quentin Fabien, an intern from France supervised by the author helped with the design of the squeeze flow apparatus used in this study. Dominic Leblanc and Benoit Landry also contributed for the installation and the calibration of the apparatus.

Chapter 5 - Marcus Scaramanga, an Undergraduate Honors Thesis Student supervised by the author performed the design and manufacturing of the friction measurement apparatus used in this study. Jeffica Hannesto performed the calibration and the improvement of the fixture.

Chapter 6 - Dr. Arthur Lévy a post-doctoral fellow at the McGill's Structures and Composites Laboratory provided a training for the COMSOL Multiphysics software and suggested methods to improve stability of the non-linear solver.

ABSTRACT

The compression moulding of Randomly-Oriented Strands (ROS) of pre-impregnated thermoplastic composites is a new process that enables forming of parts with high fibre volume content and relatively high mechanical properties that can compete with metallic alloys. With this process, parts with complex features, such as sharp corners, thickness variations, ribs and holes can be obtained in one single moulding step. This process usually requires very high pressure up to 120 bar and temperature around 400 °C to obtain good quality parts. In order to develop tools and protocols to aid predicting the required pressure and temperature to form complex parts, a deeper study of the governing flow and deformation mechanisms is required. This thesis proposes a four steps investigation of those mechanisms, with a focus on the macroscopic squeeze flow behaviour. This mechanism governs the filling of intricate part features and helps to predict the required pressure to avoid material short shots.

First, an experimental characterization of the squeeze flow of unidirectional (UD) and ROS composites is presented. A simple numerical model was also developed based on existing literature, as a first step to extend the current knowledge on processing of UD thermoplastic composites to ROS. The results showed that current models fail to predict the squeeze flow of both UD and ROS composites under high pressure and large deformation.

Second, an experimental investigation of the flow and deformation mechanisms was performed using X-Ray microtomography. A novel technique using marker strands coated with conductive silver paint was developed and successfully used to qualify and quantify the material evolution during squeeze flow at the meso-scopic and macro-scopic scale. The results were useful to observe and quantify some of the dominant flow and deformation mechanisms.

Third, an experimental characterization of the inter-ply coefficient of friction was performed using an in-house developed testing apparatus. High temperature pull-through tests were performed on UD pre-impregnated plies under representative processing temperature, normal pressures and shear rates. The results showed that the coefficient of friction is highly dependent on the processing conditions and the test method. It increases with shear rate and decreases with applied pressure.

Finally, a finite element model using an original Eulerian-Lagrangian approach was developed to predict the squeeze flow behaviour of ROS composites. A no-slip boundary condition was imposed at the tool platen interface. A smoothed yield stress behaviour was imposed for the composite melt viscosity for numerical implementation. The model was used to determine the material viscosity and yield stress of ROS composites made of different strand sizes. The results were in good agreement with the experimental data obtained for several test cases. Design charts were also generated using the model predictions. These charts provide simple guidelines to predict the pressure required to completely fill a part feature for a given strand size and feature dimensions.

ABRÉGÉ

Le moulage par compression des composites thermoplastiques à bandes orientées aléatoirement est un nouveau procédé qui permet la mise-en-forme de pièces complexes ayant des taux de fibres élevés et de bonnes propriétés mécaniques pouvant rivaliser avec les alliages métalliques traditionnels. Ce procédé permet la mise-en-forme de pièces possédant des formes complexes, tel que des angles droits, des variations abruptes d'épaisseur, des raidisseurs et des trous, le tout en une seule étape de moulage. Ce procédé requiert habituellement une température de mise-en-forme relativement élevé et l'application de pressions élevées. Afin de développer des outils et des protocoles pour aider à prédire les pressions et températures nécessaires à la mise-en-forme de pièces complexes, une étude approfondie des mécanismes d'écoulement et de déformation du matériau est nécessaire. Cette thèse propose une étude en quatre étapes des mécanismes d'écoulement et de déformation, avec une emphase sur le mécanisme d'écoulement sous pression. Ce dernier régit le remplissage des régions complexes des pièces mise-en-forme et aide à prédire les pressions nécessaires pour éviter une mise-en-forme inadéquate et des zones vides.

En premier lieu, une caractérisation expérimentale de l'écoulement sous pression de composites à fibres unidirectionnelles et à bandes orientées aléatoirement est présentée. Un modèle numérique a été développé à partir de la littérature existante, comme première étape dans l'avancement de la connaissance actuelle sur la mise-en-forme des composites étudiés. Les résultats ont démontrés que les modèles existants ne permettent pas de

prédire adéquatement l'écoulement sous pression des composites étudiés sous hautes pressions et grandes déformations.

En second lieu, une étude expérimentale des mécanismes d'écoulement et de déformation à l'échelle macro et méso-scopique a été effectué à l'aide de la micro-tomographie par rayons X. Une nouvelle méthode utilisant des marqueurs constitués de bandes enduites de peinture d'argent conductrice a été développé et utilisée avec succès pour observer et quantifier l'évolution de la méso-structure des composites durant l'écoulement sous pression. Les résultats de l'étude ont été utiles pour observer et caractériser certains des principaux mécanismes de déformation et d'écoulement.

En troisième lieu, une caractérisation expérimentale du coefficient de friction entre les plis a été effectuée à l'aide d'un appareil de mesure développé dans nos laboratoires. Des mesures ont été effectuées sur des pré-imprégné unidirectionnels sous des températures, pressions normales et taux de déformation représentatifs du procédé de mise-en-forme. Les résultats ont démontré qu'il y a une très forte relation entre le coefficient de friction entre les plis, les paramètres de mise-en-forme et la méthode de test. Globalement, celui-ci augmente avec le taux de déformation et diminue avec la pression normale.

Finalement, un modèle par éléments finis utilisant une approche Eulérienne-Lagrangienne a été développé pour prédire l'écoulement sous pression des composites à bandes orientées aléatoirement. Le matériel a été modélisé comme un fluide à seuil d'écoulement et une condition au bord de non glissement a été imposée. La viscosité du matériau a été modélisée par une approximation lissée d'un fluide à seuil, permettant l'implémentation numérique de celle-ci. Le modèle fut utilisé pour déterminer la viscosité équivalente et la limite d'écoulement de composites à bandes orientées aléatoirement avec des bandes de différentes grandeurs. Les prédictions du modèle sont en accord avec les résultats expérimentaux obtenus pour plusieurs cas d'essais. Le modèle a aussi permit d'établir des graphiques d'aide à la conception pour prédire la pression nécessaire au remplissage d'une géométrie, en fonction de la grandeur des bandes utilisés et de la géométrie de la pièce.

TABLE OF CONTENTS

LIST OF TABLES

LIST OF FIGURES

A list of symbols and a list of abbreviations can be found in Appendix A, pages 117-120.

Chapter 1

Introduction

1.1 Introduction

The research and development of new materials and manufacturing techniques for the aerospace industry has two main objectives. First, there is a need to improve the material properties in order to upgrade performance, reliability and security of aircrafts. There is also requirements to reduce the manufacturing and operating costs. Therefore, new high performance lightweight and low-cost structures are needed to further reduce aircraft weight and improve performance.

Composite materials have the potential to fulfill these objectives, and therefore, have gained a lot of popularity in the aerospace sector in the past decades. Composite materials are a combination of two or more materials whose combined performance are improved compared to the individual components. For aerospace applications, they generally consist of aligned continuous carbon fibres impregnated with an epoxy resin matrix. The carbon fibres provide the strength and stiffness and the matrix holds the fibres together and protects against external damage such as impact or environmental degradation. Their high specific properties are therefore making them a good replacement for metallic parts.

Currently aerospace composite structures are mainly processed using autoclaves. This process is costly and long for parts with complex geometries, such as variation in thickness and orientation, corners, holes or rib features. Figure 1.1 shows an example of an existing complex part from the

Airbus A340. The layup is quite complex, requires a lot of ply cutting and stitching, which involves long manufacturing time as well as high costs, and generate waste [1]. Thus, there is a need to develop new manufacturing technologies to reduce the cost and processing time for complex parts.

Figure 1.1: Photograph of an Airbus A340 spoiler assembly. (ref. Composites World [1])

First, the use of a thermoplastic matrix, instead of a commonly used thermoset epoxy matrix, can contribute to reduction of the manufacturing time, since it does not require lengthy cure cycles.

Thermoplastic polymers consist of long chain-like molecules with covalently bonded carbon atoms as the backbone of the chain. They are formed by joining many monomers together by a process called polymerization. They can be in an amorphous or a semi-crystalline phase. Crystalline phase consists of an alignment of the molecules linked together by secondary bonds (Van der Walls, hydrogen or dipole-dipole bonds) leading to an increase in the density and the mechanical properties of the polymer. In terms of processing, one of the biggest differences between thermoset and thermoplastic matrix composites is that thermoplastics have no curing reactions during fabrication; they simply melt.

Thermoplastic composites are then a good candidate to reduce the processing time of complex parts. In addition, they also offer a lot of advantages compared to traditional thermoset composites. They have higher toughness and mechanical properties, a higher service temperature, a better environmental resistance, no curing time and they are recyclable [2-4].

Current applications of thermoplastic composites in aerospace structures are limited to simple components with minimal curvature and thickness variations. This limitation exists because continuous fibre (CF) thermoplastic composites, while exhibiting excellent mechanical performance, are difficult to form. The automotive industry can produce parts with intricate features by injection moulding of Short Fibres (SF) or bulk moulding compounds (BMCs), but their mechanical properties are generally too low for aerospace applications. Recent development showed that preforms with long discontinuous fibres (LDF) and high fibre volume fractions (> 50 %) have the potential for being used in structural components due to their impressive forming and mechanical characteristics [5-8].

Thus far, behaviour of CF composites has been widely investigated and is well understood, whereas studies on LDF composites are limited. LDF material preforms can be categorized based on the form of reinforcement (individual fibres vs. strands) as well as the fibre orientation (aligned vs. random). Figure 1.2 shows the influence of the reinforcement type on the performance and processability, from SF to CF.

Aligned long discontinuous fibre preforms resemble unidirectional plies and can be layered to form a laminate. It has been shown that aligned LDF materials can achieve performance close to that of CF materials [9, 10]. However, the level of complexity that can be achieved with this material is still limited in terms of part curvature and feasible features.

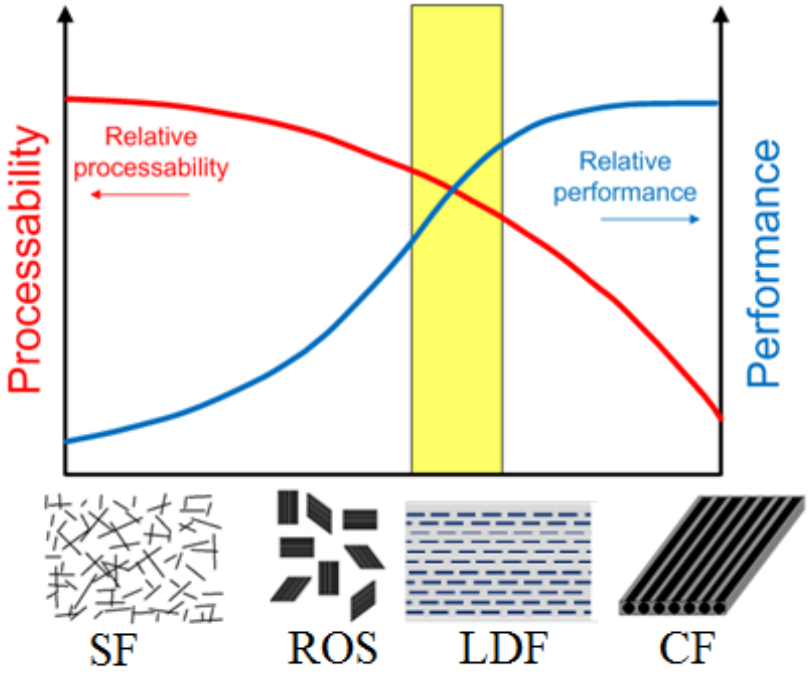

Figure 1.2: Comparison between processability and performance for different reinforcement architecture. (adapted from [9])

Lying between BMCs and LDF preforms, randomly oriented strands of unidirectional prepreg composite tape (ROS), with high fibre volume fractions (>50%), have attractive forming and mechanical characteristics [11-17]. Each strand consists of a chopped piece of pre-impregnated unidirectional (UD) tape. Their dimensions are in the order of the macroscopic scale (5-25mm) compared to small discontinuous fibres that are in the order of the microscopic scale. This discontinuous fibre system is quite new and limited research work has been done on it. On the industry side, recent announcement by aerospace part manufacturers mentioned that "they have successfully advanced the use of thermoplastic composite materials for aerospace structural metal replacement in complex-shape applications previously not suited for composites" [17]. Green, Tweed & Co. can manufacture complex parts using ROS thermoplastic materials processed by compression moulding in a short cycle time. Figure 1.3 shows an example of a complex bracket manufactured using compression moulding of ROS and the previous metallic part.

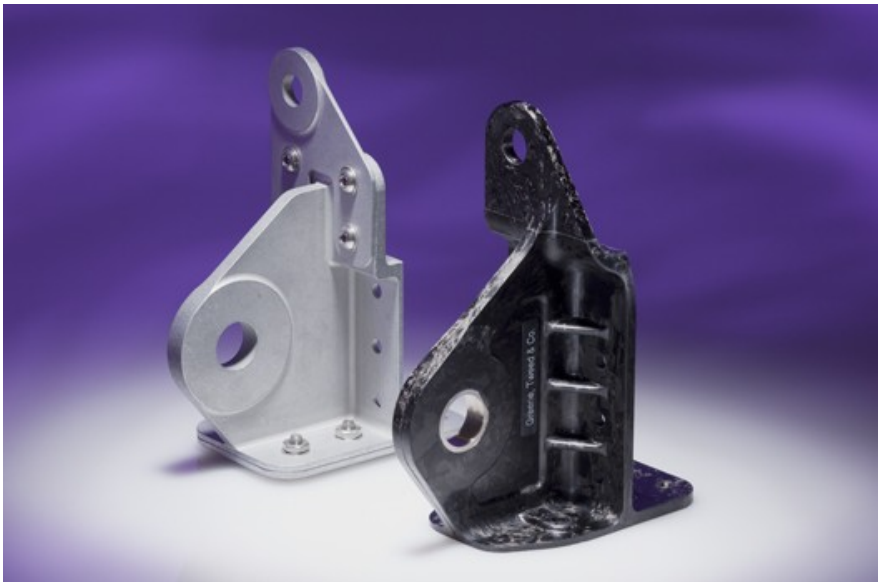

Figure 1.3: Photograph of a complex aerospace part made with ROS and the previous metallic part. (ref. Green, Tweed & Co. [17])

The new part has an equivalent specific stiffness and is lighter. This new process is then quite promising. Next section will provide an overview of the ROS compression moulding process.

1.2 Compression moulding of ROS

In this process, strands of thermoplastic composite pre-impregnated tapes are distributed randomly in a mould cavity. The setup is then placed in a heated press to melt the thermoplastic resin and compressed under high pressure to fully fill the mould cavity and to consolidate the material. Once the part is consolidated, the mould is cooled down and the part is ejected at the desired temperature. Figure 1.4 shows an overview of the compression moulding process of ROS parts. Complex shapes, including corners, thickness variations, ribs or holes, are obtained in one compression moulding step. The final part requires almost no trimming and post-processing. To the best knowledge of the author, this is the most promising processing technique to achieve high performance, complex aerospace parts, and thus, more investigation on the processing science behind this material is required to optimize the process and develop adequate design guidelines.

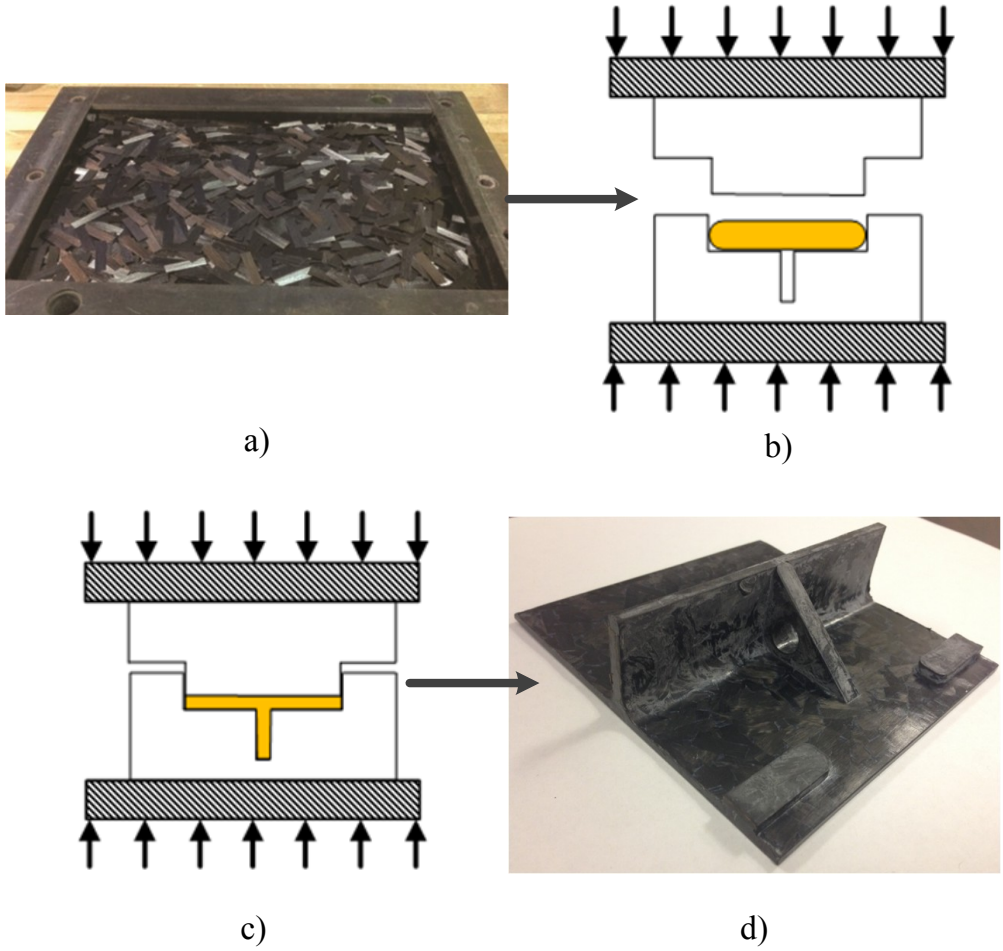

Figure 1.4: Compression Moulding of ROS. a) Chopped strands are randomly distributed in the mould cavity. b) The Mould is closed with a small preload and the heating process starts. c) The material melts, a high pressure is applied and materials flow inside intricate part features. d) The part is cooled-down and demoulded. A net-shape part is obtained with many different features without almost no trimming.

1.3 Problem statement

From the limited work found on this manufacturing technique, it was found that, generally, a high pressure (60-120 bar) is applied to form good quality parts [18, 19]. The high pressure prevents short shots and helps to obtain a good consolidation quality with minimum defects and a low void content, which directly influences mechanical properties. Under the application of heat and high pressure, the material flows and deforms to fill the intricate features of the mould, and then, consolidates. The final quality of the part is directly dependant on these flow and deformation mechanisms. However, there is no guidelines to predict the amount of pressure

required and very limited knowledge on the flow behaviour of ROS. The flow and deformation mechanisms are likely to depend on several factors, including the process parameters, the geometric features and dimensions, and the strand size. Thus, an extensive study of the relationships between these parameters and the dominant flow mechanisms is a logical first step towards a better understanding of this new manufacturing process.

1.4 Outline

The main body of this thesis is divided into seven chapters. Chapter 2 summarizes relevant theory and literature and identifies research areas where investigation is required. Chapter 3 presents an experimental and numerical study of the squeeze flow behaviour of unidirectional (UD) and ROS composites. Chapter 4 presents a novel experimental characterization method using X-Ray microtomography. Chapter 5 presents an experimental study of the inter-ply friction mechanism. Chapter 6 presents the development, implementation and application of a finite element model to predict the squeeze flow of ROS composites. Finally, Chapter 7 concludes and highlights the key contributions of this work. Additional data can also be found in the appendix section.

Chapter 2

Theory and literature review

In this chapter, a concise review of relevant background theory and literature on the processing science related to compression moulding of ROS composites is presented. Since, there is very limited knowledge of the flow and deformation mechanisms governing the processing of ROS composites, a state-of-the-art of the processing science related to thermoplastic (TP) composites that is likely to be applicable, or adaptable to ROS composites is presented. Then, based on the analysis of the existing literature, the governing physical phenomena that are likely to influence the processing of ROS composites are discussed along with the areas that requires investigation.

2.1 Processing of thermoplastic composites

In this section, a review of the main processing methods and governing physical phenomena behind manufacturing of TP composites that are likely to be applicable to ROS composites are discussed. Figure 2.1 provides a summary of the main categories of reinforcement used for TP composites, as well as the most common processing techniques and the governing deformation mechanisms that influence the forming behaviour.

Reinforcement Types	Typical Processing Methods	Governing deformation mechanisms
Continuous Fibres 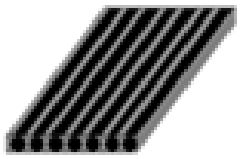	Autoclave 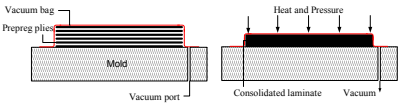 Thermoforming 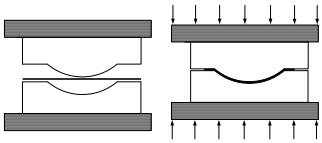 Automated Tape Placement	- Inter-ply friction - Intra-ply shear -Tool-ply friction - Bending - Squeeze flow
Aligned Long Discontinous Fibres 	Autoclave Thermoforming	- Inter-ply friction - Intra-ply shear -Tool-ply friction - Squeeze flow
Randomly-Oriented Strands 	Compression Moulding 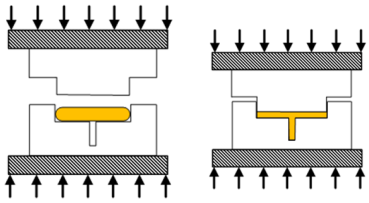	- Squeeze Flow (macro-scopic and meso-scopic) - Packing stress - Inter-ply friction
Short Fibres 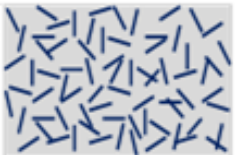	Injection Moulding 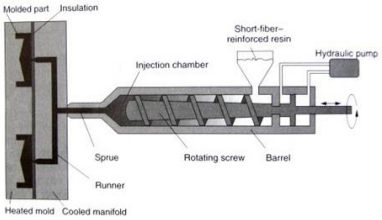 Compression Moulding (SMCs/BMCs)	- Packing stress - Squeeze flow - Fibre-fibre interactions

Figure 2.1: Summary of the different fibre systems, the processing methods and the governing deformation mechanisms.

The following sub-sections will provide a brief review of the processing science behind each categories of reinforcement type, from CF systems to SF systems.

2.1.1 Continuous fibres (CF) system

Generally, CF thermoplastic composites are manufactured either by thermoforming processes or by Automated Tape Placement (ATP). Thermoforming processes are all based on a similar technique. A composite sheet made of continuous fibres is preheated above its melting temperature, put in a tool and draped, and consolidated by the applied pressure and temperature. The consolidation can be obtained by direct action of the mould on the thermoplastic sheet or by the mould combined with vacuum or air pressure (see schematic on Figure 2.1). Usually, the route from prepreg to final component consists of three basic steps: prepreg lay-up, prepreg consolidation and sheet forming. Sometimes, two or all of these steps are combined into a single operation. All of the consolidation techniques for thermoplastic prepregs use sufficient pressure and temperature to squeeze the prepreg plies together to eliminate inter-ply gaps and allow autohesion to occur before the matrix solidifies [20]. The third step consists of forming the consolidated blank into a given shaped component using any thermoforming process. There are several variations of thermoforming process, as reviewed by [5]: mainly Vacuum / Autoclave forming [21, 22], Diaphragm forming [23], Hydro forming [24] and Rubber pad press forming [25], the only difference being the pressure application method, either pneumatic, hydraulic or mechanical. These processes produces CF composites parts with very good mechanical properties, but the geometry is limited to low curvature parts.

Two physical mechanisms that govern CF thermoforming processes have been studied extensively by different authors: the inter-ply friction and the tool-ply friction [26-28]. These mechanisms depend on the fibre architecture, orientation and processing parameters. When the plies are formed in the mould cavity, inter-ply friction restricts the plies to slide on each other and tool-ply friction restricts the outer plies in contact with the mould cavity. If the tool geometry is too complex or the process parameters inadequate, defects such as wrinkles or fibre buckling can occur due to inter-ply friction or tool-ply friction. The inter-ply friction mechanisms are discussed with further details later in the present chapter.

In terms of processing science, finite element (FE) models have been developed by different authors to simulate the forming of CF composites by including the governing phenomena: tool-

part friction, inter-ply friction, wrinkling and fibre buckling. Modelling thermoplastic composites forming involves the simulation of highly anisotropic material subjected to large deformation. Recently, Thije proposed a new non-linear FE formulation to accurately simulate large deformation of highly anisotropic materials [25, 29]. It is a good tool to predict the location of wrinkles during the forming of a pre-consolidated CF thermoplastic composites.

Also, ATP processes have been widely studied for thermoplastic composites. In this process, tape layup and consolidation are obtained simultaneously using a heat source, such as gas torch, and a pressure roller [30]. One of the important phenomenon that occur during ATP is the tape squeeze flow. This mechanism results of the normal pressure applied by the roller that can make the tape spread in the transverse direction, which can cause defects such as gaps and overlaps [31, 32]. This latter mechanism is discussed in the following sections.

2.1.2 Aligned long discontinuous fibres (ALDF) system

To increase the formability of CF thermoplastic prepreg while keeping good mechanical properties, several types of LDF preforms were developed. The first mention of thermoplastic based composites that are reinforced by aligned long discontinuous fibers (ALDF) and have high mechanical properties can be traced back to the late 80's [5]. An example of such material would be an LDF^{TM} (long discontinuous fibers) preform developed by DuPont that consists of aligned LDF such as carbon or Kevlar, and thermoplastic resin such as PolyEther Ether Ketone (PEEK) or PolyEther Ketone Ketone (PEKK).

Most of the literature on LDF is dealing only with mechanical properties, mainly tensile, fatigue and shear properties [9, 10, 33, 34] It was shown that these composites exhibit mechanical properties comparable, but slightly lower, to those of continuous fibre composites. Such performance is attained when fibres are sufficiently long and aligned to achieve maximum reinforcement efficiency, and fibre ends are randomly distributed to avoid formation of resin rich areas [9].

A popular way to produce LDF preforms is introducing slits into a carbon/epoxy prepreg with an automated cutting machine. The effect of different slit parameters (e.g. width, frequency,

stacking, angle) on formability and mechanical properties were evaluated [35, 36]. They also performed experimental studies on the flowability of this material. It was shown that a rib section of good quality can be produced and properties higher than those of SMC can be achieved.

Overall, the governing mechanisms behind this reinforcement system are rather similar to those of CF composites, where inter-ply friction, tool-ply friction and transverse squeeze flow mechanisms play dominant roles.

2.1.3 Randomly-oriented strands (ROS) system

For discontinuous fibre TP composites manufactured using ROS, there is very limited work. Nevertheless, some authors studied similar materials made with a thermoset resin that has already found commercial applications and is available from manufacturers such as Hexcel (HexMC^{TM}). Tuttle *et al.* [7] investigated the effect of material flow on mechanical properties and microstructure of parts produced from HexMC^{TM}. They found that fibres tend to align with the mould boundary, hence changing material properties in that region. Moreover, Feraboli *et al.* [11, 12, 37, 38] conducted a comprehensive study into the properties of composites that were fabricated from strands cut from carbon/epoxy UD prepreg. They studied the effect of strand dimensions on tensile, compressive and flexural properties. They found that its stiffness, compressive and shear strength are comparable to that of quasi-isotropic continuous fibre laminates of the same material. However, its tensile strength is significantly lower and is dependent on the strand aspect ratio.

Van Wijngaarden *et al.* [16] demonstrated applicability of randomly stacked strands of carbon/PEEK for compression moulded parts with complex geometry and thickness variations. However, this study was limited to a simple experimental study, where they made parts using different pressures and analyzed the final part quality.

Recently, authors from Greene, Tweed & Co. demonstrated the applicability of ROS to replace complex metallic parts [39]. Kilic developed a non-linear three dimensional micro-mechanical model to study the mechanical behaviour of ROS thermoplastic composites [40]. They also

studied impact resistance and residual strength after impact of ROS vs. CF composites and they used X-Ray Microtomography to vizualize and characterize the fracture behaviour [41].

Finally, Eguémann also studied the mechanical properties of Carbon/PEEK ROS compression moulded parts. He investigated a case study on a door hinge and also modelled the mechanical properties of ROS. He also investigated the recyclability of ROS thermoplastic parts using a high-voltage fragmentation technique [42].

To the best knowledge of the author, no scholarly literature was found on the study of the governing physical mechanisms behind processing of ROS composites. These mechanisms are discussed later in this chapter based on the review of the existing material systems.

2.1.4 Short fibre system

This last category of discontinuous fibre composites comprises materials fabricated from randomly oriented short fibre suspensions. They are mainly processed either by Injection Moulding, Resin Transfer Moulding (RTM) or by Bulk Moulding Compounds (BMCs). This latter category has been very popular in the automotive industry to manufacture very complex parts with intricate features and the technology and scientific knowledge is quite advanced [43-47]. However, the mechanical properties are too low for aerospace applications and higher fibre volume fraction BMCs are required.

In the injection moulding process, the thermoplastic resin is mixed with SF and injected into the mould using hydraulic pressure. The material has a rheological behaviour close to the viscosity of neat polymers due to the low fibre content. The physical phenomenon involved has been studied by several authors and commercial softwares are already available to simulate the injection moulding process for SF systems.

For compression moulding of concentrated SF suspensions, such as BMCs or Glass Mat Thermoplastics (GMTs), processing is mainly governed by the squeeze flow mechanism [48-51].

They also studied the packing stress of short fibre suspensions and bundle suspensions, the only difference being the aspect ratio between fibre and bundles diameter. Toll and Manson [52, 53]

first developed a model to predict the packing stress of fibre suspensions and this was adapted later for in-plane randomly oriented bundle mats. Also, the effect of the fibre-fibre interactions was studied extensively by Caba [54].

Next section provides deeper explanations and theoretical background on the most relevant mechanisms for ROS composites.

2.2 Overview of the governing deformation mechanisms of ROS

Based on the existing literature presented above on similar materials, an overview of the main governing deformation mechanisms that are likely to influence the forming of ROS composites is discussed in this section. The deformation that the material undergoes during compression moulding is important to understand the material behaviour and to determine the feasibility of the process and the final quality of the part. Based on existing work on the deformation mechanisms encountered in SF and LDF bundle suspensions [55-57], it is assumed that during compression moulding of ROS, the material undergoes three similar deformation modes: packing deformations, meso-scopic transverse deformations and a macro-scopic squeeze flow. This latter mechanism is also intimately linked to the inter-ply shear mechanism.

Figure 2.2 shows a schematic of the governing deformation mechanisms for ROS composites. Initially, the strands are bulked and not compacted. When a pre-load is applied, strands will pack, potentially bend and conform on each other. At this stage, there are gaps between strands that could potentially lead to voids. Then, when the material melts and a high pressure is applied, the melt flows at the macroscopic scale and fills the tool cavity. Also, each strand will undergoes transverse deformation due to the meso-scopic squeeze flow mechanism. This latter mechanism ensures the inter-strand void content reduction. The following sections provide theoretical background on these four dominant mechanisms.

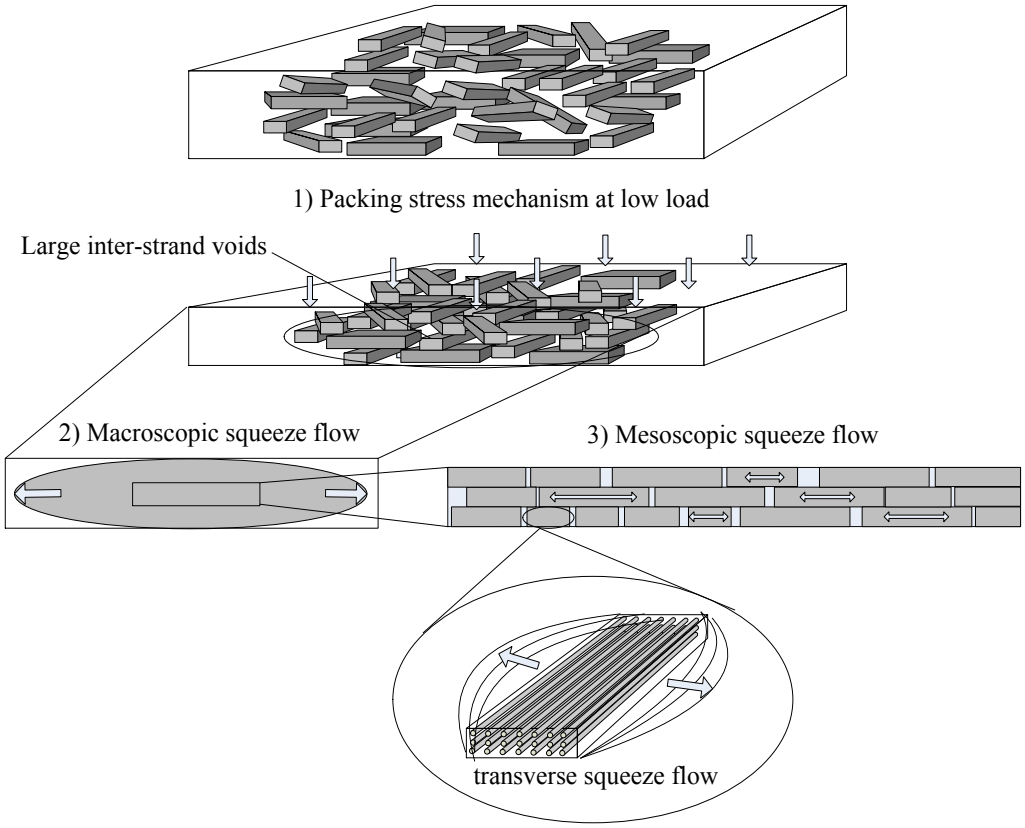

Figure 2.2: Schematic of the governing deformation mechanisms for ROS composites.

2.2.1 The packing stress mechanism

The first mechanism corresponds to an elastic compaction behaviour, denoted as *packing deformation*, at low load. It is mostly associated with the bending and conformation of the strands. It has been studied by many authors for concentrated SF and fibre bundle suspensions. Servais *et al.* [56] suggested an experimental method to measure the packing stress up to 100 kPa (i.e. low normal stress). Luchoo *et al.* [58] simulated the elastic response at the meso-scale. Hereunder, we consider that normal stresses (3-12 MPa) involved when press forming ROS are much higher than the packing stress and that the fibre bed is fully compacted when the material flows. The packing deformation therefore occurs only at very low load during the initial stage of the process and is considered to have negligible effects on the final part quality. Therefore, this mechanism is not taken into account in this study.

2.2.2 The meso-scopic transverse deformation mechanism

The second mechanism corresponds to a flow at the mesoscopic scale of the strand. In this mode, the applied pressure results in a spreading of each strand. With this squeezing, the gaps between strands reduce. This mechanism is denoted as the *inter-strand void content* (ISVC) reduction. These inter-strand voids have to be reduced enough to prevent crack initiation and strength property loss in the final part. This later mechanism has been studied in a recent work by Levy *et al.* [59]. An analytical model to predict the ISVC for ROS flat panels under various processing conditions and strand geometry has been developed. It has been used to predict the void content and final thickness of flat panels manufactured with Carbon/PEEK ROS of different strand size.

2.2.3 The squeeze flow mechanism

The third mechanism corresponds to a flow at the macroscopic scale of the part. At this scale the material can be considered as a homogeneous medium that undergoes a squeeze flow imposed by the closing platens of the mould. Several analytical models and experimental procedures were developed to predict the squeeze flow of UD composites [31, 60] and short fibre bundles for SMC or BMC moulding [57, 61].

The macroscopic squeeze flow plays a dominant role in ROS forming. It rules whether the material flows and fills intricate features of the mould preventing short shots. These areas, such as corners or ribs, may indeed remain empty after the initial operator positioning of the strands in the mould. However, to the best knowledge of the author, no extensive study of that mechanism was performed for ROS. Section 2.3 is entirely dedicated to the squeeze flow mechanism and the relevant theoretical background for this study.

2.2.4 The inter-ply shear mechanism

As discussed previously, the inter-ply shear mechanism plays a dominant role in TP composites processing and it has been studied widely in the past years, mostly to improve the understanding of CF thermoforming processes. Also, the macroscopic squeeze flow behaviour is likely to be influenced by the inter-ply or in the case of ROS, the inter-strand shear mechanism. This mechanism, is governed by the friction coefficient between two plies or strands sliding on each

other. The coefficient of friction, is highly variable for composite materials. It highly depends on the forming process parameters such as temperature, sliding velocity and normal pressure. It also depends on material properties of the fibres and matrix, such as the surface roughness, the reinforcement type such as UD plies or fabrics, as well as the fibre orientation and distribution. Figure 2.3 shows a schematic of the inter-ply shear mechanism for UD plies, where a ply oriented at 90° is pulled through two plies oriented at 0°. For composite materials, the inter-ply friction is quite challenging to measure and predict accurately under representative processing conditions. In addition to the material nature itself, the testing method can greatly affect the coefficient of friction measurements. In fact, several researchers developed different apparatus and techniques to measure and model the coefficient of friction and a lot of variability in the results was found for some materials [62].

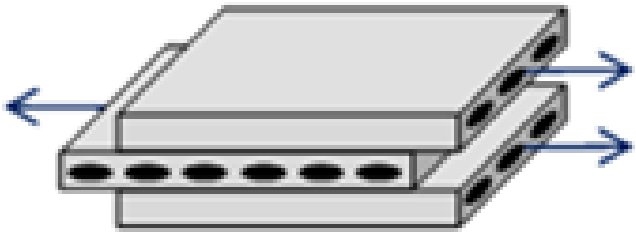

Figure 2.3: Schematic of the inter-ply shear mechanism in composite forming.

This work has been mostly applied to the forming of textile fabrics and UD thermoplastic composites [28, 62, 63]. A lot of achievements were done on the characterization and modelling of the tool-ply friction, which plays an important role in thermo-stamping processes. Recently, a test friction benchmark exercise was performed by several research groups [64]. They compared the results for the coefficients of friction obtained with their different test setup using a benchmark material: a Polypropylene (PP) commingled fabric (Twintex PP). But, to the best knowledge of the authors the effect of the inter-ply friction for ROS composites have not been studied yet. Most of the models were developed with the assumption of elliptical fibre bundles with fabric architecture or UD plies. These models cannot be extended directly for ROS composites, as several assumptions have to be reviewed.

2.3 Squeeze flow of thermoplastic composites

As mentioned earlier, the squeeze flow mechanism plays a dominant role in several thermoplastic forming processes, including SMCs and BMCs, CF systems and ROS composites and this is the main topic of this thesis. The following sub-section extensively reviews the squeeze flow characterization methods and models developed for CF and SF composite materials.

2.3.1 Theoretical background on squeeze flow

The squeeze flow can be defined as a kinematic where a material is deformed between two parallel platens approaching each other at a constant applied force or closure rate [65], as shown in Figure 2.4. It can be used as a rheology method for a wide range of materials, including purely viscous liquids, viscoelastic solids, yield stress fluids and purely elastic solids. Engmaan *et al.* [65] reviewed the major experimental and modelling techniques developed in the past years. Two configurations can be used:

1. A constant material volume between the platens. The platens are larger than the squeezed sample, so the material is constrained between the platens throughout the experiment (see Figure 2.4a)).
2. A constant contact surface between the samples and the platens. The platens gap is initially fully filled with material, so the contact surface remains constant throughout the test (see Figure 2.4b)).

In both cases, the material is placed between the two platens and heated up to desired temperature. Once the target temperature is reached, either a constant load or a constant closure rate is applied and the load evolution or the change in height is measured over time.

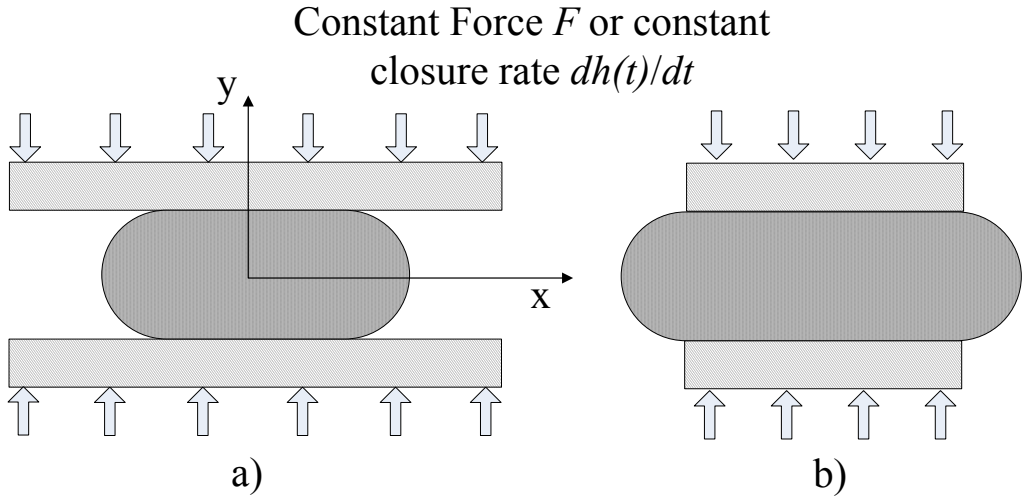

Figure 2.4: Schematic of the squeeze flow test with: a) a constant material volume between the parallel platens b) a constant contact pressure between the parallel platens.

The following sub-section reviews the experimental and modelling work that has been done on the squeeze flow of CF systems and SF systems.

2.3.2 Squeeze flow of CF thermoplastic composites

For continuous fibre reinforced thermoplastic materials, the squeeze flow test is often used to characterize the deformation occurring during processing. Different authors [60, 66, 67] considered UD fibre reinforced composites as a homogeneous continuum medium with an effective bulk transverse shearing viscosity η.

UD fibre composite melts are assumed to behave as an incompressible anisotropic viscous fluid. Indeed, the flow occurs solely in the direction transverse to the fibres, since the inextensible fibres are considered to restrict flow in their direction (see transverse Squeeze Flow on Figure 2.2). The flow is therefore two dimensional. Because the platen gap is usually an order of magnitude smaller than the sample width, lubrication assumption holds, and the two dimensional problem can be reduced to a one dimensional equation. Under these assumptions, the Stokes equation can easily be reduced and solved numerically to predict the sample height evolution as a function of time. The main difference between the different models is how the viscosity is defined.

Thermoplastic polymers are known to behave as a non-Newtonian, shear thinning, viscous fluid [60]. The Carreau viscosity model is well known to describe this shear thinning behaviour [68].

$$\eta = \eta_0[1 + (\lambda\dot{\gamma})^2]^{(n-1)/2} \tag{2.1}$$

where η_0 is the zero shear rate viscosity, n is the shear thinning exponent and λ is the relaxation time. The Carreau viscosity model was often used to model the rheological behaviour of UD thermoplastic composites. This equation is used in the development of the numerical model of Chapter 3.

2.3.3 Squeeze flow of short fibre suspensions

Authors found that the squeeze flow of short fibre suspensions is mainly governed by direct frictional and lubricated contacts between the fibres [54, 55]. The fibres usually have a high length to diameter ratio and can be considered in-plane. When the fibre mat is compressed, fibres tend to bend, slide and potentially deform [56]. These fibre-fibre interactions have been studied by many authors. Servais et al. found that three different forces occurs at the contact points, an elastostatic normal force F_n, a Coulombic friction force F_t and an hydrodynamic lubrication component F_h, due to the thin fluid layer between the impregnated fibres [55]. Figure 2.5 shows a schematic of the fibre-fibre interactions in short fibre bundle suspensions.

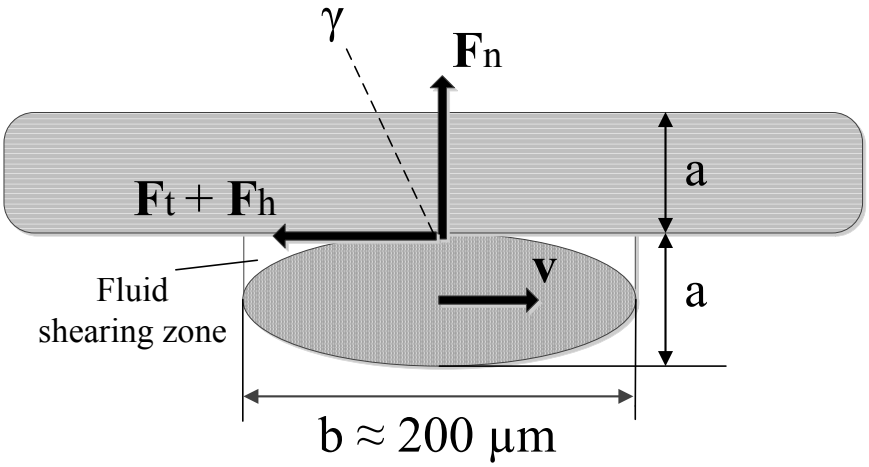

Figure 2.5: Schematic of the fibre-fibre interactions in dispersed fibre bundle suspensions. (adapted from **[55]**)

Squeeze flow experimental test results have also shown that concentrated short fibre suspensions and long fibre suspensions can be considered as yield stress fluids [57]. The squeeze flow test has been used to characterize yield stress fluids and to develop several constitutive relations. Thus, a brief review of relevant background on the squeeze flow of yield stress fluids is provided in the next sub-section.

2.3.4 Squeeze flow of yield stress fluids

Viscoplastic or yield stress materials can be considered either as elastic or rigid solids for low stress levels, whereas over a critical value of stress, named the yield stress τ_Y, they flow with a viscosity that depends on the local shear rate. In the general case, there may be solid-like areas (unyielded regions) of material that are either attached to rigid boundaries or convected by adjacent flowing material with a stress level above the yield value. In some cases, a yield stress material can flow and deform throughout its whole domain, if the stress is everywhere above the yield stress, or it may not flow at all, if the stress is everywhere below this value [69-74]. Figure 2.6 shows a general viscoplastic case where the material is deformed between two parallel platens. Some areas, in gray, where the stress is higher than τ_Y are flowing and some regions, in yellow, where the stress level is lower than τ_Y are rigid.

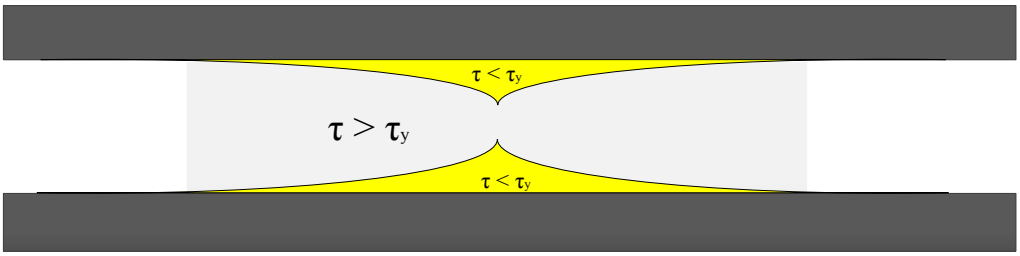

Figure 2.6: General viscoplastic material. Areas in yellow are solids, the stress value is below the yield stress. Areas in gray are flowing, the stress level is higher than the yield value.

Viscoplastic materials are often referred to as *Bingham Plastics* after Bingham [75] who was the first in 1919 to describe paints using a yield stress definition. Many constitutive relations have been developed to model the viscosity of viscoplastic materials. The most common viscoplastic models are the Bingham model, the Herschel-Bulkley model and the Casson model [75-77]. Mitsoulis [72] reviewed the different models and several benchmark problems of viscoplastic

flows. The following equations are respectively the Bingham, the Herschel-Bulkley and the Casson model in tensor form:

$$\begin{aligned} \bar{\bar{\tau}} &= \left(\mu + \frac{\tau_Y}{\left|\bar{\bar{\dot{\gamma}}}\right|}\right)\bar{\bar{\dot{\gamma}}} \qquad for\ \ |\bar{\bar{\tau}}| > \tau_Y \\ \bar{\bar{\dot{\gamma}}} &= 0 \qquad for\ \ |\bar{\bar{\tau}}| \leq \tau_Y \end{aligned} \tag{2.2}$$

$$\begin{aligned} \bar{\bar{\tau}} &= \left(K\left|\left|\bar{\bar{\dot{\gamma}}}\right|\right|^{n-1} + \frac{\tau_Y}{\left|\bar{\bar{\dot{\gamma}}}\right|}\right)\bar{\bar{\dot{\gamma}}} \qquad for\ \ |\bar{\bar{\tau}}| > \tau_Y \\ \bar{\bar{\dot{\gamma}}} &= 0 \qquad for\ \ |\bar{\bar{\tau}}| \leq \tau_Y \end{aligned} \tag{2.3}$$

$$\begin{aligned} \bar{\bar{\tau}} &= \left(\sqrt{\mu} + \sqrt{\frac{\tau_Y}{\left|\bar{\bar{\dot{\gamma}}}\right|}}\right)^2 \bar{\bar{\dot{\gamma}}} \qquad for\ \ |\bar{\bar{\tau}}| > \tau_Y \\ \bar{\bar{\dot{\gamma}}} &= 0 \qquad for\ \ |\bar{\bar{\tau}}| \leq \tau_Y \end{aligned} \tag{2.4}$$

In the above expressions, $\bar{\bar{\tau}}$ is the shear stress, μ is a constant plastic viscosity, K is the consistency index and n is the power law index. $\left|\bar{\bar{\dot{\gamma}}}\right|$ is the magnitude of the symmetric rate-of-strain tensor.

The main challenge in solving a viscoplastic flow problem is that all the theoretical models presented above are discontinuous at τ_Y. In the late 80's, Papanastasiou [71] proposed a modification of the Bingham model with an exponential stress-growth term. This model smoothes the ideal discontinuous Bingham viscoplastic model and converts it to a purely viscous one, which is much easier to implement and solve numerically.

$$\eta_{eq} = \eta_0(1 + (\lambda\dot{\gamma})^2)^{\frac{(n-1)}{2}} + \frac{\tau_Y\left(1 - e^{-m\dot{\gamma}}\right)}{\dot{\gamma}} \tag{2.5}$$

This viscous behaviour is highly non-linear and needs numerical methods such as Newton-Raphson algorithms to solve the flow problems. For the squeeze flow of a Bingham fluid, the

deformation that the material undergoes is rather high and one also needs to account for mesh large deformations.

Finally, based on this concise review of the state-of-the art on processing of thermoplastic composites, several gaps in the knowledge for ROS composites have been identified and are discussed in the following sub-section.

2.4 Desired expansion of knowledge

This literature review leads to several conclusions about the applicability of the existing knowledge on the processing of UD and SF thermoplastic composites to ROS composites. Due to the novelty of this material, very limited scientific work has been done on the processing of ROS composites, and several gaps exist in the literature and are highlighted hereunder.

To the best knowledge of the author, **no extensive characterization of the squeeze flow mechanism has been done for ROS Carbon/PEEK composites**. The chopped strands large aspect ratio and the heterogeneity of the material leads to complex flow mechanisms that were not studied in the literature A deeper understanding of the flow behaviour will help the development of predictive models and design guidelines. Therefore, a first natural step is to study this mechanism for representative pressures and processing temperatures. The squeeze flow test method can readily be adapted and is used to characterize ROS composites.

Several models were developed to predict the squeeze flow of composite materials with different types of reinforcement architecture. However, **there is very limited knowledge on the applicability of existing models for ROS composites, and therefore, the assumptions have to be reviewed and adapted.** So, there is a need to investigate the physical phenomenon governing compression moulding of ROS composites, using a combination of both experimental methods and numerical tools, in order to adapt previous models based on realistic assumptions.

Moreover, **the effect of the governing processing parameters, namely the applied pressure, the temperature, the dwell time as well as the strand size has not been systematically**

studied. So, a parametric study should be performed to quantify the effect of the key parameters and identify the critical parameters governing the flow behaviour.

Globally, **there is a need to develop new experimental methods and modelling tools for ROS processing analysis** due to the lack of scientific knowledge on this material.

A summary of the existing knowledge and the desired expansion of knowledge is presented in Table 2-1.

Table 2-1: Existing knowledge and desired expansion of knowledge

Existing knowledge
1. Squeeze flow of UD composites model.
2.Yield stress fluid models.
3.Squeeze flow of BMCs model.
Desired expansion of knowledge
1. Characterization of the macroscopic squeeze flow of ROS.
2. Determination of a suitable viscous behaviour for ROS.
3. Effect of the dominant processing parameters on the squeeze flow of ROS.
4. Effect of the strand size on the flow mechanism.
5. New experimental methods and modelling tools for ROS processing analysis.

2.5 Thesis objective and outline

With the increasing interest in ROS composites and the lack of detailed literature and predictive tools for the governing flow and deformation mechanisms, the overall objective of this thesis is to develop models and guidelines to predict the dominant flow and deformation mechanisms of ROS composites processed by compression moulding.

The proposed objectives were accomplished through the research work presented in the following four chapters that follow a building-block approach:

- Chapter 3 presents a characterization of the squeeze flow mechanism through experimental and modelling efforts. It shows a comparison with UD thermoplastic composites and highlights the limitations of current models.
- Chapter 4 proposes a novel X-Ray microtomography method to characterize the flow and deformation mechanisms occurring during the forming of ROS composites.
- Chapter 5 presents an experimental characterization of the inter-ply coefficient of friction for UD Carbon/PEEK composites under representative processing conditions.
- Chapter 6 combines the extended knowledge of Chapter 3 to 5 and proposes the development, implementation and application of a new model to predict the squeeze flow of ROS flat geometries. A parametric study for different strand size and applied pressure was also performed and design guidelines were developed using the predictive model.
- Chapter 7 finally highlights the main contributions of this research work and discusses potential research areas that would require further investigation

Figure 2.7 provides a flow chart outline of the thesis. A building-block approach is used to extend the current knowledge and implement it in a predictive model for the squeeze flow of ROS composites.

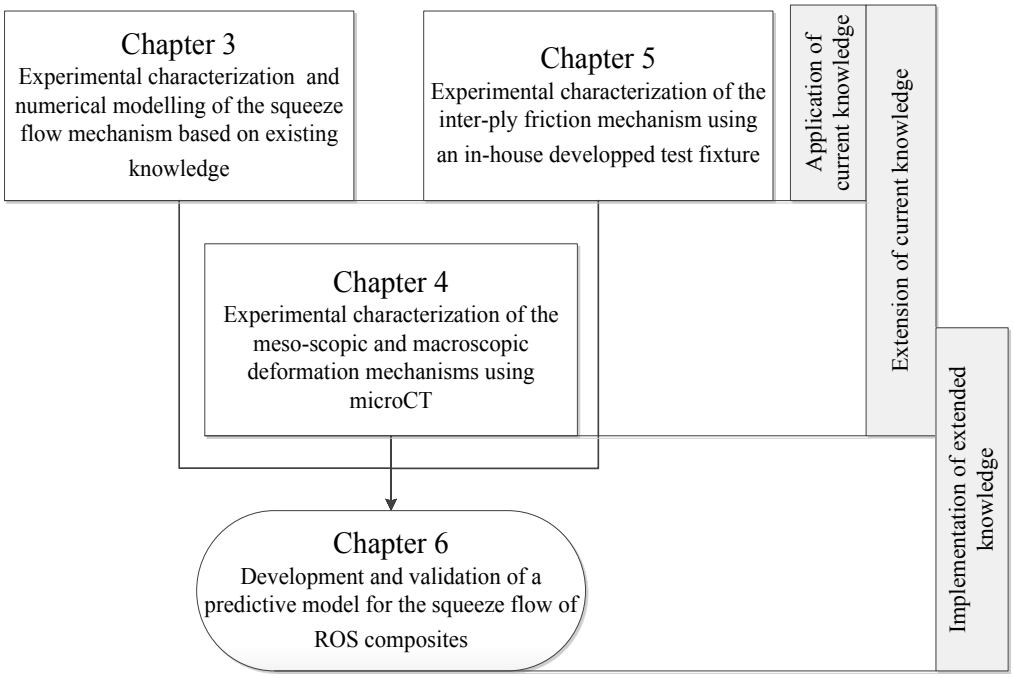

Figure 2.7: Flowchart outline of the thesis.

Chapter 3

A study of the squeeze flow of unidirectional and Randomly-Oriented Strand composites

3.1 Introduction

When processing ROS composites complex parts, the material flows and deforms according to several mechanisms as described in Chapter 2. The ROS composite melt flows at the macroscopic level and fills intricate features of the mould, but also each of the strands, consisting of pieces of UD prepreg, also flows and deforms at the meso-scopic scale.

As a first natural step towards a deeper understanding of the macroscopic and mesoscopic deformation mechanisms for ROS, squeeze flow tests were performed on both UD and ROS composite flat panels. An instrumented hot-press was developed to perform the tests under controlled representative processing conditions. An extensive study for different strand size and pressure level was also performed. The available knowledge on the squeeze flow of UD composites was implemented in a numerical model to verify the applicability to ROS composites.

3.2 Objectives and structure

This chapter has two concurrent objectives, first characterize experimentally the macroscopic squeeze flow of ROS composites using different strand size in order to quantify and qualify the material behaviour. But also, to apply the current theoretical knowledge on the squeeze flow of UD Carbon / PolyEtherEtherKetone (PEEK) composites and verify its applicability to the development of a predictive model for ROS. This helps to establish proper realistic assumptions for ROS composites

The following sections describe the experimental methods, the modelling approach, a summary of the results and discussion of the key findings and limitations of the current model.

3.3 Experimental methods

3.3.1 Material

The material used in this study is a Carbon / PEEK pre-impregnated composite. It consists of AS-4 UD Carbon fibres impregnated by a PEEK matrix. 150 mm wide tape was used to manufacture the continuous fibre samples. ROS samples were manufactured using chopped strands of the same pre-impregnated tape. It was supplied already cut at the desired width and length. The fibre volume fraction is 60% for both materials. The consolidated ply thickness is 0.136 mm. The manufacturer's recommended consolidation temperature is between 370 and 400°C. Figure 3.1 shows a photograph of 25.4 mm long by 6.35 mm wide strands. Table 3-1 summarizes the material properties for the AS-4 Carbon fibres and the neat PEEK resin.

Figure 3.1: Photograph of the 25mm long by 6.35 mm wide strands used in this study.

Table 3-1: Summary of Carbon/PEEK material properties

Material properties	Carbon Fibres	Neat PEEK matrix
Fibre Volume Content (%)	60	40
Average ply thickness (mm)	0.135	0.135
Melt Temperature (°C)	-	343
Glass Transition Temperature (°C)	-	144
Recommended Processing Temperature (°C)	-	370-400
Density (g/cm^3)	1.6	1.3

3.3.2 Instrumented hot-press

A specific instrumented hot press was designed (Figure 3.2). The fixture consists of a custom built miniaturized heated press. Additional details on the setup and engineering drawings can be found in Appendix B. The testing section consists of two H13 steel platens (100 mm x 100 mm) heated using four 500 W cartridge heaters from Watlow. Cartridges are 127 mm long, they have a diameter of 9.42 mm and their heat flux is 16.74 W/cm^2 One type-K thermocouple is used to independently control the temperature of each platen. The platens temperature are controlled with a Watlow SD series Proportional-Integral-Derivative (PID) temperature controller. A cooling system using compressed air is also used to cool down the fixture quickly after each test. The apparatus is mounted into a 250 kN Mechanical Testing System (MTS) servo hydraulic testing machine that allows control of the applied compression force. The relative displacement between the two hot-press platens, and thus, the sample height evolution is measured using the MTS transducer during the whole squeeze flow test.

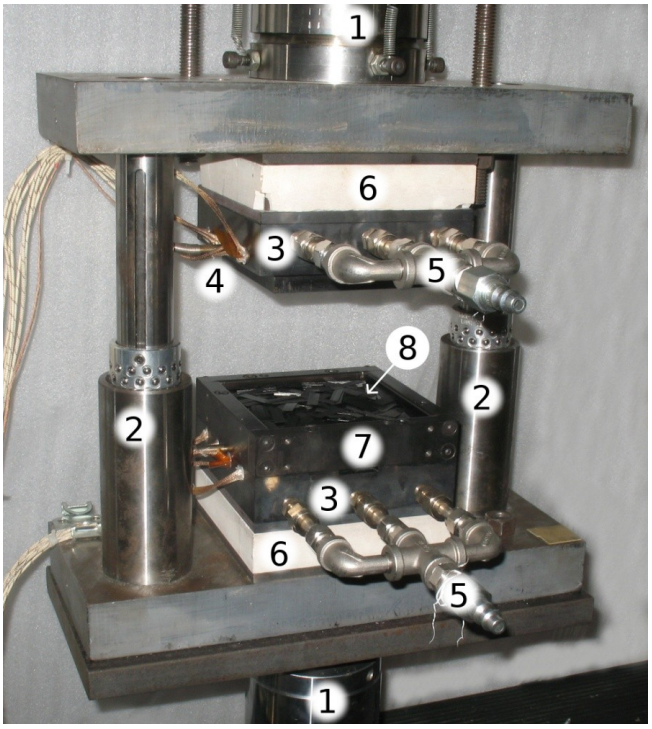

Figure 3.2: Instrumented hot press. (1) MTS compressive fixture. (2) Ball-bearing die set to ensure alignment. (3) H13 steel 100mm x 100mm platens (4) 500W Heating cartridges. (5) Cooling channels using compressed air. (6) Ceramic layer to ensure thermal insulation. (7) A picture frame can be used to pre-consolidate flat panels. (8) Material placed inside the mould.

3.3.3 Test procedure

One UD $[0^o]_{42}$ and four ROS preconsolidated flat laminates were used to perform all the squeeze flow tests presented in section 3.4. This ensured that consolidation effects at low load (packing stress) and ISVC mechanisms, discussed in Chapter 2, were not observed during the experiments, but only the macroscopic squeeze flow behaviour. Both the UD and ROS samples used in this study were cut from 150 mm by 150 mm flat panels pre-consolidated by compression moulding. The laminates were made using a steel tool with a 150x150 mm cavity. Engineering drawings with detailed dimensions of the mould can be found in Appendix C.

For UD laminates, 42 plies of UD tape were stacked inside the cavity of the mould to reach an average consolidated thickness of 6.0 ± 0.1 mm. 250 g of chopped strands was used for each ROS laminates, to reach an average thickness of 6.5 ± 0.2 mm (see Figure 3.2). Strands were added to the mould in small batches and shuffled manually each time to ensure random distribution and minimize their out-of-plane orientation. Then, the mould was closed and placed into a Wabash 100 Tons hot press preheated to 395°C. A thermocouple was placed into a hole on the side of the mould to measure and monitor the plate temperature during the cycle. A pressure of 22 bars was then applied and maintained during 15 minutes. The mould was then cooled down to 70°C at an approximate rate of 12°C/min and was removed from the press. Figure 3.3 shows the processing cycle used to manufacture all the pre-consolidated panels of this study. The panels were trimmed and 50mm x 50mm samples were cut using a diamond blade saw.

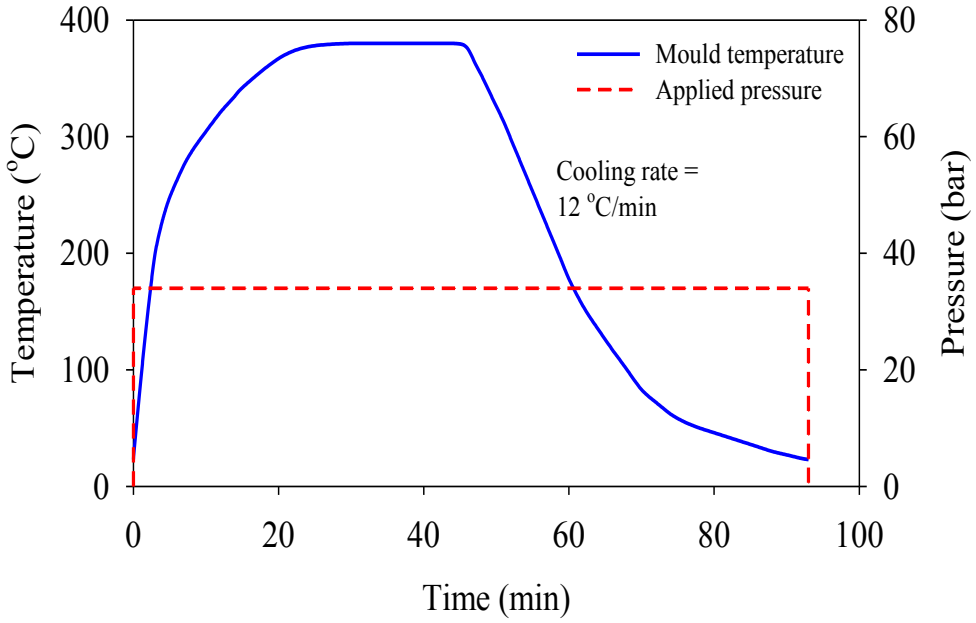

Figure 3.3: Processing cycle used to manufacture all the pre-consolidated panels

The squeeze tests were all performed at 400 °C on the pre-consolidated 50 mm square samples. The instrumented hot-press platens were coated with FREEKOTE 700-NC release agent before each tests to prevent material sticking to the platens and ease demoulding. The samples were centered on the bottom platen and the upper platen was moved down until a contacting force was measured. The MTS machine was set in force control mode. The contacting force (90 N) was low compared to the applied force during the test (1 to 20 kN), preventing flow during the heating phase. The platens were then heated to 400°C in about 15 min. Force control allowed for a compensation of the thermal expansion of the setup. An additional stabilization time of 10 min ensured isothermal conditions during the tests. A closing force according to the test matrix given in Table 3-2 was then applied in a one second ramp and maintained during 5 min. The press was cooled down using compressed air. The cooling rate was not controlled, but measured to be approximately 15°C/min. Finally, when the temperature dropped below 143°C, which corresponded to the glass transition temperature of PEEK, the press was opened and the sample ejected. Sample length, width and thickness were measured prior and after each squeeze flow test, using a micrometer and caliper.

Four different strands size were tested, and four different load levels were used for each strand size (see Table 3-2). The load levels were such that the material remained inside the press platens, ensuring a constant volume experiment, during the whole squeeze flow test.

Table 3-2: Experimental Test Matrix.

Material	Strand length (mm)	Strand width (mm)	Applied Load (kN)
Large strands	25.4	6.35	1, 5, 10, 20
Medium wide strands	12.7	6.35	1, 5, 10, 20
Medium slender strands	12.7	3.18	1, 5, 10, 20
Small strands	6.35	3.18	1, 5, 10, 20
UD	-	-	1, 2.5, 5, 10

3.3.4 Data acquisition

Force and relative displacement signals were acquired, at a rate of 10 Hz, during the whole test. The MTS machine transducer provided the absolute distance between the MTS platens during the tests. The actual sample height evolution *h(t)* was obtained by compensating for the material and fixture thermal expansion. Figure 3.4 shows a two dimensional schematic of the sample placed between the instrumented hot-press platens prior and after the squeeze flow test. The initial sample height h_i and the final sample height h_f were measured at room temperature using a micrometer, prior and after the squeeze flow test.

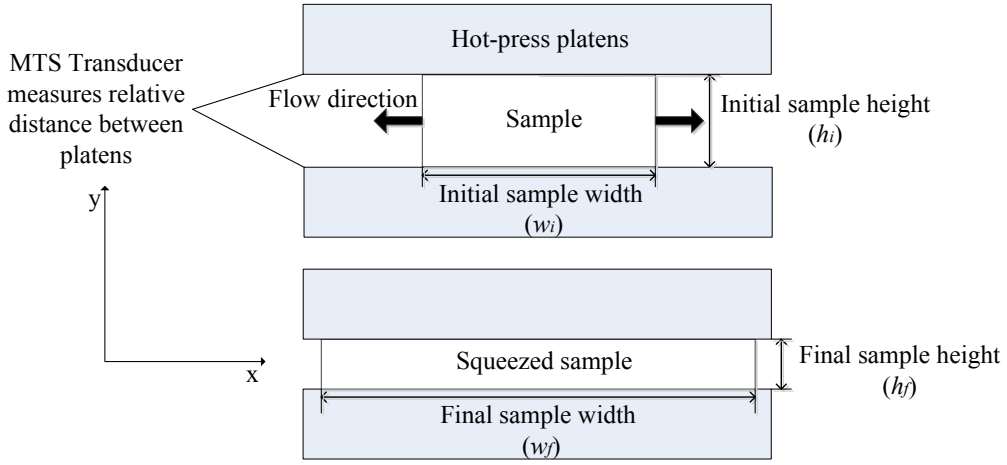

Figure 3.4: Schematic of the sample height evolution measurements during the squeeze flow test. The MTS transducer provides the relative distance between the MTS platens and is used to calculate the absolute sample height reduction throughout the squeeze flow tests.

Because of the thermal expansion of the material between room and processing temperature, corrections had to be performed. ε_{yy}^{th} is the out-of-plane (y-direction) thermal strain of carbon/PEEK composites at processing temperature (400°C). Due to the out-of-plan material thermal expansion, the final height of the specimen at processing temperature h_f^{400} is:

$$h_f^{400} = h_f\left(1 + \varepsilon_{yy}^{th}\right) \tag{3.1}$$

ε_{yy}^{th} was measured at 8% using a TA instruments Q400 thermomechanical analyzer on a quasi-isotropic laminate made of carbon/PEEK UD plies. This value for the out-of-plane thermal strain was supposed to be similar for UD and ROS specimens (transverse behaviour).

The sample final height at processing temperature h_f^{400} was used to offset the acquired relative displacement measurement and obtain absolute height change data. The final height was measured for every sample and compared to the initial height h_i to obtain the final strain ε_f:

$$\varepsilon_f = 1 - h_f/h_i \tag{3.2}$$

3.3.5 Hot-press compliance correction

Also, for tests under loads above 2kN, one has to account for the press compliance to compensate for the tool deformation component in the relative displacement measurements.

Indeed, when the contacting force is increased, the test fixture parts start to deform due to compressive stresses. The deformation was measured at processing temperature by applying different load levels on the hot-press platens, without any samples, to measure purely the steel deformation. A third order polynomial regression was fitted on the experimental data to provide the required displacement compensation d (mm) as a function of the applied load F (N).

$$F = -24.47d^3 + 84.71d^2\ 12.89d \tag{3.3}$$

It means, that for a load level of 20kN, the fixture deformation was about 0.45mm, which was non-negligible compared with the sample height (around 6.5mm). The relative displacement signals were then corrected with the required compensation calculated using equation (3.3).

3.4 Numerical model

As a first step to verify the applicability of current knowledge on squeeze flow of CF composites to ROS composites, only the squeeze flow of UD composites was modelled in this study. As introduced in Chapter 2, section 2.3.2, the model by Shuler and Advani [60] is adapted for a constant material volume configuration. The following sub-sections describe the model assumptions, development and numerical implementation.

3.4.1 Squeeze flow under lubrication assumption

The following assumptions were considered in this model; they were adapted for a constant material volume configuration instead of a constant contact pressure condition [60]:

- UD Carbon/PEEK composites were assumed to behave macroscopically as incompressible anisotropic viscous fluids where there is no flow in the fibre direction. This is well known in the literature and was verified by experimental evidence.
- The material volume was considered constant during the whole experiments, so there was no material flowing outside of the test platens.
- The edges are free, no external force was applied on the sample edges.
- A no-slip boundary condition was imposed on the tool platens.

- The squeeze flow rates were assumed slow enough to neglect inertia effects.

Also, creeping flow conditions can also be considered. The criterion used to qualify creeping flow was the Reynolds number, Re, defined as:

$$Re = \frac{\rho * (dh(t)/dt) * h(t)}{\eta} \tag{3.4}$$

where ρ is the fluid density, $dh(t)/dt$ is the platens closure rate, $h(t)$ is the sample height at a given time and η is the fluid viscosity. A Reynolds number below one indicates creeping flow. This condition was verified for all squeeze flow tests performed in this study.

With respect to these assumptions, transverse squeeze flow of UD composites can be considered as a two-dimensional hydrodynamic lubrication system, with the following pertinent Stoke equation in the *x*-direction:

$$-\frac{\partial P(x)}{\partial x} + \eta\left(\frac{\partial^2 V_x(x,y)}{\partial x^2} + \frac{\partial^2 V_x(x,y)}{\partial y^2} + \frac{\partial^2 V_x(x,y)}{\partial z^2}\right) \tag{3.5}$$

where $P(x)$ is the pressure along the x-direction and $V_x(x,y)$ is the horizontal velocity component.

Under lubrication assumption the vertical component of the velocity is neglected versus its horizontal *x* coordinate $V_x(x,y)$. The velocity derivative versus the *x* dimension can also be neglected compared to its *y* derivative. The pressure field *P* can be considered constant through thickness in the *y* direction. Equation (3.5) then reduces to:

$$\frac{\partial P(x)}{\partial x} = \eta \frac{\partial^2 V_x(x,y)}{\partial y^2} \tag{3.6}$$

where η is the viscosity of the UD composite melt, that can be modeled using the Carreau law (see equation (2.1), section 2.3.2).

3.4.2 Geometry and boundary conditions

Figure 3.5 shows the numerical model geometry and boundary conditions for the squeeze flow of UD Carbon/PEEK composites.

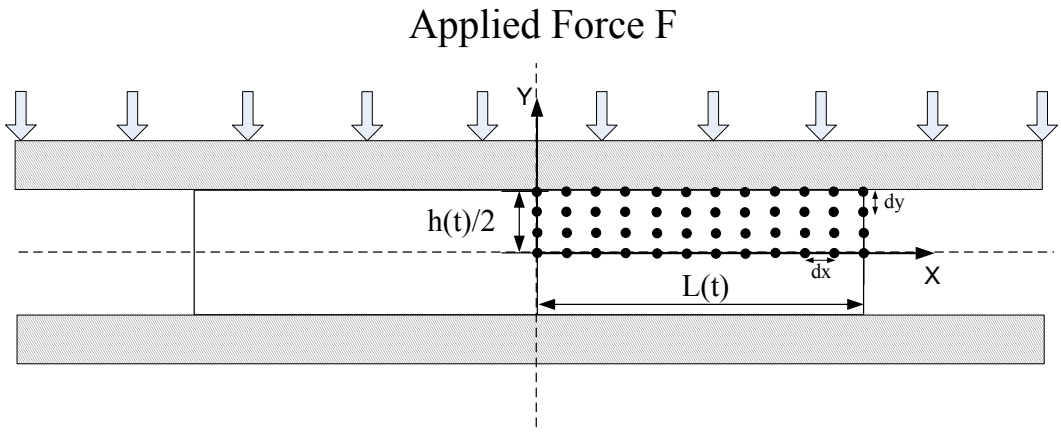

Figure 3.5: Squeeze flow model for UD composites: geometry, numerical discretization and boundary conditions. Arrows represents the distributed load applied by the moving hot-press platen. One quarter of the sample was modelled using the problem symmetry.

As for the boundary conditions, according to previous experimental work [15], no slip conditions are imposed at the platen interface:

$$V_x(x,y) = 0 \qquad at\ y\ =\ h(t)/2 \tag{3.7}$$

Using symmetries, only one quarter of the geometry is modelled, and at y = 0:

$$\frac{dV_x(x,y)}{dy} = 0 \tag{3.8}$$

The closure force *F(t)* equates the pressure *P(x)* integral over the platen surface:

$$F(t) = \int_0^{2L}\int_0^{W} P(x)dxdz = 2W\int_0^{L} P(x)\,dx \tag{3.9}$$

The effective pressure P_{eff} is also defined based on the sample area evolution:

$$P_{eff} = \frac{F(t)}{L(t)W} \tag{3.10}$$

Finally, the sample volume is assumed constant due to material incompressibility, such that:

$$L(t) = \frac{h_i L_i}{2h(t)} \tag{3.11}$$

where L_i and h_i are respectively the initial sample length and height. Considering a control volume between the vertical planes at coordinate 0 and *x*, incompressibility also gives:

$$\int_0^x \frac{dh(t)}{dt} d\,x \; = \frac{dh(t)}{dt} x = \int_0^{h/2} V_x(x,y) \tag{3.12}$$

3.4.3 Numerical implementation

The time coordinate was discretized using a constant time step *dt*. Space was discretized using a regular grid with horizontal and vertical spacing *dx* and *dy* as shown in Figure 3.5. At each time step, the pressure field versus *x*, the horizontal velocity field $V_x(x,y)$ and the closure rate $dh(t))/dt$ were solved. To this end, an unknown vector $\{X\}$ was defined as the concatenation of the horizontal velocities $V_x(x,y)$ at each node, the pressure $P(x)$ at each *x* node and the platens closure rate $dh(t))/dt$:

$$\{X\} = \begin{Bmatrix} V_x(x_1,y_1) \\ V_x(x_1,y_2) \\ \vdots \\ V_x(x_1,y_n) \\ P(x_1) \\ V_x(x_2,y_1) \\ V_x(x_2,y_2) \\ \vdots \\ V_x(x_2,y_n) \\ P(x_2) \\ \vdots \\ P(x_m) \\ \dfrac{dh(t)}{dt} \end{Bmatrix} \tag{3.13}$$

Finite differences were used to discretize equation (3.6) to (3.8) and numerical summation were used to implement equations (3.9) and (3.12).

The system of equations (3.6) to (3.13) can then be written in the residual form:

$$\{R(X, F, h_0, L_0, \eta_0, \lambda, n)\} = \{0\} \tag{3.14}$$

These $m \times (n+1) + 1$ equations were solved using a Levenberg-Marquardt nonlinear solver in MATLAB. At each time step, $dh(t)/dt$ was thus obtained, and the thickness evolution was computed with an explicit Euler integration scheme and the initial thickness h_i. Note that the sample length $L(t)$ was updated at each time step using equation (3.11). Table 3-3 summarizes the model input parameters and the value used in this study.

Table 3-3 : Model input parameters

Parameter name	Symbol	Value used
Sample width (m)	W	0.0508
Initial sample length (m)	L_i	0.0508
Initial sample height (m)	h_i	0.006
Applied force (N)	F	1000, 2500, 5000
Time step (s)	dt	0.1
Discretization size in x (m)	dx	0.000375
Discretization size in y (m)	dy	0.0025
Zero shear rate viscosity (Pa-s)	η_0	7.45e5
Relaxation time constant (s)	λ	52.2
Shear-thinning exponent	n	0.59

3.5 Results and discussion

In this section, the experimental and modelling results obtained following the procedures presented in section 3.3 and 3.4 are presented and discussed.

3.5.1 Global flow description and model comparison with experimental data

Figure 3.6 shows sample height changes as a function of time for the 4 different load cases, for ROS samples with small 6.35 by 3.18 mm strands. It gives an overview of the global flow behaviour under high pressure. Initially, the material is fully melted under isothermal conditions. The contact load is not high enough to create flow. At time $t = 0\ s$, when the force is applied in a one second ramp, the material starts to flow. The effective pressure resulting from the closure force (calculated using equation (3.10)) is then maximum. This is shown in Figure 3.7, where the effective pressure (P_{eff}) evolution is plotted as a function of time, for the different load levels on UD samples. Then, the sample area increases as the material flows, and the effective pressure reduces. It eventually reaches a minimum pressure P_{min} not sufficient to reach the yield stress and further deform the material: the sample thickness reaches a plateau. The minimum dwell time t_{min} is defined as the time needed to reach this plateau.

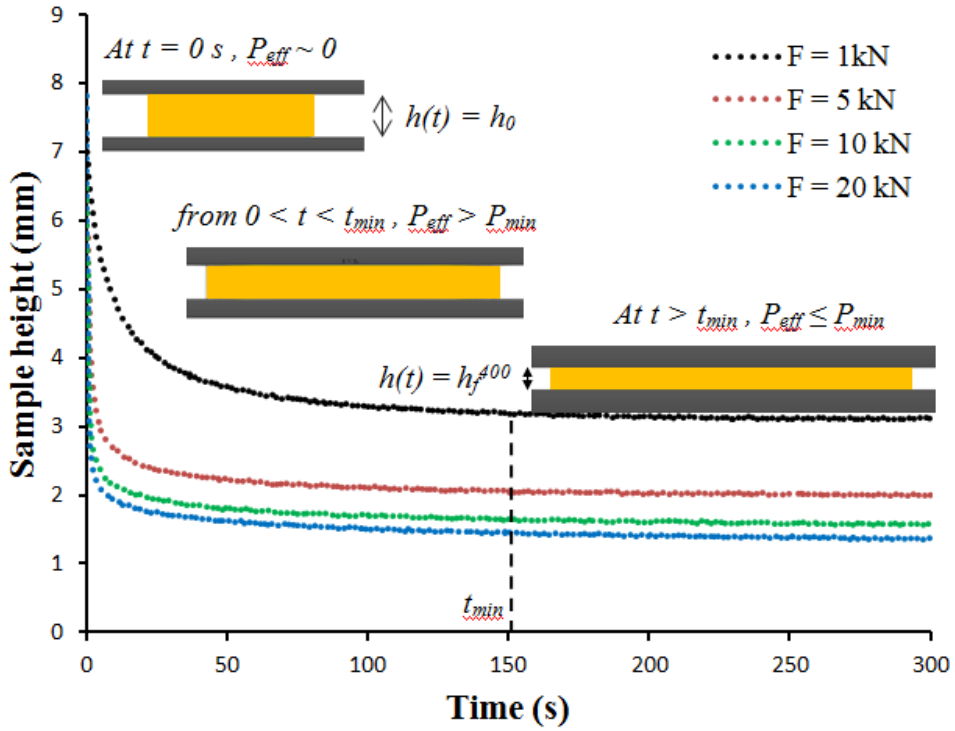

Figure 3.6: Sample height reduction as a function of time, for different closure forces, for ROS samples. Strands size : 6.35x3.18mm. Two phases are visible: viscous fast squeeze an unyielded plateau. The minimum dwell time $\boldsymbol{t_{min}}$ to reach the plateau is shown for the 1kN load case.

The slopes of sample height as a function of time show that the flow velocity strongly depends on the applied load. For the load range tested (1 to 20kN), the yield stress was always reached before two minutes. The minimum dwell time t_{min} decreased for higher applied loads, since the squeeze flow velocity increased and the viscous phase was shorter.

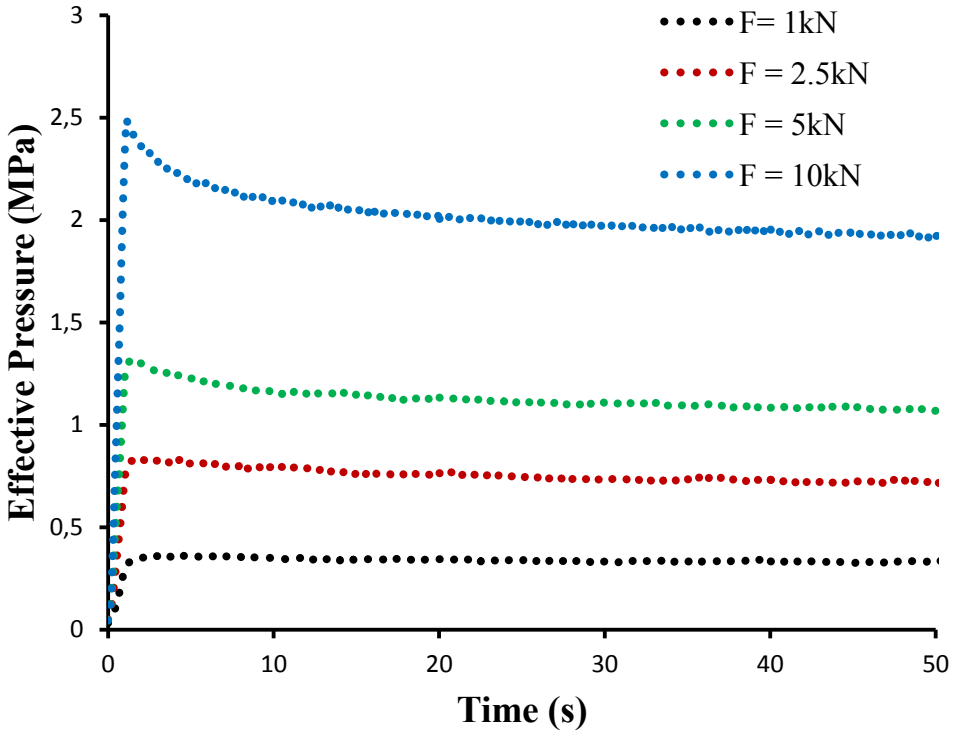

Figure 3.7: Effective pressure evolution as a function of time for different closure forces on UD samples. After the initial increase associated with the force imposition, the effective pressure decreases as the sample area increase.

Figure 3.8 shows a comparison between the modelled and the experimental sample height versus time for different closure forces on UD samples. The model fails to predict accurately the complete squeeze flow under those load levels. The strain is high for the model, compared to classical recommendation of a few percent in the literature [31]. However, Figure 3.9 shows that during the first seconds, the model reasonably reproduces the sample height evolution over time, with an average error of less than 3%.

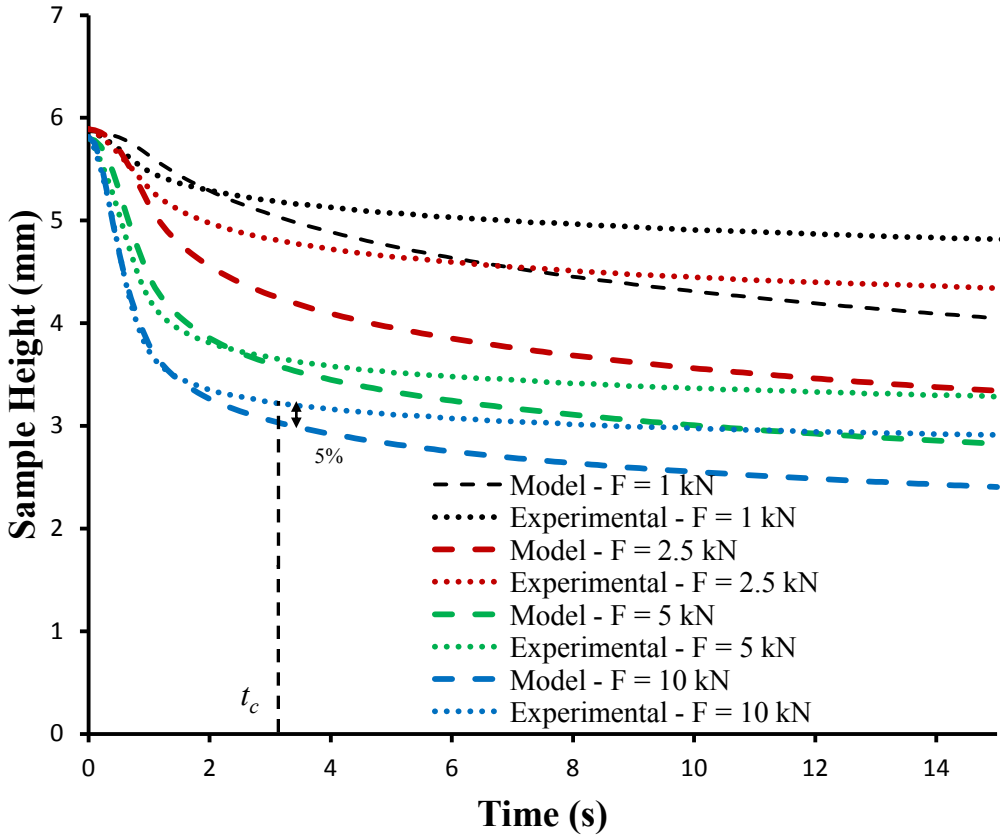

Figure 3.8: Comparison of the sample height reduction predicted by the analytical model and experimental results on UD samples during a complete squeeze flow test. Discrepancy between the model and the experimental data appears after a few seconds. $\boldsymbol{t_c}$ is shown for the 10000N case.

The critical viscous time t_c is defined as the time when the predicted height starts to deviate by more than 5% from the measured one. t_c is an indicator of the duration of the fluid behaviour. It determines until when the assumption of an equivalent fluid behaviour for the composite melt is valid. Also, the viscous strain fraction α_μ is defined as the ratio between the predicted height after t_c ($h(t_c)$) and the final height h_f, with respect to the initial height h_i:

$$\alpha_\mu = \left(\frac{h_i - h(t_c)}{h_i - h_f} \right) \tag{3.15}$$

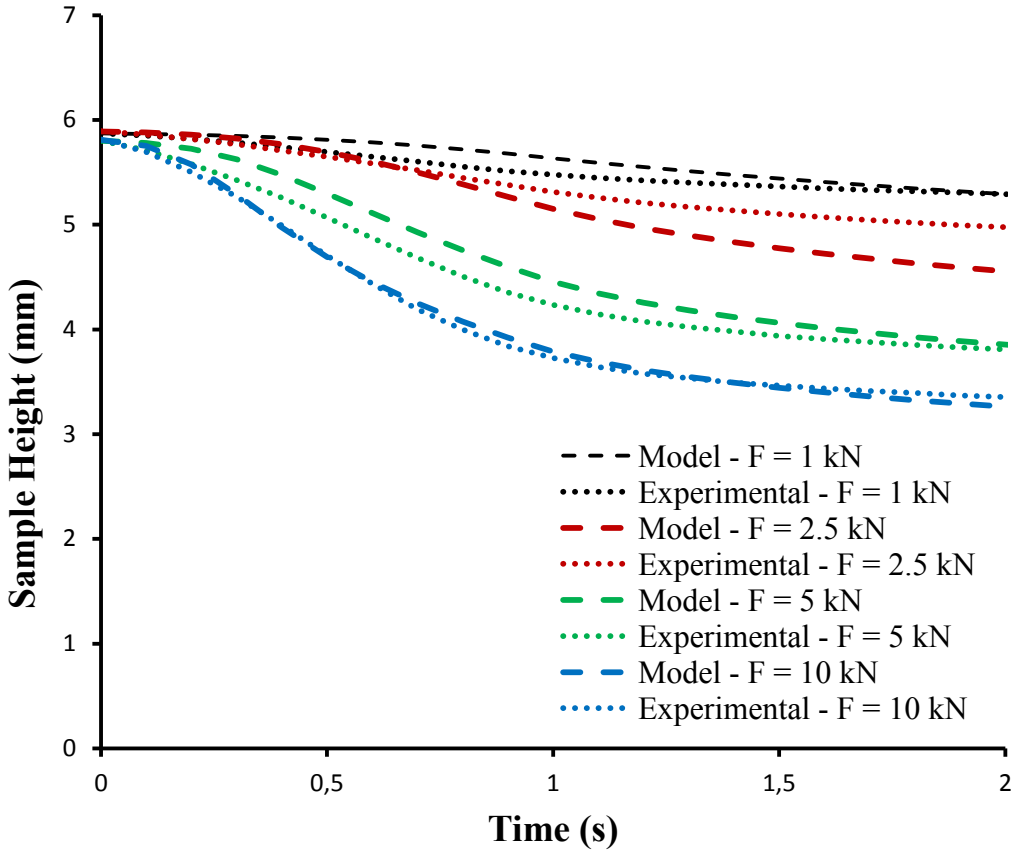

Figure 3.9: Comparison of the sample height reduction predicted by the analytical model and the experimental results on UD samples during the first two seconds of a squeeze flow test. The model is more accurate during this viscous phase.

Figure 3.10 shows t_c and α_μ as a function of the applied force for the UD material. t_c is less than 5 seconds for the load range tested in this study. α_μ quantifies how much of the total deformation occurs during the fluid phase. In the case presented above, α_μ ranges between 35% to 80%. On the one hand it shows that assuming an equivalent bulk viscosity for the composite melt is valid during only a few seconds of the process, but on the other hand most of the deformation occurs during that time for high loads.

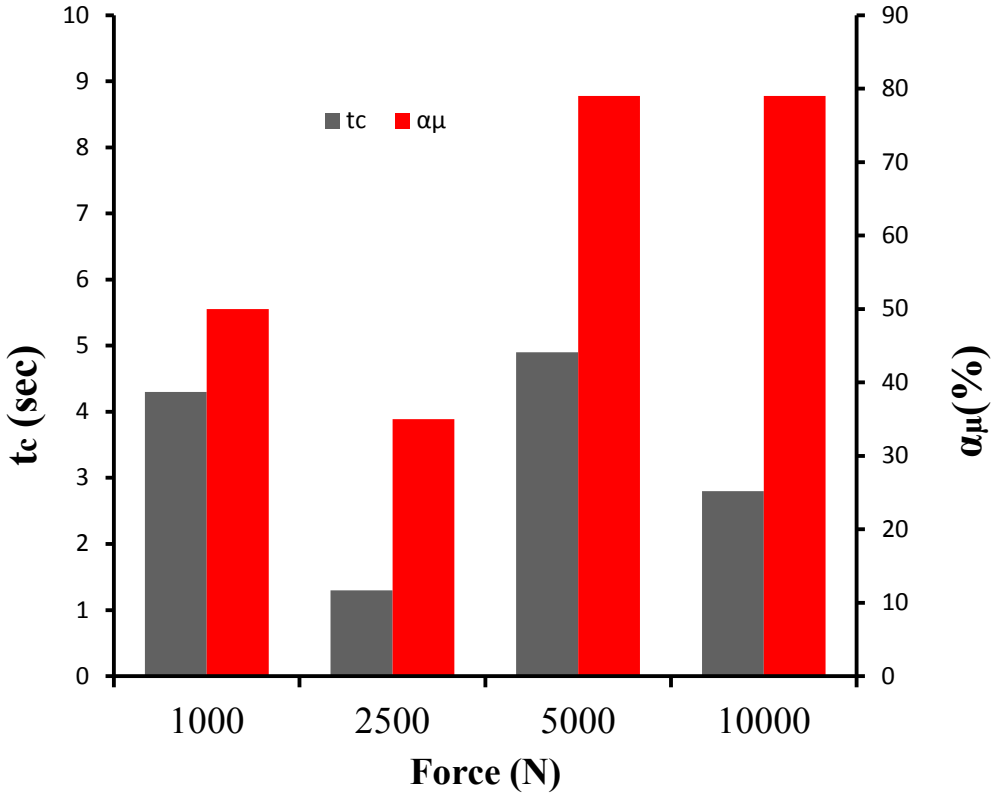

Figure 3.10: Critical viscous time t_c and viscous strain fraction α_μ for the squeeze flow of unidirectional samples for the four closure forces. Most of the deformation occurs during the fast viscous phase.

3.5.2 Comparison between ROS and UD

For UD (0°) preconsolidated laminate, the flow only occurred transversely to the fibre direction, while for ROS samples, flow occurred in both *x* and *z* direction (see Figure 3.11). The 1-D symmetric transverse flow observed for UD samples validates the assumption used in the model. However, a 2-D flow was observed for ROS samples, which makes the 1-D assumption invalid in that case. Moreover, since the model can only predict the first seconds of a test, as shown above, it was not applied to squeeze flow of ROS.

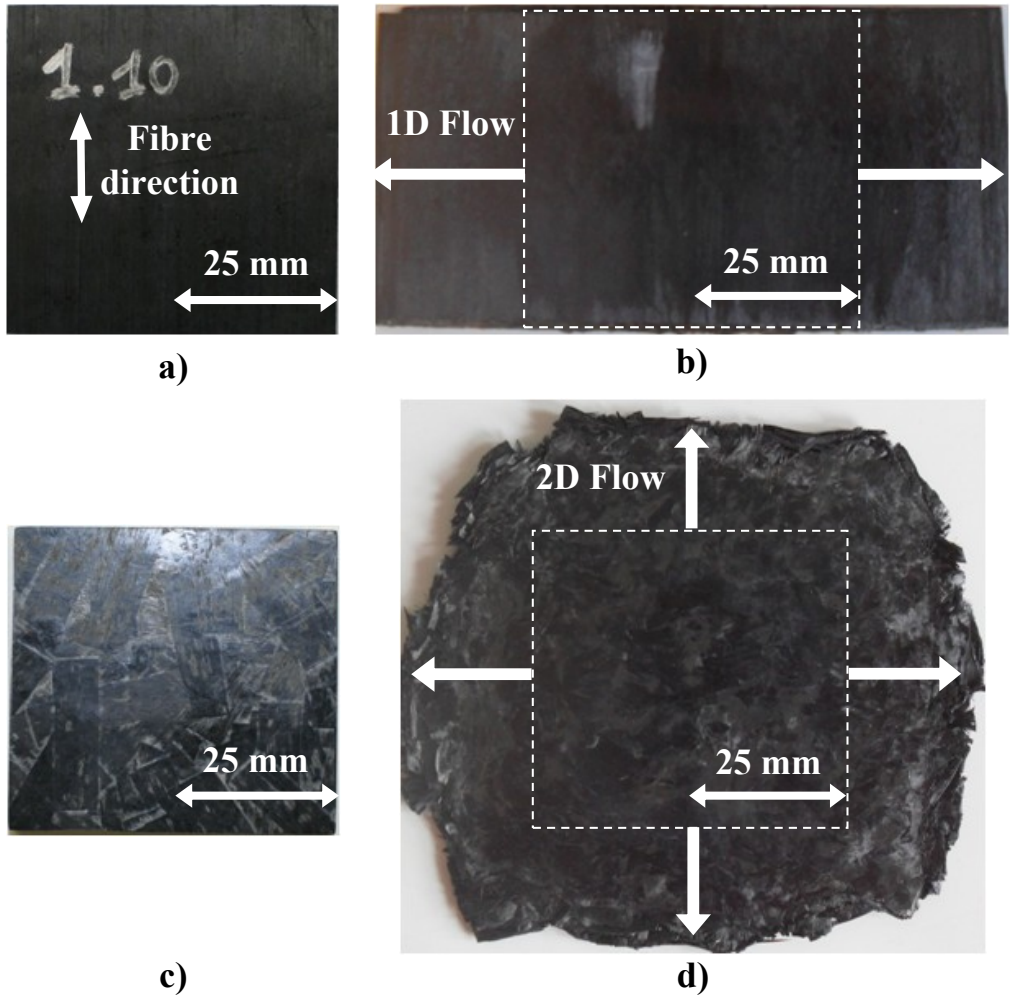

Figure 3.11: Pictures of a UD sample a) prior to squeeze flow b) after squeeze flow and a ROS sample c) prior to squeeze flow d) after squeeze flow. UD exhibits a 1D transverse flow, ROS a bidirectional flow.

Figure 3.12 shows the sample height evolution as a function of time for different strands size as well as UD samples, using a closure force of 5kN. For large strands (25.4 x 6.35mm) the flow is much slower at that load level and the final thickness is twice higher than for smaller strands. Also, UD and small strands sample thickness evolutions match during the first seconds. Then, at t_{min}, when the pressure reaches the minimum pressure P_{min}, and the yield stress is reached, the flow stops, and the sample height remains constant. t_{min} is generally increasing with strands size, and decreasing with the applied load. However, due to the heterogeneity of ROS, there is

some discrepancy in the results, as shown on Figure 3.12, where the final height reached for small strands (6.35 x 3.18 mm) is a slightly higher than for medium strands.

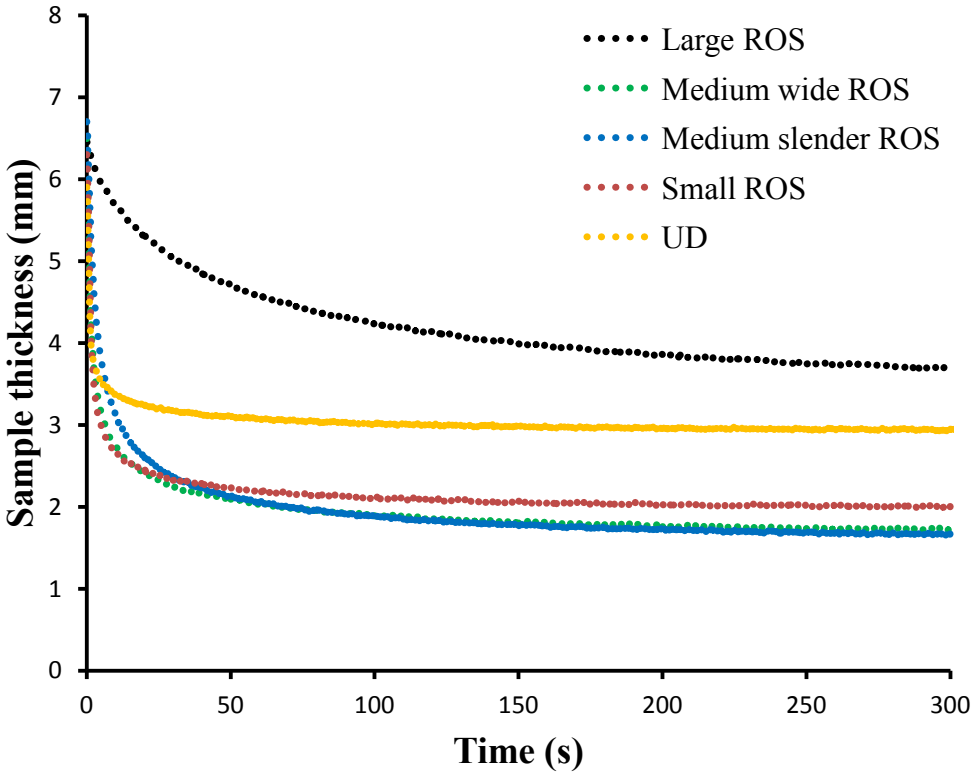

Figure 3.12: Comparison of the sample height reduction measured experimentally for different ROS and UD samples for a closure force of 5kN.

3.5.3 Optical microscopy

Optical microscopy was used on a few representative samples to further investigate the effect of the squeeze flow test on the ROS meso-structure and fibre orientation. Figure 3.13 shows a representative cross-section of a pre-consolidated ROS sample prior to squeeze flow (Figure 3.13a)) and after squeeze flow (Figure 3.13b)). Prior to squeeze flow, there are several resin rich regions, corresponding to the dark gray regions on the micrographs. Also, fibre waviness and out-of-plane fibre orientation can be observed. After the squeeze flow test, strands tend to align in-plane and resin rich regions greatly reduce in size. This shows that squeeze flow improves the consolidation quality of ROS samples and therefore improves mechanical properties.

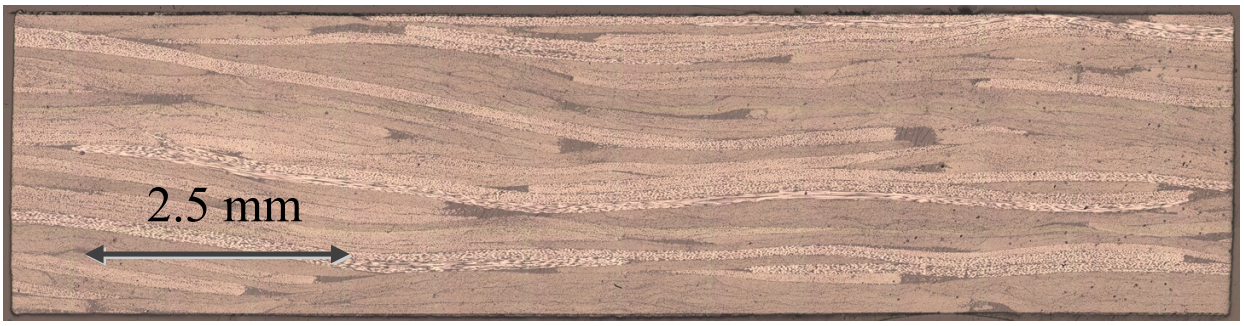

a)

b)

Figure 3.13: Micrographs of cross-sectional samples at 50X magnification. a) Pre-consolidated ROS sample before squeeze flow. Several resin rich regions can be observed and fibre out-of-plane orientation. b) ROS sample after squeeze flow. Strands aligned in-plane and resin rich regions are much smaller.

3.5.4 Strands size effect

Figure 3.14 shows the load versus final strain (calculated using equation (3.2)) curves for the different load level tested in this study. The larger the strands, the higher the pressure required to reach a given strain. It shows that strand size has a large effect on the material viscous behaviour.

Except for one outlier at 5000N for the 12.7 by 3.18 mm strands, the behaviour of the two medium size strands is similar. Nonetheless, there is a consistent final strain increase with the strand length decreasing from 25.4 to 12.7 to 6.35 mm. This suggests that the final strain depends mostly on strand length, and less on strand width.

At low closure force, the final strain is more sensitive to strands length (0.5 strain difference at 1000N), whereas at higher load the final strains are closer (within 0.2 strain). Moreover, the non-linear behaviour observed on Figure 3.14 suggests that a maximum final strain of around 0.8

cannot be exceeded, even with higher forces. This is the upper limit for the macroscopic squeeze flow of the 50 x 50 x 6.5 mm flat panel at 400°C, investigated in this study.

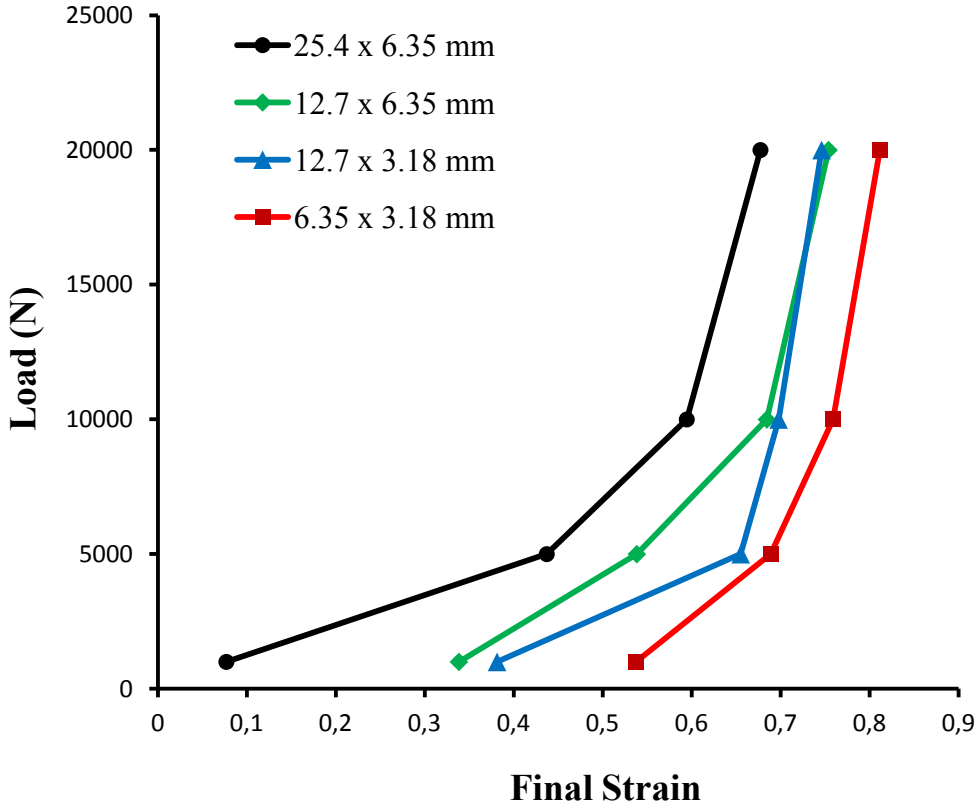

Figure 3.14: Load as a function of final strain for different strand size. Final strain depends on strand length and 80% strain cannot be exceeded.

3.6 Chapter conclusions

In this chapter, an experimental characterization of the squeeze flow mechanism was performed using an in-house developed instrumented hot press. Also, an analytical model was adapted from the literature. The previous models were mainly developed for composite manufacturing processes that involved lower strains, such as Automated Tape Placement. Those models were relatively accurate to predict the squeeze flow behaviour of unidirectional thermoplastic composites under moderate strain (< 50%) and low shear rates. However, this study showed that these models cannot successfully predict the plateau behaviour observed during squeeze flow under high pressure (up to 2.5 MPa).

It was found that high pressure flow of UD or ROS composite materials is mainly governed by two regimes.

1. A Non-Newtonian fluid behaviour of the composite melt with an equivalent viscosity. It is dominant in the first seconds of the process, when the pressure is maximum and the strain rate is low. The effective pressure progressively decreases during this phase.
2. A second yielded phase. When the composite melt has reached a given strain, the shear rate quickly drops to nearly zero and the flow stops. This confirms the existence of a yield stress, likely linked to the inter-ply friction behaviour.

Quantitative indicators were defined to analyze those two phases. The viscous strain fraction $\boldsymbol{\alpha_\mu}$ showed that most of the deformation is fluid like. The minimum dwell time $\boldsymbol{t_{min}}$ indicated that the squeeze flow is fast and occurs in less than 2 minutes even for the largest strands.

Also, the strand size, and especially the strand length, have a large effect on the squeeze flow mechanism.

This study showed that forming UD and ROS Carbon/PEEK composites under high pressure involves two phenomena: a viscous Non-Newtonian behaviour and a yield stress behaviour. To predict the forming of ROS complex parts under high pressure, new models taking both the viscous and the yield stress behaviour have to be developed. The following chapters describe the experimental and modelling efforts done to overcome the limitations of the existing models and propose new predictive tools and guidelines for the processing of ROS composites.

Chapter 4

Experimental characterization of ROS composites using X-Ray tomography

4.1 Introduction

In Chapter 3, it was shown that ROS undergo complex deformation mechanisms. A first effort was done to characterize and quantify the macroscopic squeeze flow behaviour through experiments and application of the current knowledge. However, the heterogeneity of the ROS material and the lack of information on the macro- and meso-structure evolution during squeeze flow requires more investigation. Hence, a characterization of ROS using micro-structure imaging techniques is a next logical step towards a better understanding of ROS deformation mechanisms. In this study, X-Ray Microtomography was used to characterize the ROS meso and macro-structure evolution during the squeeze flow test.

4.1.1 X-Ray microtomography

X-ray microtomography (also known as micro-CT) is a characterization technique that provides three-dimensional microstructural images, based on the material density. Micro-CT is based on X-ray attenuation, which is described by [78]:

$$I = I_0 \exp\left(1 - \int \eta_{att,ave}(s) d\overline{s}\right) \quad (4.1)$$

I is the intensity of the signal at a given spatial coordinate, I_0 is the intensity of an unattenuated beam, $\eta_{att,ave}$ is the average linear attenuation coefficient within a line element $d\overline{s}$ oriented along the direction of X-ray signal. The linear attenuation coefficient $\eta_{att,ave}$ is related to the number of atoms crossed by the signal, and therefore to material configuration and density [78]. By measurement of X-ray intensity levels and powerful geometric reconstruction algorithms, one can observe different material and phases within a microstructure.

The sample is fixed on a rotating stage between an X-ray generator and a reception panel. For a specific scan time, X-rays are generated, they go through the sample while attenuating, and reach the reception panel to provide information about the material nature and density. The sample is then rotated incrementally up to a complete revolution of 360°. High quality micro-CT systems use powerful mathematical algorithms to automatically reconstruct data into a 3D structure that allows separation of the different material phases [78].

Micro-CT is a powerful non-destructive inspection tool that requires almost no sample preparation other than cutting the sample to the desired size. It provides a very high spatial resolutions (up to 1µm per pixel). It has been used in several material researches to characterize woven fibre architecture, Out-Of-Autoclave materials, damage inspection and void content determination [79-84].

4.1.2 Challenges with carbon/PEEK composites

Generally, to obtain good contrast between the material phases using X-Ray tomography, one needs a material with at least two phases of different density, which is usually the case for thermoset matrix composites, such as the out-of-autoclave material studied by Centea *et al*. [84], but not for Carbon/PEEK composite. The density difference between carbon fibres and PEEK matrices is relatively small, so it can be hard to differentiate matrix and fibres using micro-CT. Moreover, the heterogeneity of ROS composites adds a significant level of complexity. Indeed, in order to track the changes in the material meso- and macro-structure during squeeze flow, one

would like to extract strands orientation, position and dimensions at different locations within the ROS mat. In order to extract this information using X-ray tomography a different density material can be added to the fibres to act as markers. In the present study, a conductive silver paint was applied on specific strands denoted as marker strands to track their deformation and displacement during the squeeze flow process.

4.2 Objectives and structure

The objectives of this chapter are twofold: first, to develop a new experimental characterization method using Micro-CT to study the macroscopic squeeze flow mechanisms and the meso-scopic transverse deformations of ROS composites; second, to demonstrate how this method can be applied to quantify the deformations and perform non-destructive inspection of complex ROS parts. Relevant data is then extracted to help the development of a predictive model later in the thesis.

The following sub-sections describe the proposed experimental method and highlight the key results obtained from the resulting microCT data.

4.3 Materials

The material used in this study was the same Carbon / PEEK ROS compound used in Chapter 3. The squeeze flow experiments of this chapter were performed using the large 25.4 long by 6.35 mm wide and medium 12.7 long by 6.35 mm strands. A conductive silver paint with 40% silver made by M.E. Taylor Engineering, Inc. was used to paint the marker strands used to track the flow front with X-Ray tomography.

4.4 Procedures

The proposed method consists of applying a conductive silver paint on marker strands. These markers are then placed at strategic locations through the thickness of the part. The initial and final positions, orientations and dimensions of the markers can then be measured using X-Ray tomography. The markers can be used to extract the macroscopic flow profiles and mesoscopic

deformations. They also help to identify consolidation defects such as compaction gradients and large fibre waviness.

The procedure used to characterize the flow front involved a four step process, as shown in Figure 4.1. First, the samples were pre-consolidated using an industrial 100 Tons Wabash press, using exactly the processing cycle described in Chapter 3, section 3.3.3. Second, the samples were scanned using X-Ray tomography. Then, the sample was placed in the instrumented hot press and squeezed under different load levels. The squeezed samples were finally scanned to quantify all changes in the position, orientation and shape of the marker strands. The following sub-sections provide more details on each steps of the procedure.

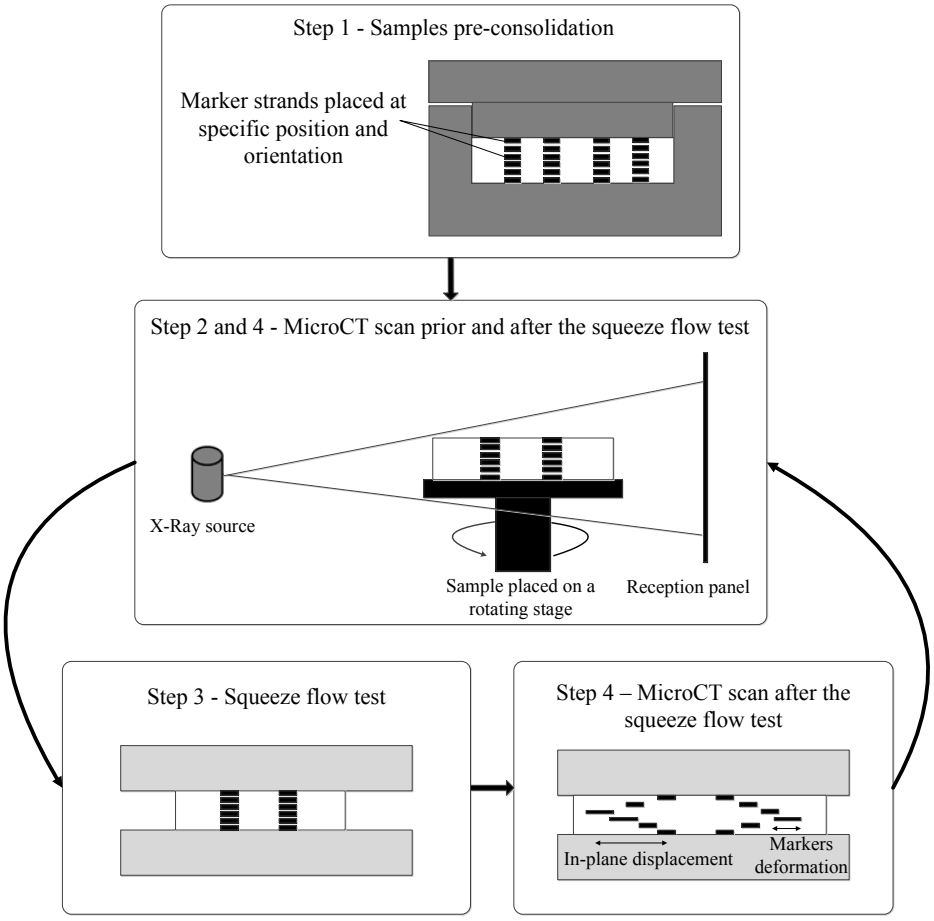

Figure 4.1: Schematic of methodology used to track the marker strands displacement and deformation using microCT. The black rectangles represent marker strands placed at specific locations within the samples. First, samples are pre-consolidated. Second, they are scanned using microCT to determine their initial position and shape. Third, samples are squeezed using the instrumented hot-press. Finally, deformed samples are scanned to determine markers in-plane displacement and deformation.

4.4.1 Markers preparation

The markers consist of strands painted with the conductive silver paint from M.E. Taylor Engineering Inc. on each side. The markers were painted using a little brush and were allowed to dry for at least one hour before sample manufacturing. Experimental evidences showed that the conductive silver paint was not affected by the application of heat and pressure and tended to stick to the pre-impregnated chopped strands. Experiments also showed that the overall macroscopic squeeze flow behaviour was not affected by using only a dozen of markers per samples. However, the silver paint might slightly affect some of the properties at the markers location, such as the inter-ply friction behaviour, but these local effects were neglected due to the small number of markers per sample, compared to hundreds of strands. Thus, it was a good method to track the displacement, deformation and orientation changes for a specific strand in the ROS flat panel during squeeze flow.

4.4.2 Sample preparation

The samples used in this study were cut from 150 mm by 150 mm ROS flat panels pre-consolidated by compression moulding. The following sub-sections describe the layup process used to place the markers among the mat and the processing cycle used to manufacture the panels. For the large strands panel, the first layer containing 8 markers was placed directly on the bottom of the tool at the position and orientation shown by Figure 4.2a). For a 6.5 mm thick consolidated plate, 250g of strands were divided in five equal weight batches. The first batch was added on top of the bottom markers. Extreme caution was taken to avoid moving the markers while the strands were randomly placed. The same procedure was repeated five times before a last set of markers was placed on top of the mat. Overall, for the large strands panel, 48 markers were used (6 layers of 8 strands) for each panel. For the medium strand panel, the procedure was exactly the same, but 96 markers were used: 16 markers per layer were placed. This was done since 4 markers per layer can be fitted in a 50 mm by 50 mm sample made with medium strands, while only two can be fitted for large strands.

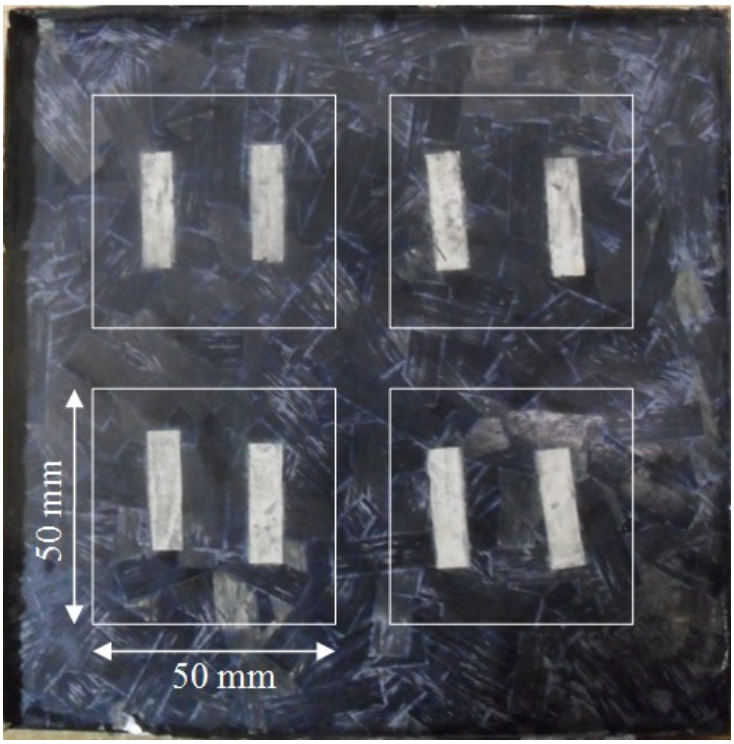

a)

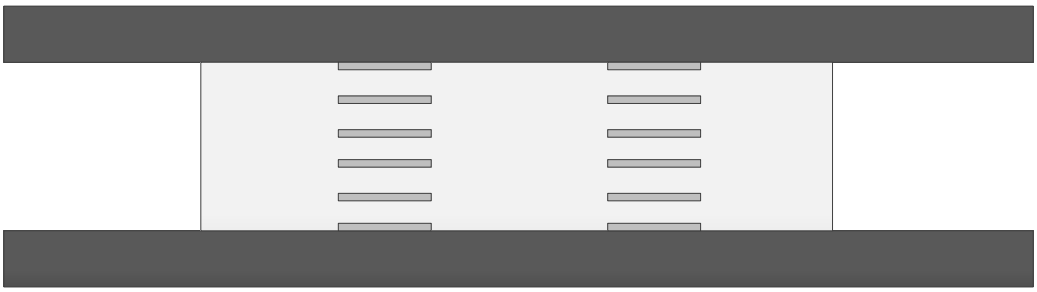

b)

Figure 4.2: a) Picture of a pre-consolidated flat panel with large marker strands and samples location. b) Schematic of the markers position along the sample thickness, each sample contains two rows of 6 markers.

Next, the flat panels were pre-consolidated using a Wabash 100 ton hot press using the same processing cycle described earlier in the thesis (see Chapter3, section 3.3.3). The panels were trimmed and four 50mm x 50mm samples were cut using a diamond saw, according to the sample configuration shown on Figure 4.2a). At the end, each sample contained two rows of 6 markers, as shown on the schematic of Figure 4.2b).

4.4.3 Squeeze-flow test procedure

The squeeze flow test procedure and equipment are the same as the one presented in the previous chapter. The pre-consolidated samples were placed between the hot-press parallel platens. Their temperature was increased to 400 Celcius and squeezed under different load level. The following test matrix shows the different case study presented in this chapter. The load levels were selected to observe the macroscopic squeeze flow from the early stage at low load (case A to C) to higher loads closer to representative processing conditions (case D).

Table 4-1: Squeeze flow and microCT experimental test matrix.

Case Study	Strand Size	Applied Load (N)
A	Large	562,5
B	Large	1125
C	Large	2250
D	Medium	20000

4.4.4 Micro-CT scan and reconstruction procedures

The pre-consolidated samples were scanned using an XTek HMXST 225 computed tomography system in order to determine the initial position, orientation and shape of the markers. The main scan parameters are summarized in Table 4-2. The scan resolution was around 2μm/pixel, corresponding to the spatial dimension of each pixel. All the samples were scanned in the same conditions, using an acceleration tension of 45 kV and an intensity of 347 μA. Those two parameters were selected to optimize the contrast between the markers and the ROS material. The number of Frame Per Projections (FPP) was set to 4 for all the scans. This gave the optimal resolution while minimizing scan time. Scan times were approximately 5 hours. Also, three to six samples were scanned at the same time, thus minimizing the number of scan required.

Table 4-2: Micro-CT scan parameters

Parameters	Value
Filter	None
Resolution	2μm/pixel
Image size	2000x2000pixels
Frame Per Projection (FPP)	4
X-Ray Voltage	45kV
X-Ray intensity	347μA

CT Pro software was used to reconstruct the scan data into 3D volume data. ORS Visual software was used to visualize and analyze the data. It allows to visualize the data in both 2D and 3D format.

A detailed description of the scan and reconstruction procedures can be found in Appendix B.

4.5 Results and discussion

4.5.1 Pre-consolidated samples microCT results

Figure 8 shows the computed tomography results of a pre-consolidated sample prior to squeeze flow. Figure 4.3a) shows a two dimensional cross-sectional view of one row of markers, in the longitudinal direction and Figure 4.3b) shows the markers in the perpendicular direction. Many features can be observed and quantified on those computed tomography results.

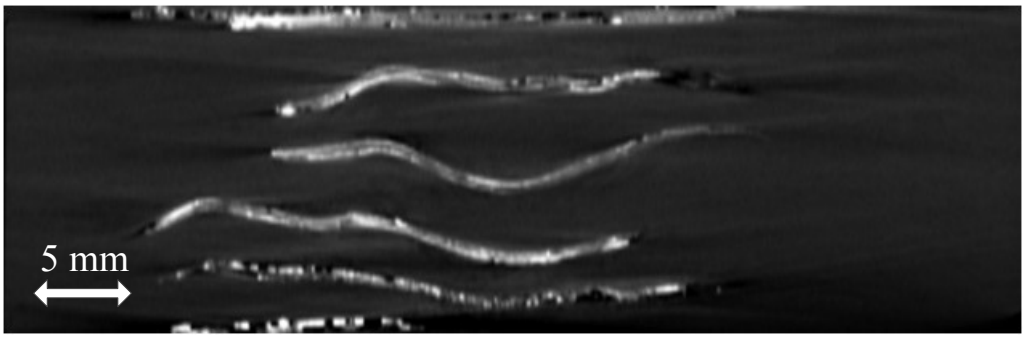

a)

b)

Figure 4.3: Initial configurations of the markers in the preconsolidated sample of case A prior to the squeeze flow test. a) Longitudinal direction. b) Perpendicular direction.

The heterogeneous distribution of strands in the part led to a compaction gradient. This was observed in all the pre-consolidated samples, where the top and bottom strands (near the tool surface) did not experience out-of-plane deformation, while the middle strands were bent. The markers remained mostly in the location where they were initially placed during the layup process.

Those observations were consistent with the deformation mechanisms identified for ROS in Chapter2. The out-of-plane deformation observed on the markers in the middle of the sample was associated with the packing stress at low loads.

Moreover, the width of the markers after pre-consolidation ranged from 6.35 to 20mm, which is a 0 to 320% increase from the initial width (6.35mm). This was associated with the meso-scopic transverse deformation mechanism. For all the pre-consolidated samples, the top markers exhibited large transverse deformation while most of the other markers located in the middle and at the bottom expected nearly zero transverse de formation. These large deformations at the

mesoscopic scale also contributed to the inter-strand void content reduction mechanism that was discussed previously.

The pre-consolidated samples computed tomography results were also used to measure the initial position of the markers by measuring the relative distance between the two markers of each layers. The ORS Visual data analysis software was used to perform this task.

4.5.2 Meso-scopic transverse deformations measurements

After the squeeze flow tests, the samples were scanned and analyzed. First, the meso-scopic transverse deformations were quantified for all the samples. The meso-scopic transverse deformation is associated with the squeeze flow of each individual strand, as defined in Chapter 2, section 2.2.2. Figure 4.4 shows a schematic of the meso-scopic transverse deformation of one single marker strand. Using the computed tomography results of samples scanned prior and after the squeeze flow test, the initial and final width of the marker strands can be visualized and quantified.

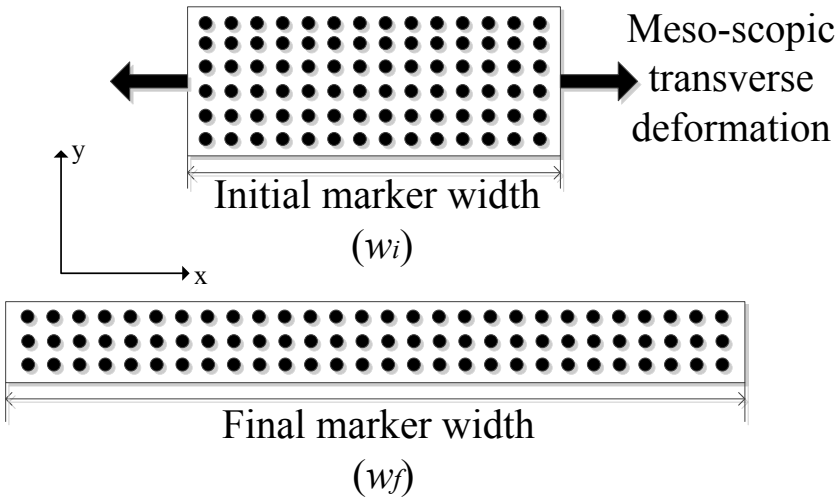

Figure 4.4: Schematic of the meso-scopic transverse deformation. Marker strands initial and final width was measured using the microCT results and the data analysis software.

Figure 4.5 shows a two dimensional cross-sectional view of the top, middle and bottom markers of cases A and C. From these images, it is clear that the bottom markers did not deform at all during the squeeze flow test and their position, orientation and dimensions remained identical. On the other side, the top markers were highly deformed, but this was already observed in the

pre-consolidated samples. However, their position and orientation did not change, showing clearly that no slippage occured at the tool platen. Finally, the middle markers expected both transverse deformations and macro-scopic flow. This latter aspect is discussed in the next sub-section.

In order to quantify the markers transverse deformations at the mesoscopic scale, the microCT results were used to measure the markers final width w_f which was compared with the initial one w_i, thus defining the transverse deformation ϵ_t:

$$\epsilon_t = \frac{w_f - w_i}{w_i} \tag{4.2}$$

For Cases A, B and C, the markers final width was measured using the ORS visual analysis software.

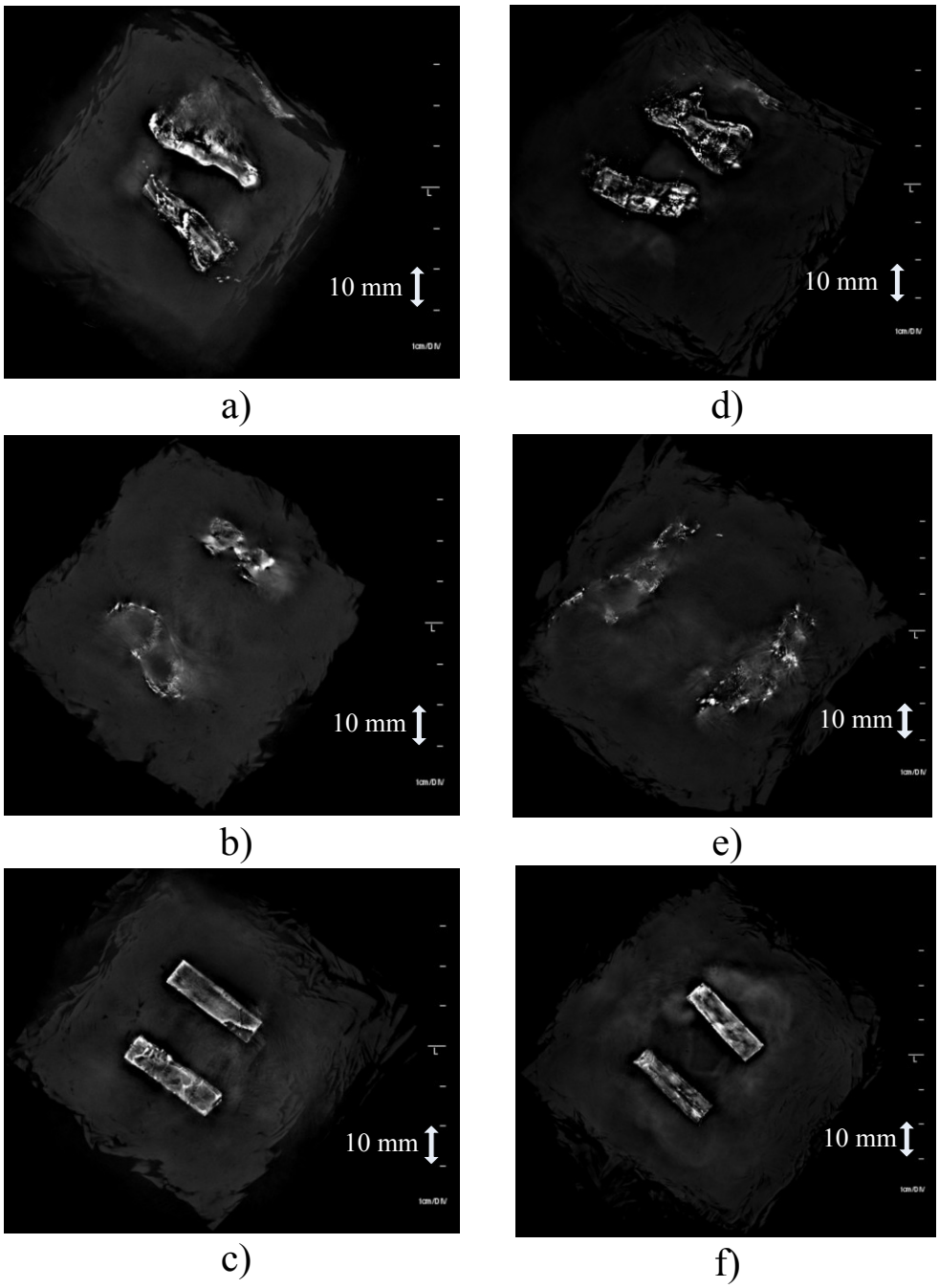

Figure 4.5: Micro-CT images of the markers transverse deformation as a function of the vertical position for cases A and C. a), b) and c) are respectively images of the top middle and bottom markers of case A . d), e) and f) are respectively images of the top, middle and bottom markers of case C.

Figure 4.6 shows a summary of the average transverse deformations for each marker at its normalized position, where zero corresponds to the bottom marker and one to the top marker. The results were averaged for the three load cases. The error bars represent the minimum and

maximum meso-scopic transverse deformations measured at a given normalized position. For all cases, bottom markers experienced absolutely no transverse deformations. They sticked to the bottom platen during the squeeze flow tests and their shape remained rectangular. Also, the top markers showed large transverse deformation of 1 strain in average. However, there was a lot of heterogeneity in the results, where some of the top markers underwent almost no deformations and some deformed up to 1.7 strain. For the four middle markers, the trend was less clear. In average, most of these markers exhibited deformations between 0.25 and 0.8 strain, but there was large discrepancy in the results. The markers closer to the sample top generally exhibited higher transverse deformations.

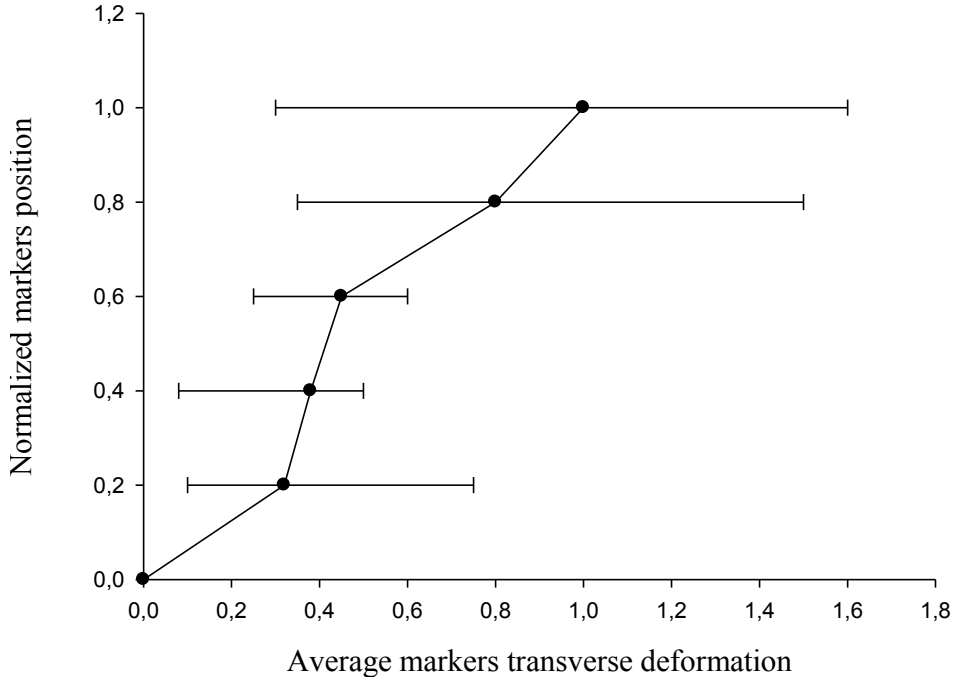

Figure 4.6: Average markers meso-scopic transverse deformations as a function of their position along the sample thickness. Bottom markers expected no transverse deformation and the deformation generally increased from bottom to top of the samples. Large heterogeneity was observed in the results, especially for the top markers.

Overall, it showed that this novel method can be used to quantify and analyse the meso-scopic deformation mechanisms occuring during squeeze flow.

4.5.3 Macroscopic flow characterization and measurements

Figure 4.7 shows a representative cross-sectional view of case A before and after the squeeze flow test. The top and bottom markers remained at their initial position, showing clearly that no slippage occurred at the platen/material interface. On the other hand, the middle layer was subjected to a large in-plane displacement, likely caused by inter-ply slippage between strands.

a)

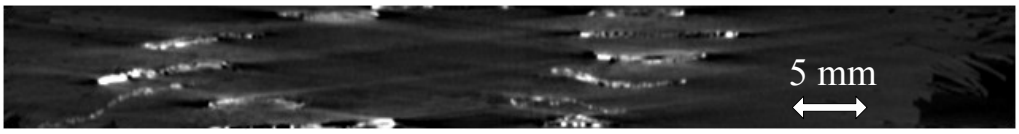

b)

Figure 4.7: a) Initial and b) final configuration of the markers in the perpendicular direction for Case A with an applied load of 562.5N. Heterogeneity in the flow fronts can be observed. The top and bottom markers did not slip.

The ORS visual software was used to measure the in-plane (or horizontal) displacement of each marker relative to its initial position after the squeeze flow test. Figure 4.8 shows the profile of the measured in-plane displacement for cases A, B and C. The values were all measured in the middle of the markers, perpendicularly to the fibre direction. The results show the average relative displacement for each marker and the error bars represent the minimum and maximum values measured for each marker. One can note that the displacement profiles were not symmetric. This can easily be explained by the heterogeneous distribution of strands in the flat panel.

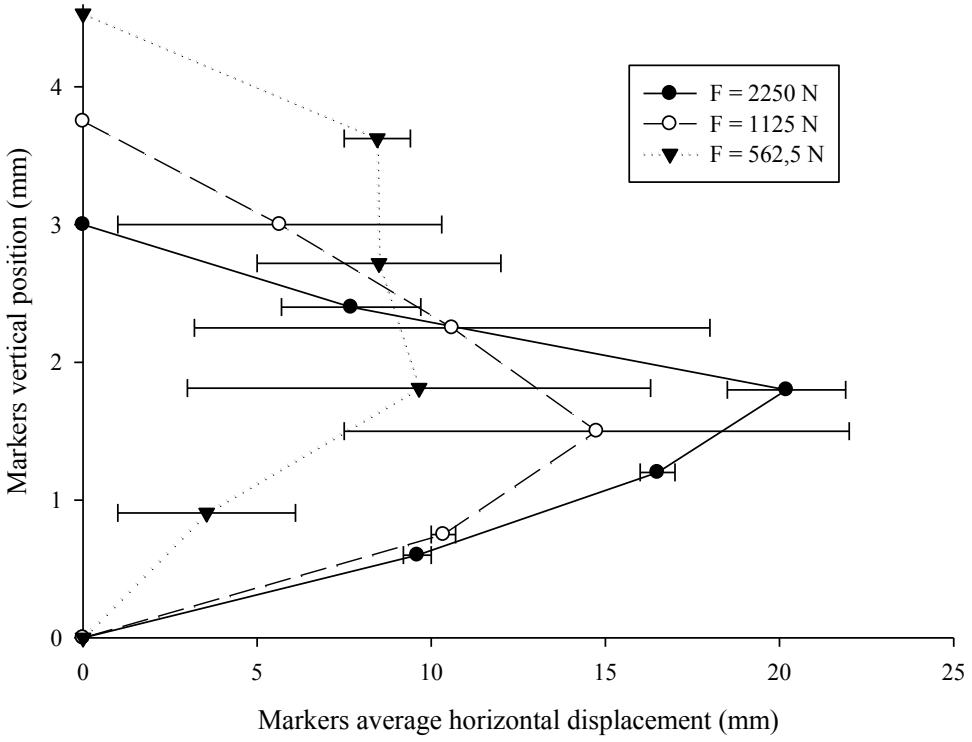

Figure 4.8: Summary of the markers average horizontal displacement for cases A, B and C. The error bars represents the minimum and maximum displacement values measured for each marker. Large variability was observed for markers located in the middle of the samples.

This random factor led to local variability in the flow. In fact, the maximum in-plane displacement measured was 22mm on both case B and C for markers located in the middle of the sample (markers 3 and 4). Moreover, all markers located in the middle of sample B flowed in the same direction, while the other two samples had a flow profile in both direction. Finally, it showed that locally, the random factor had a stronger effect on the direction and magnitude of the flow front compared to the applied load.

Finally, the computed tomography results can also be viewed using three dimensional rendering. Figure 4.9 shows a three dimensional view of the markers for case D, prior to test a) and after the squeeze flow test b). It must be noted that 4 rows of 6 markers were used for this case, since medium strands were used for case D. It shows the high heterogeneity in both the meso-scopic and macro-scopic flow patterns. Under high pressure, the middle markers expected larger

transverse deformations and flowed on a longer distance. One interesting thing that can be noted in this figure is that for most of the markers, even if there is large fibre spreading and fibre waviness, the overall orientation of the markers remained the same. It suggests that during squeeze flow, strands are likely to slide on each other in translation motions and are not rotating. Indeed, no clear evidence of strands orientation change was observed in all the samples analyzed.

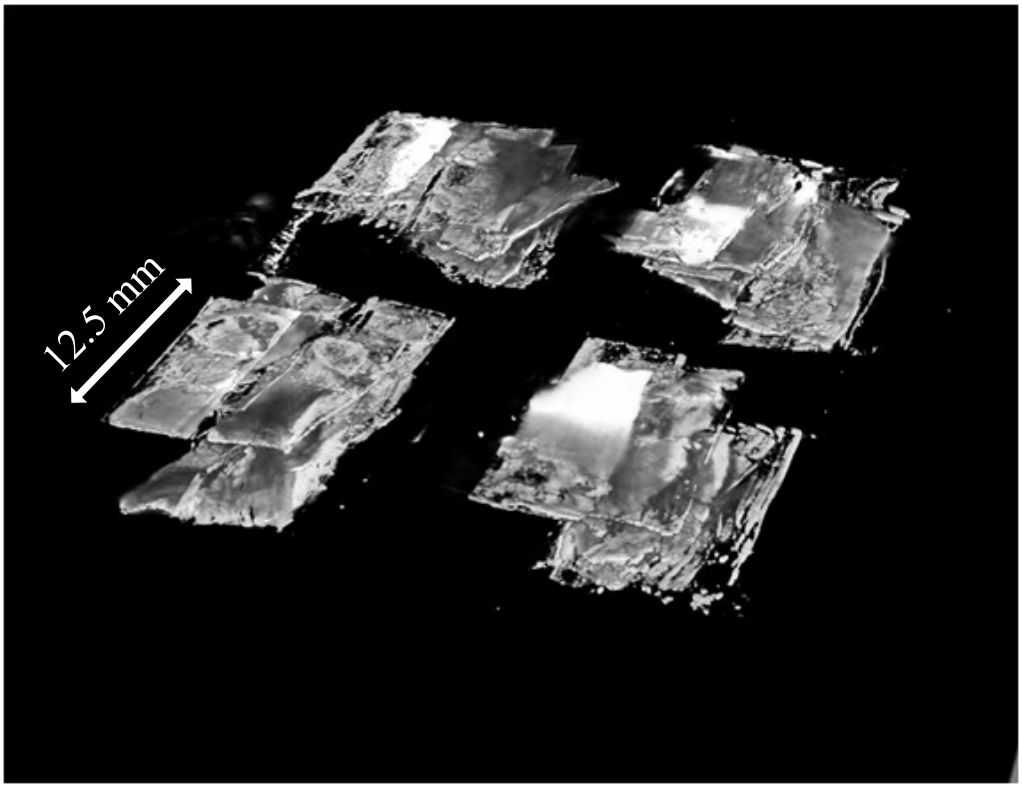

a)

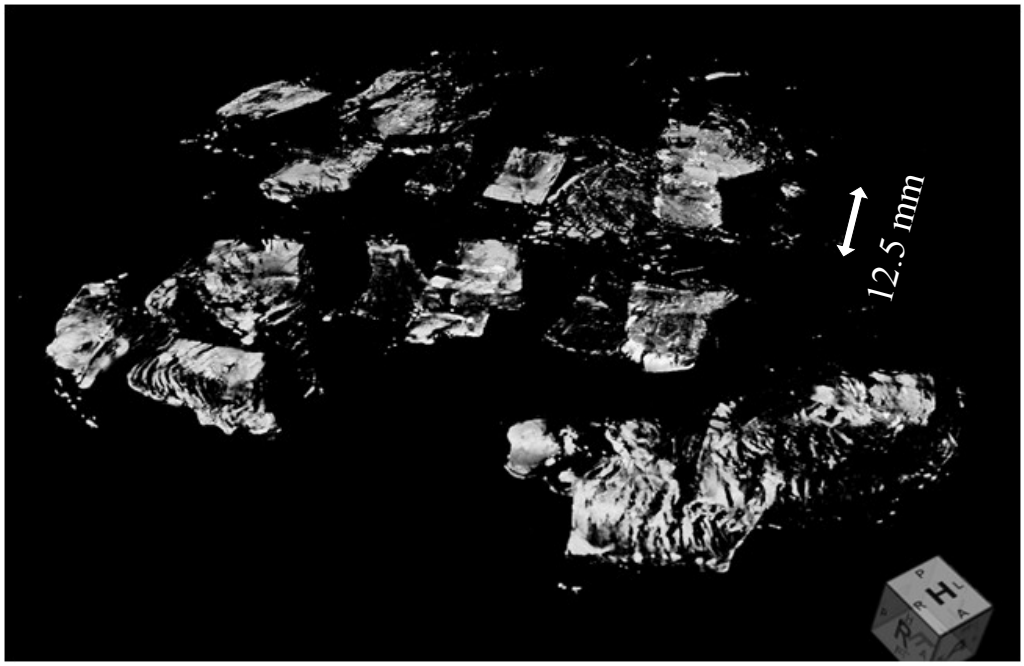

b)

Figure 4.9: Three dimensional view of the markers for case D: a) prior to squeeze flow markers are aligned in the same direction and only the bottom markers are slightly deformed in the transverse direction b) after squeeze flow markers located in the middle randomly flew and showed high transverse deformations, but the top and bottom markers position and shape remained identical.

4.5.4 Case study: application to a three-dimensional complex part

As a first step to demonstrate the applicability of this novel experimental method for analyzing the flow mechanisms occurring when forming complex three dimensional ROS parts, a case study on a simple T-Shape part is presented. The idea is to demonstrate how this method could be applied as a non-destructive inspection method for ROS parts. The part was manufactured using a modified version of the instrumented hot press used during the study, using machined inserts and a picture frame, to produce a simple T-Shape part (see Figure 4.10a)). An extensive study on the processing of T-Shape parts using this modified hot-press was performed by LeBlanc. Details on the design, processing cycle and mechanical testing of these T-Shape parts can be found in the thesis by LeBlanc [85]. In summary, the strands were randomly deposited in the hot-press cavity and markers were randomly placed in the middle of the ROS material. The part was processed using a typical compression cycle, at a temperature of 400°C and a pressure

of 30bar. The part (Figure 4.10b)) was then scan using the same microCT equipment and procedure described in this chapter, section 4.4.4.

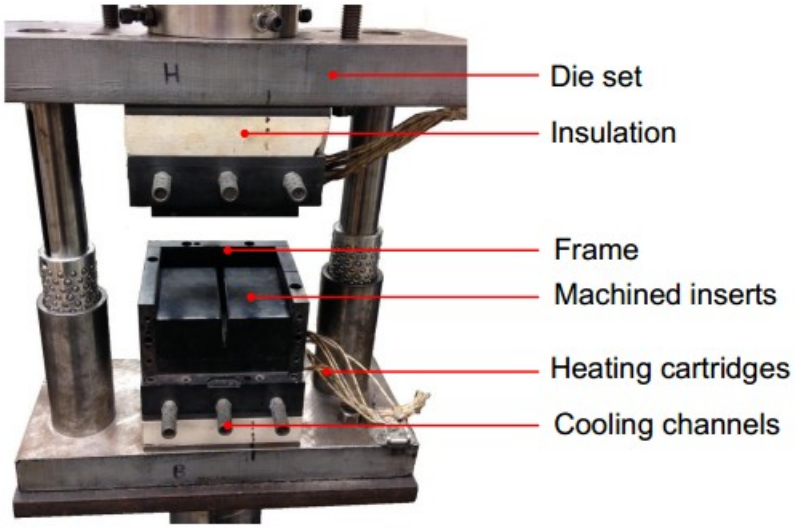

a)

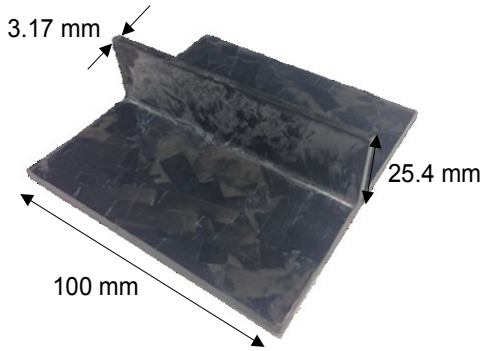

b)

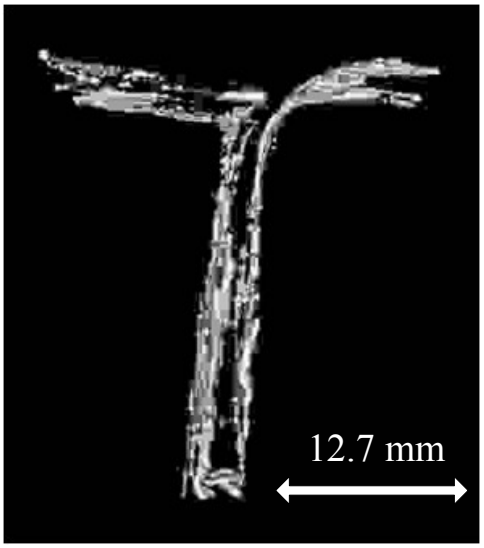

c)

Figure 4.10: Application of the scanning methodology on a T-Shape part. a) Photograph of the modified instrumented hot-press with machined inserts to manufacture T-Shape parts (from [85]).b) The ROS T-Shape part produced with 25.4 x 6.35 mm strands and its dimensions. c) A cross-sectional view of the markers inside the rib section.

Figure 4.10c) shows a cross-sectional view of the computed tomography results showing markers inside the T-shape part. It shows that markers flowed inside the rib feature following

preferential directions. On the one hand, some markers followed a curvilinear path, while others were blocked at the corner of the rib and pushed against the mould wall. Also, none of the markers were located in the middle of the rib section. This simple case study showed that this novel method can be used to characterize the flow and deformation mechanisms occurring when forming complex three-dimensional parts.

4.6 Chapter conclusions

This chapter had two objectives: to develop a new experimental characterization method for ROS composites using microCT and to characterize and quantify the dominant meso-scopic and macro-scopic deformation mechanisms occurring during the squeeze flow test. To this end, marker strands were added to pre-consolidated ROS flat panels and their position, orientation and displacement was tracked before and after the squeeze flow test using microCT. The main conclusions and contributions of this study are summarized hereunder:

1. **A novel technique was developed to track the strands displacement and transverse deformations, using X-Ray tomography.** A conductive silver paint was applied on marker strands placed at key locations in the ROS mat. Tracing the strand positions before and after the squeeze flow test with X-Ray tomography gave an insight into the deformation that the material experienced. At the meso-scopic level, the markers placed on top of the samples generally experienced high transverse deformation up to 320% and those placed at the bottom did not deform at all. Also, it was found that markers slipped in the in-plane direction following translation motions, and no rotation. Thus, the marker orientation remained more or less the same throughout all the squeeze flow tests.
2. **It was found that the material does not slip along the mould platen. This key information was useful to define boundary conditions of the model that will be presented in the chapter 6.**

Moreover, each marker located in the middle of the samples showed random in-plane displacements and spread differently.

It was found that the heterogeneity of this novel material added a random component in the flow pattern. It had local effects on the direction and magnitude of the strands displacement and spreading. Therefore, the applied load cannot be directly used to locally predict the ROS flow front. These phenomena would have been hard to predict without the use of markers.

Chapter 5

An experimental characterization of the inter-ply friction carbon-PEEK composites

5.1 Introduction

As introduced in Chapter 2, inter-ply friction plays a dominant role in forming composites . For compression moulding of ROS, the strands flow and slide one on each other. The inter-ply friction then governs the sliding mechanism. This sliding behaviour is highly influenced by the processing conditions, especially temperature and pressure. In this Chapter, an in-house developed friction measurement apparatus is presented and used to measure the coefficient of friction between UD plies of carbon/PEEK composites. The measurements were performed under representative processing conditions and also compared to experimental results obtained from the literature. The results are used in the next chapter to compare with the model predictions.

5.2 Objectives and structure

The main objective of this chapter is to characterize experimentally the inter-ply friction behaviour of carbon/PEEK composites. As mentioned in Chapter 2, section 2.2.4, a lot of parameters influence the coefficient of friction, namely temperature, shear rate, normal pressure and ply orientation. In this thesis, all the tests were performed under isothermal conditions at 400 °C. This also corresponds to the testing temperature used in other studies on similar materials [28, 62]. Therefore, the effect of the temperature was not studied here, and only the effect of the applied pressure and pulling velocity were considered.

Also, all the tests were done at the same pulling orientation on UD 0°/0° plies. This corresponds to the worst case scenario where the coefficient of friction is the highest, as observed by other authors [28]. The following sections describe materials, equipment, experimental procedures, and highlight the key results and conclusions.

5.3 Background

The technique to measure the coefficient of friction between two given materials c_f is relatively simple. If a ply of a given material is compressed by a load F_n and pulled-through two fixed plies of the same material by a tangential load F_t (see Figure 5.1), by applying static equilibrium and using the Couloumb friction definition, the coefficient of friction can simply be calculated by:

$$c_f = \frac{F_t}{2 * F_n} \tag{5.1}$$

In this study, a pull-out testing fixture was specifically developed to measure the coefficient of friction of pre-impregnated carbon fibre composite plies. Figure 5.1 shows a schematic of the concept behind the pull-out testing method used in this study as well as some of the key dimensions. One ply is pulled between two fixed plies at a given tangential load F_t, and a normal load F_n is applied on the fixed plies. The two load components associated with the friction between the pulled ply and the two fixed plies is calculated using equation (5.1).

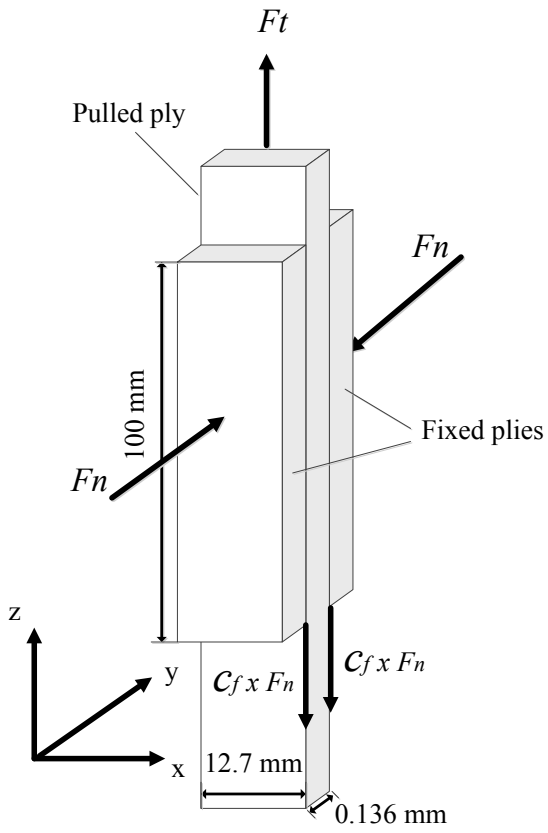

Figure 5.1: Schematic of the friction coefficient measurement technique. One ply is pulled between two fixed plies. The coefficient of friction between the plies can easily be calculated by applying static equilibrium (eq. (5.1)).

5.4 Materials

The material used in this study is the same carbon/PEEK thermoplastic used in the previous chapters. Plies were cut from a UD 150mm wide prepreg tape, and then, used for the measurement of coefficients of friction. Also, Kapton films from DuPont™ were put between the fixed plies and the fixture platens, to protect platens during the tests and to ease removal of the fixed plies after each tests (see Figure 5.2, section 5.5.1).

5.5 Equipment and procedures

5.5.1 Friction measurement apparatus

A friction measurement apparatus for carbon fibre composites was designed to perform pull-out or pull-through tests at any processing temperature (from room temperature to 400 °C) and for a wide range of normal pressure (from 1 to 30 bar). A full description of the fixture, including details on the design and engineering drawings, can be found in the thesis by Scaramanga [86]. It consists of two 25.4mm thick H13 steel platens, heated using three electric heating cartridges controlled individually using type-K thermocouples. In total the six thermocouple inputs and the six 200 W heating cartridges from Omega outputs, via relays, were put into one 6 way CN616 PID temperature controller, also from Omega.

The total contact area of the platen was chosen to be 100mm x 50mm as this was the size used by Murtagh [87, 88] and it was noted that to measure dynamic friction results, a pull-out length greater than 20mm is required [28]. The fixed plies were draped on the platens and clamped using a small flat panel, bolts and wingnuts, as shown on Figure 5.2 . To ensure the ply could bend around the edge of the contact platen a fillet of radius 25mm was used. This was found by looking at the greatest turning angle a piece of PEEK/carbon fibre prepreg composite tape could withstand.

Two ceramic insulation layers of 25.4mm thick were also fixed on the outside of the heating platens, to avoid load cell and fixture over-heating. The insulation material was chosen upon its ability to withstand high pressures, up to 3MPa, and high temperatures, 400°C. A calcium silicate composed insulation was chosen for its good thermal properties. Its thermal conductivity is 0.15 W/mK, it can withstand temperatures of up to 920°C, and has a high compression strength. A simple steady state heat transfer finite element analysis was conducted in ANSYS to ensure that the connecting plate steel reached a safe temperature.

One platen is fixed to a rigid frame and the other is attached to a ball-joint rod end connected to a pneumatic cylinder. The ball-joint rod end ensures self-alignment of the two platens. The pneumatic cylinder was used to apply and control the normal load. A 5kN load cell connected to

the air cylinder was used to measure the applied load. The whole setup was placed in a 5kN MTS Insight® Electromechanical Testing System. The setup was positioned so that when the platens were closed, they were aligned with the upper clamp of the traction machine. The pulled ply was gripped in the MTS machine upper clamp and the traction machine was used to control the pull-out velocity. The MTS 5kN load cell was used to measure the tangential load during the pull-out tests.

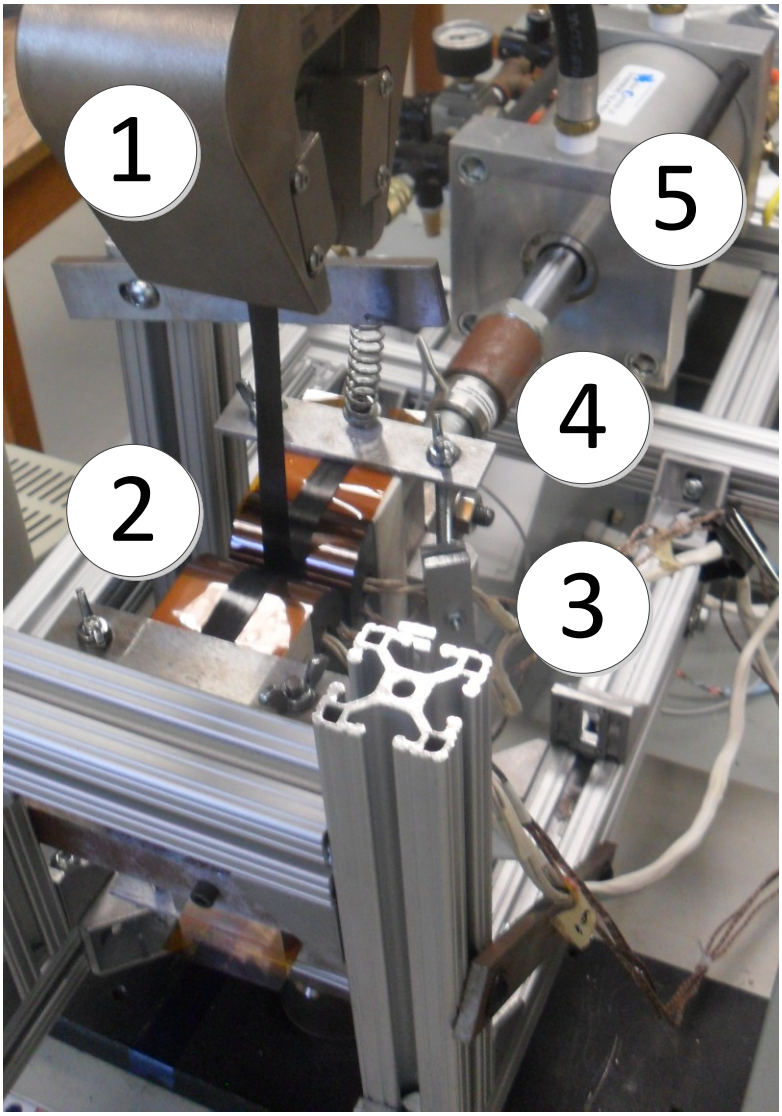

Figure 5.2: Photograph of the friction measurement apparatus. 1) The pulled ply is gripped in the MTS machine upper frame. 2) The fixed plies are wrapped on the platens and attached using the clamping mechanism. Kapton films are placed between the fixture platens and the fixed plies. 3) Heating cartridges and thermocouples are connected to the PID controller. 4) A load cell is used to measure the normal force. 5) A pneumatic cylinder applies and controls the normal load.

5.5.2 Pull-through test procedure

The friction measurements performed in this study were all done under pull-through test condition (i.e. the pulled ply remained entirely between the two fixed plies during the whole pulling test). First, Kapton films were placed on the two steel platens to prevent material sticking and ease sample removal after the tests. The two fixed plies were wrapped on the platens, over the Kapton films, and clamped firmly.

The pulled ply was attached in the MTS machine upper clamp and centered between the two fixed plies. A normal load was then applied using the compressed air cylinder and the load was adjusted using the load cell. The tangential load was also set to 0N and the setup was then heated up to 400 °C in approximately 20 minutes for all the tests. An additional stabilization time of 10 minutes was allowed to ensure isothermal conditions.

The pulling phase was then started. The MTS controlled the pulling velocity and the MTS load cell measured the tangential load evolution and the crosshead displacement throughout the test at a frequency of 1.25 Hz. The tangential load output F_t can then be compared to the applied normal load F_n to calculate the coefficient of friction c_f (see equation 5.1). For all the tests, the sample was pulled a distance of 70mm. New prepreg plies were used for every test performed in this study, to avoid surface deterioration effects that could occur due to pulling.

Table 5-1 summarizes the pulling velocity and normal pressures used in this study. The values were selected based on the order of magnitude of the shear rates encountered in our squeeze flow tests as well as representative normal pressures. All the four pulling velocities were tested with normal pressures of 5 and 20 bars, except for the 10 mm/min case that was also tested at 1 bar, as an extreme low pressure case study. The average normal pressure was calculated based on the normal load F_n and the contacting area between the plies. All the pulled and fixed plies were approximately 12.7 mm wide, and the contacting platen length was 100mm, so the contacting area was approximately 1270 mm^2 for all the tests (see Figure 5.1). All the test conditions were repeated 3 times to verify results accuracy and repeatability.

Table 5-1: Pull through test matrix.

Pulling velocity (mm/min)	Normal pressure (bar)
1	5, 20
10	1, 5, 20
100	5, 20
500	5, 20

5.6 Results and discussions

Following the described procedure and test matrix of Table 5-1, the coefficient of friction was calculated for all the tests performed. The following sub-sections highlight the key results and discuss the effect of the processing parameters on the coefficient of friction.

5.6.1 Effect of the pulling velocity on the coefficient of friction

The effect of the pulling velocity on the coefficient of friction was studied for different normal pressures. Figure 5.3 and 5.4 show representative coefficient of friction results for the four pulling velocities tested in this study, using an average normal pressure of 5 bar and 20 bar, respectively. The time axis t^* was normalized with respect to the final time t_f of each test, for easier data visualization (equation (5.2). Since the pull-through tests were stopped after a pulled distance of 70mm, the actual pulling time t is different for each case and depends on the pulling velocity. Thus, a time normalization enables comparison of the coefficient of friction measurements on the same time scale.

$$t^* = \frac{t}{t_f} \tag{5.2}$$

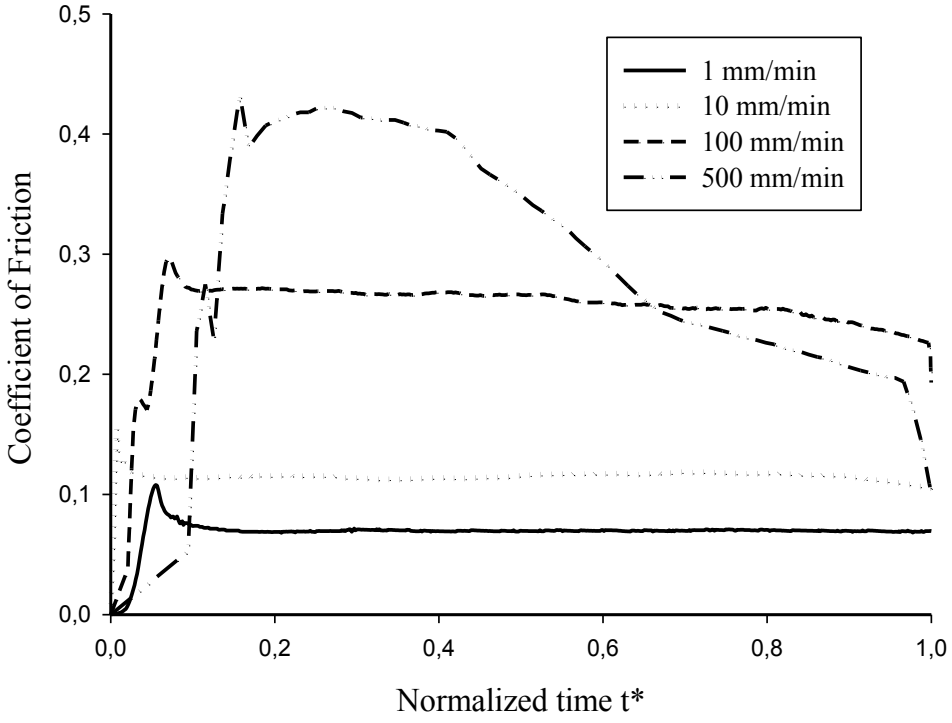

Figure 5.3: Effect of the pulling velocity on the inter-ply coefficient of friction for an average normal pressure of 5 bar. The coefficient of friction increases with pulling velocity. High variability was observed for the tests performed at 500 mm/min.

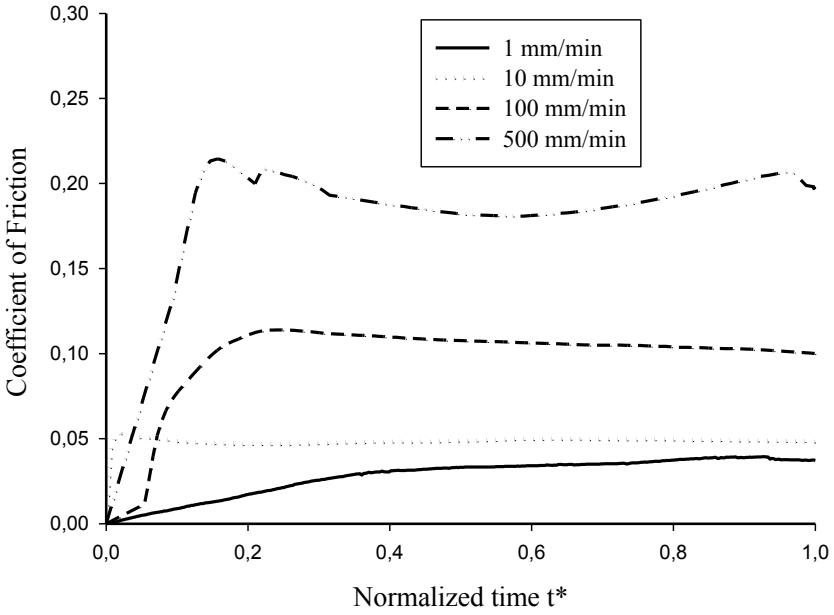

Figure 5.4: Effect of the pulling velocity on the inter-ply coefficient of friction for an average normal pressure of 20 bar. The coefficient of friction increases with pulling velocity. High variability was observed for the tests performed at 500 mm/min.

First, one can observe that the static coefficient of friction, corresponding to the peak value of each curve, is always higher than the dynamic coefficient of friction, as expected. For the first three pulling velocity, the dynamic coefficient of friction is pretty constant. However, for the 500 mm/min case, the dynamic coefficient of friction is around 0.4 for the first seconds of the test, and suddenly starts to decrease all the way to 0.1. These unexpected behaviour happened for most of the high velocity tests. This can be explained by the changes in the samples geometry and fibre orientation during the high velocity tests. Indeed, before the tests, fixed plies and pulled plies were perfectly aligned and all fibres were all oriented in the pulling directions. When tests were performed under extreme velocity conditions, some fibre entanglement, matrix re-distribution at the ply surface, wrinkling, and buckling was observed. This could be due to small misalignments in the testing fixture that becomes more pronounced under high pulling velocity. Also, under high pressure, the tape can spread due to squeeze flow, therefore the contacting area between plies may increase, which can also affect the coefficient of friction measurements. These effects show that the inter-ply coefficient of friction can be greatly affected when plies are

deformed. In this study, only new prepreg plies were studied, and the effect of ply deformation on the coefficient of friction was not quantified.

Figure 5.5 summarizes the average values found for the static and dynamic coefficient of friction, for the different pulling velocities tested, under an average normal pressure of 5bar. The error bars represent the minimum and maximum values found for each test case. Overall, the static and dynamic coefficients of friction both increase with pulling velocity for a given normal pressure. The repeatability is better for the static coefficient of friction. Large variability was found for the dynamic coefficient of friction measured at 500 mm/min, nevertheless the static coefficient of friction was more consistent throughout all the tests.

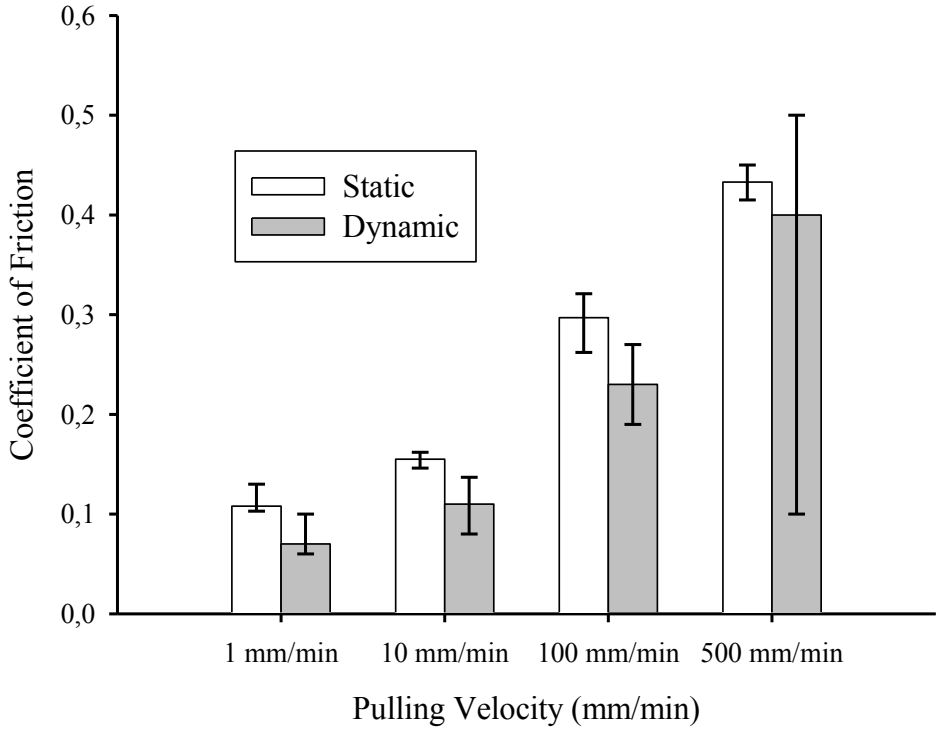

Figure 5.5: Effect of the pulling velocity on the inter-ply coefficient of friction. Summary of the static and dynamic coefficient of friction measurements. Static and dynamic coefficient of friction both increase with pulling velocity. Results are presented for the 5 bar case.

5.6.2 Effect of the normal pressure on the coefficient of friction

Then, the effect of the normal pressure was studied for a constant pulling velocity. The setup controlled the normal load, so the average normal pressure was calculated based on the contacting area, as defined in section 5.5.2. Figure 5.6 shows representative coefficient of friction results found for the three normal pressure tested (1, 5 and 20 bars), at a pulling velocity of 10 mm/min. Globally, the coefficient of friction decreased with the applied pressure. Coefficients of friction as low as 0.04 were measured for an applied pressure of 20 bar. Also, at 1 bar, the static coefficient of friction (0.3) was approximately 30% higher than the dynamic coefficient of friction (0.23), as shown in Figure 5.6. At 5 bar, it was approximately 20% higher and at 20 bar there was a very low difference (less than 1%). These trends are in agreement with other experimental results found in the literature using similar materials [28].

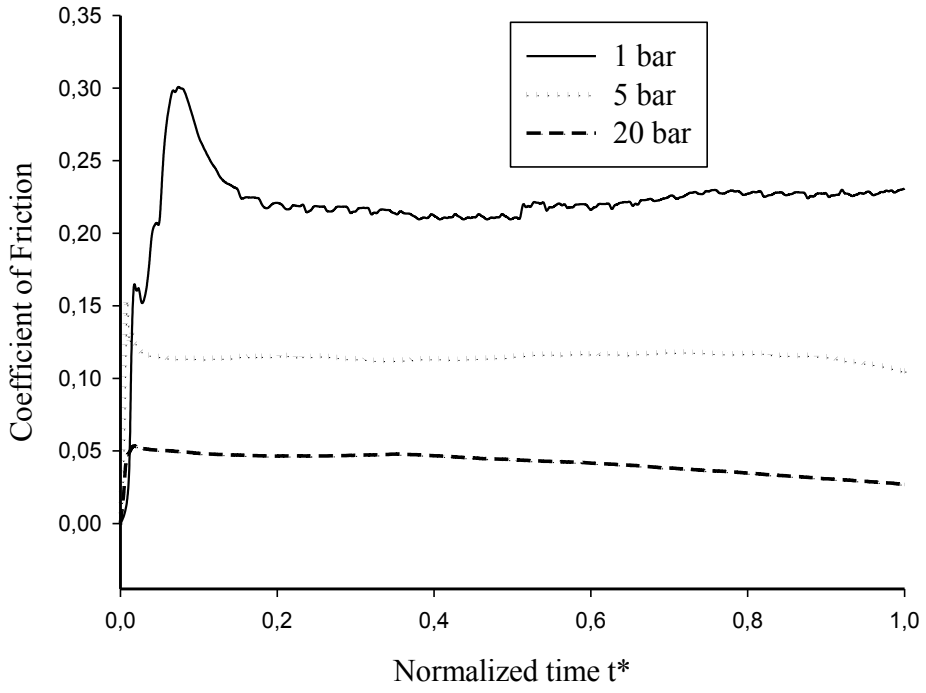

Figure 5.6: Effect of the normal pressure on the inter-ply friction coefficient. The coefficient of friction decreases with the applied pressure. The difference between the static and dynamic coefficient of friction also decreases with the applied pressure.

Finally, Figure 5.7 shows a summary of the average static and dynamic coefficient of friction for the three pressure level tested at 10 mm/min. The error bars represent the minimum and maximum values measured for each pressure level. It is interesting to note that for low pressures, the difference between the static and the dynamic coefficient of friction is much larger than for high pressure levels. At 1 bar, the average static coefficient of friction is 0.33 compared to 0.2 for the dynamic one, whereas for a pressure of 20 bar, the average value is around 0.05 for both the static and the dynamic coefficient of friction.

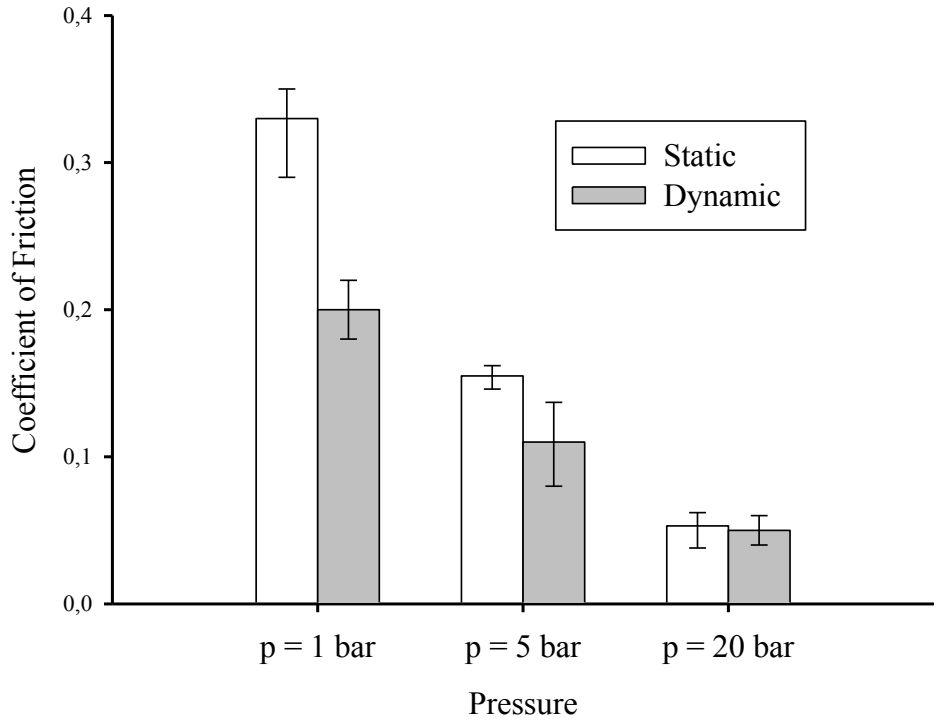

Figure 5.7: Effect of the normal pressure on the inter-ply friction coefficient. Static and dynamic coefficients of friction are compared for different normal pressure at pulling velocity of 10 mm/min.

5.6.3 Results summary and discussion

Figure 5.8 summarizes the static coefficients of friction values found for the different pressure levels and pulling velocity using a log-log scale. A linear regression relationship between pulling velocity and maximum coefficient of friction for a given pressure level was found with a R^2

value over 95%. It can be useful to estimate the coefficient of friction for pulling velocities and pressure levels within the range of values tested experimentally.

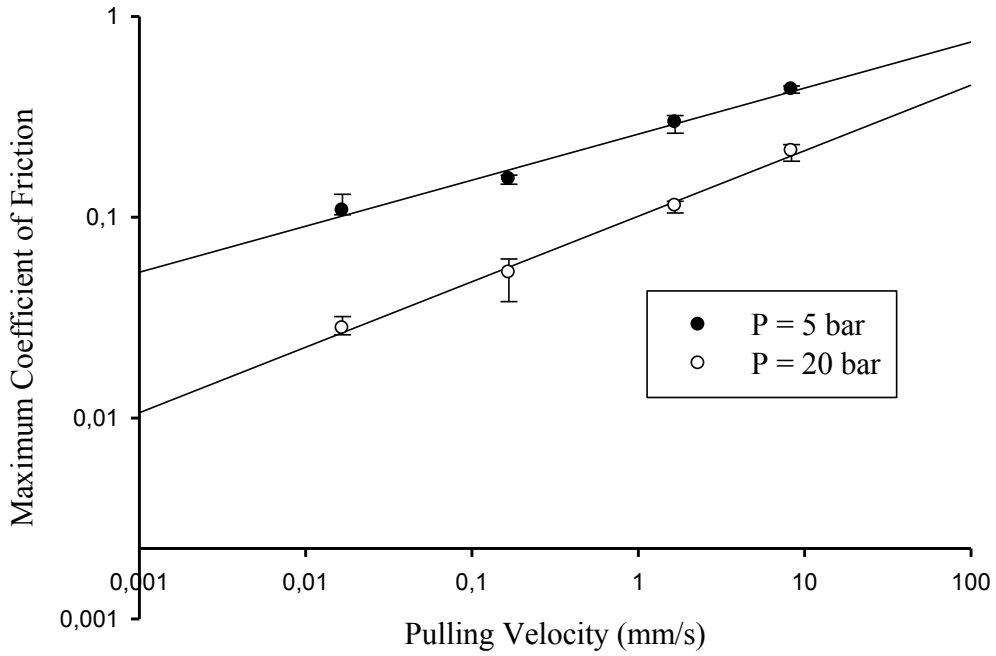

Figure 5.8: Summary of the maximum coefficient of friction measured for the different pulling velocities and applied pressure.

Finally, it was shown in Chapter 3 that ROS composites seems to follow a yield stress behaviour. The yield stress of ROS composites is likely to be linked to the inter-ply coefficient of friction. Authors showed that the yield stress of short fibre suspensions is a function of the coefficient of friction and the out-of-plane compaction pressure [55, 57]. So, the coefficient of friction results found in this study are compared with the yield stress predictions obtained using the model that is presented in Chapter 6.

5.7 Chapter conclusions

The main objective of this chapter was to measure the inter-ply coefficients of friction of the carbon/PEEK material used in this study. Using an in-house developed apparatus, the coefficients of friction were measured for representative normal pressures and shear rates. This study led to the following conclusions and contributions.

1. **The inter-ply coefficient of friction of carbon/PEEK is highly dependent on the testing method and parameters**. It was found that the coefficient of friction increased with pulling velocity and decreased with normal pressure. For the range of pressure and pulling velocity tested, the coefficient of friction ranged from 0.01 to 0.45. A lot of variability was found in the results, but generally the static coefficient of friction results were more repeatable from one sample to the other than the dynamic coefficient of friction.
2. **A better control of the normal pressure application would increase the accuracy of the testing apparatus and thus would improve repeatability.** However, the general trends observed in this study are in agreement with published results on similar material and test methods from other authors. A benchmarking exercise on this specific material would be needed with different test methods to verify the accuracy and repeatability of the coefficient of friction measurements.

The results of this study is used in the next chapter for model validation.

Chapter 6

A 2D Finite Element model to predict the squeeze flow behaviour of ROS composites

6.1 Introduction

Following the work and conclusions of the previous chapters, a model was developed to predict the macroscopic squeeze flow of ROS composites under representative processing conditions. Based on the study presented in Chapter 3, it was determined that ROS seems to follow a yield stress behaviour, characterized by a viscous flow phase ending with a plateau. This behaviour can be challenging to model and a FE approach is required. Also, due to the problem complexity, the model was limited to a 2D approach. So, a FE model was developed to incorporate the ROS yield stress behaviour into a predictive tool that can relate sample geometry, strand size, material behaviour and processing conditions to the squeeze flow behaviour. An experimental campaign was also performed to validate the model for different strand size.

6.2 Objectives and structure

The primary objective of this chapter is to use the key findings and extended knowledge of the previous chapters to develop an FE model to predict the squeeze flow of ROS composites and to validate the model using experimental measurements. The secondary objective of this chapter is to perform a parametric study using the model to quantify the effect of the main processing and geometrical parameters, such as the applied pressure, the sample size and the strand size and then provide basic design guidelines for this novel material.

6.3 Model development

As a first step in the understanding of the macroscopic flow of ROS, the squeeze flow of a flat pre-consolidated rectangular plate is modelled. As discussed in the previous section, several deformation mechanisms occur during compression moulding of ROS. In order to avoid measuring pre-consolidation effects and packing stresses, pre-consolidated ROS samples were used for all the squeeze flow tests performed in this study. This was done to focus on the pure macroscopic squeeze flow behaviour. Also, in this thesis, the squeeze flow was restricted to one direction, by constraining two sides of the sample, thus reducing the problem to a two dimensional problem. The space dimension aspect was handled using the finite element method. Several difficulties appeared when solving the squeeze flow of a Bingham fluid, mainly the highly non-linear behaviour, the large deformation and the singular boundary condition imposed by the moving platen.

In order to overcome these challenges, COMSOL Multiphysics was used. This software can solve strongly coupled partial differential equations. It allows the definition of any analytical expressions for the viscosity term in Stokes equation. It can handle mesh large deformations and any additional scalar equations defined by the user. The whole system of equations is then fully coupled and can be solved simultaneously using robust non-linear algorithms.

The following sub-sections describe the model geometry, mesh large deformation resolution, boundary conditions and the material behaviour.

6.3.1 Geometrical domain

Figure 6.1 shows the geometrical domain used for the model. The light gray region corresponds to the pre-consolidated ROS flat panel. The sample has a rectangular cross-section and covers one-half of the mould cavity. Using the horizontal symmetry, only the bottom half of the sample and tool cavity are considered: the dotted region corresponds to the model domain that is meshed. The bottom half of the pre-consolidated sample covers half of the domain and the rest is initially filled with air.

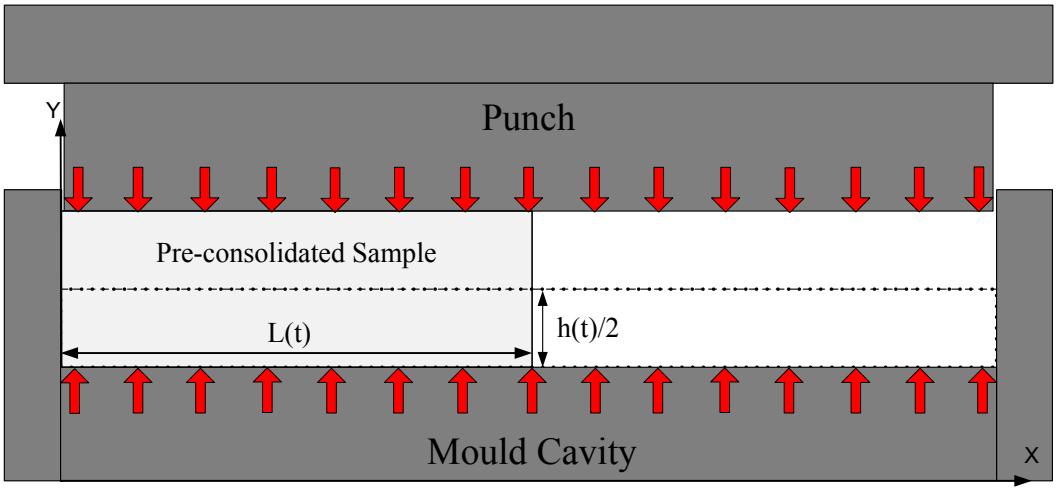

Figure 6.1: Geometrical domain for the 2D model. Red arrows represents the distributed load *F* imposed by the hot press.

6.3.2 Mesh and large deformation resolution

In order to deal with the large in-plane deformations associated with the squeeze flow of ROS, an original mixed Eulerian-Lagrangian approach was developed. In this case, out-of-plane deformations are much smaller than in-plane deformation. To avoid dealing with highly deformed mesh, an Eulerian approach was used for the in-plane direction.

The mesh was then kept fixed in the x-direction and deformed in the y-direction according to the closure of the mould. In the y-direction, the mesh deforms according to the calculated sample height at a given time step $h(t)$. At each time step, the deformed mesh coordinates $\boldsymbol{Y'}$ are simply updated by the following equation:

$$\boldsymbol{Y}' = \boldsymbol{Y}\left(\frac{h(t)}{h_i} - 1\right) \tag{6.1}$$

where h_i is the initial sample height and $\boldsymbol{Y}$ the reference mesh coordinates.

In addition, a level-set was used to track the in-plane position of the interface between material and air throughout the whole simulation. Initially, the interface was set in the middle of the mould cavity, corresponding to the preconsolidated sample edge.

Figure 6.2 shows the mesh and boundary conditions for the model. The domain was meshed with 7984 unstructured triangular elements. 2D triangular elements were automatically generated and refined around the initial position of the interface and near the mould cavity boundary. The mesh was separated in two domains with different material properties. The left domain has an equivalent viscosity given by equation (6.9) and the right domain has simply the constant Newtonian viscosity of the air (18.3×10^{-6} Pa-s).

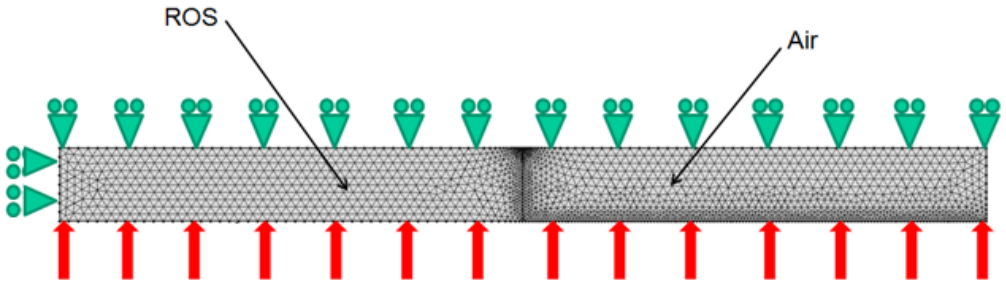

Figure 6.2: Mesh and boundary conditions. Rollers represent the symmetry boundary condition on the top edge and the fixed left edge. A level-set is defined at the interface between ROS and Air. A no-slip boundary condition is imposed at the bottom edge corresponding to the platen interface.

6.3.3 Boundary conditions

From the problem symmetry, only one half of the domain is considered in the model. Besides symmetry boundary conditions, the right edge of the domain is let free and a vertical displacement was applied on the top boundary corresponding to the symmetry plane:

$$\boldsymbol{v} = \frac{dh(t)/dt}{2} \, at \; y = h(t)/2 \tag{6.2}$$

The platen velocity $dh(t)/dt$ imposed on the top platen is an additional scalar unknown that is calculated at each time step with the platen force balance equation. The closing force F applied on the bottom boundary Γ is known, but the normal stress distribution at the boundary follows the force balance equation:

$$\int_{\Gamma} \boldsymbol{\sigma} \cdot \boldsymbol{e_y} \cdot \boldsymbol{e_y} dS = F \tag{6.3}$$

where $\boldsymbol{\sigma}$ is the total Cauchy stress tensor and $\boldsymbol{e}_y$ is the vertical normal vector to the boundary in contact with the bottom platen Γ. Eq. (6.3) is the last scalar equation that fully defines the problem boundary conditions.

Also, a no-slip boundary conditions was imposed at the interface with the bottom platen, such that:

$$\boldsymbol{u} = \boldsymbol{v} = \mathbf{0} \; at \; y = 0 \tag{6.4}$$

where $\boldsymbol{u}$ and $\boldsymbol{v}$ are respectively the horizontal and vertical velocity vectors. This no-slip condition was clearly observed in the experimental study of Chapter 4. It showed that the ROS Carbon/PEEK material sticks to the tool platens during squeeze flow tests.

6.3.4 Material behaviour

Because of the high viscosity of the composite melt, the inertia and gravity terms can be neglected, such that the local equilibrium reduces to:

$$\boldsymbol{\nabla} \cdot \boldsymbol{\sigma} = \mathbf{0} \tag{6.5}$$

Pre-consolidated ROS samples were used for all the squeeze flow tests performed in this study. This was done to focus on the pure macroscopic squeeze flow behaviour and avoid pre-consolidation effects. The material is then assumed incompressible:

$$\boldsymbol{\nabla} \cdot \boldsymbol{u} = \mathbf{0} \tag{6.6}$$

only the deviatoric stress

$$\boldsymbol{\tau} = \eta\dot{\gamma} \tag{6.7}$$

can be obtained from the kinematic (strain rate) and the total stress tensor $\boldsymbol{\sigma}$ is known to within a hydrostatic pressure p:

$$\boldsymbol{\sigma} = \boldsymbol{\tau} - p\boldsymbol{I} \tag{6.8}$$

Instead of the conditional visco-plastic behaviour, the smoothed exponential approach (see equation (2.5), Chapter 2) suggested by Papanastasiou [71] and used later [72] was assumed here. As a first approximation, the fluid was considered to behave as a Bingham fluid, i.e. the exponent n was set to 1, such that equation (2.5) reduces to:

$$\eta_{eq} = \eta_0 + \frac{\tau_Y\left(1 - e^{-m\dot{\gamma}}\right)}{\dot{\gamma}} \tag{6.9}$$

This way, the flow behaviour of ROS composites can be characterized by an equivalent Newtonian viscosity η_0 and a yield stress τ_Y. The exponent m is used to smooth the discontinuous yield stress behaviour. When m is increased to infinity, the equation converges to the ideal discontinuous behaviour.

6.3.5 Numerical implementation

The Stokes flow defined by equations (6.5) to (6.8) was solved using the *two phase flow* module in COMSOL Multiphysics. A mixed formulation was used for the velocity and pressure fields using a standard P2/P1 interpolation. A level-set tracked the interface between the two material phases. The transient problem was solved using the built-in time-dependent solver.

The force balance (6.3) was implemented using an additional physics (global algebraic equation), thus adding the scalar unknown $dh(t)/dt$ to the model.

The nonlinearity arising from the non-constant viscosity (equation (6.9)) was handled with the COMSOL built-in lumped Newton-Raphson solver. A constant damping factor of 1 was used. At

each time step a relative tolerance of $1x10^{-3}$ was reached. The maximum number of iteration was set to 25.

6.3.6 Initial values approximation

In order to help the non-linear solver converging on the first time step, initial values for the velocity field $\vec{U}$ were approximated using the analytical solution obtained for a Newtonian fluid. Considering a two dimensional transverse flow and using the lubrication assumption, as shown in Shuler and Advani [60], one can relate the the closure rate $dh(t)/dt$ to the applied load $F(t)$ and the Newtonian viscosity η. W, h and L are respectively the sample width, height and length.

$$\frac{dh(t)}{dt} = \frac{F(t)}{8\eta W}\frac{\mathrm{h}^3}{\mathrm{L}^3} \tag{6.10}$$

The velocity field $\vec{U}$ is defined using the following notation for horizontal and vertical components.

$$\vec{U} = \begin{pmatrix} u(x,y) \\ v(x,y) \end{pmatrix} \tag{6.11}$$

The velocity vertical component $v(x,y)$ can directly be expressed as a function of the closure rate $dh(t)/dt$ and the initial sample height h_0.

$$v(x,y) = -\frac{dh(t)}{dt}\frac{y}{h_0} \tag{6.12}$$

Assuming a Newtonian behaviour, and considering material incompressibility, an analytical expression for the horizontal velocity component $u(x,y)$ can be determined :

$$u(x,y) = \frac{3x}{h_0^2}\frac{dh(t)}{dt}\left(y - \frac{y^2}{2h_0}\right) \tag{6.13}$$

This provides an initial solution to the non-linear problem that is closer to the actual solution and enables the non-linear solver to converge on the first time step. More details of the mathematical operations that led to this latter equations are provided in Appendix C.

6.3.7 Converting final strain to flow distance

The model output provides the sample height evolution as a function of time. The final height can then be compared to the initial height h_i to obtain the final strain:

$$\varepsilon_f = 1 - h_f/h_i \tag{6.14}$$

The final strain is useful to quantify the deformation under given processing parameters. Although one might be interested to know the flow distance L_d, or in other words, how much distance the material travelled from its initial position.

Figure 6.3 shows the material initial and final configuration and the flow distance definition.

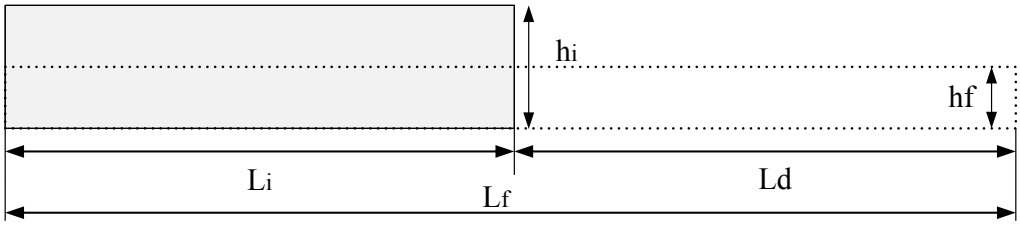

Figure 6.3: Material initial and final configuration and flow distance definition.

By calculating ε_f one can easily determine L_d, using material incompressibility, one can write:

$$h_i * L_i = h_f * L_f \tag{6.15}$$

By reorganization and substitution of equation (6.14) into (6.15), one can obtain an expression for L_f as a function of the final strain ε_f

$$L_f = \frac{L_i}{(1 - \varepsilon_f)} \tag{6.16}$$

Also, by definition the flow distance is simply the difference between the final length and the initial length:

$$L_d = L_f - L_i \tag{6.17}$$

Finally, reorganization and substitution of (6.16) into (6.17) leads to the following expression for the flow distance L_d:

$$L_d = \frac{L_i * \varepsilon_f}{(1 - \varepsilon_f)} \tag{6.18}$$

The flow distance is useful to determine the feature dimensions that can be filled with material for a given material and processing conditions.

6.4 Experimental procedures

6.4.1 Materials

The material used in this study is the same Carbon / PEEK pre-impregnated chopped tape composite as described in the previous chapters. In this Chapter, three different strand size was considered:

- Large: 25.4mm long by 6.35mm wide,
- Medium slender: 12.5mm long by 3.18mm wide and
- Small: 6.35mm long by 3.18mm wide.

6.4.2 Instrumented hot-press

The apparatus used to perform the squeeze flow tests presented in this chapter is the same that was presented in Chapter 3, with the exception that a picture frame was used to ensure a 1D flow and restrict the material inside the test section.

6.4.3 Test procedure

ROS preconsolidated flat laminates were used to perform all the squeeze flow tests presented in section 4. This ensured that consolidation effects at low load (packing stress and ISVC mechanisms discussed in Chapter 2, section 2.2.1) were not observed during the experiments but only the squeeze flow behaviour. The ROS samples used in this study were cut from 184 mm by 279 mm flat panels pre-consolidated by compression moulding. The laminates were made using a steel tool with a 184x279 mm cavity.

560g of material was used for each ROS laminate to reach an average thickness of 6.5 mm ±0.2 mm. Strands were added to the mould in small batches and shuffled manually each time to ensure random distribution and minimize their out-of-plane orientation. Then, the mould was closed and placed into a Wabash 100 ton hot press preheated to 395 °C. A thermocouple was placed into a hole on the side of the mould to measure and monitor the plate temperature during the cycle. A pressure of 22 bars was then applied and maintained during 15 minutes. The mould was then cooled down to 70 °C at an approximate rate of 12 °C/min and was removed from the press when the temperature dropped below 70 °C. The panels were trimmed and 50.8mm x 101.6mm samples were cut using a diamond blade saw.

The squeeze tests were all performed at 400 °C on the pre-consolidated 50.8 by 101.6 mm samples. The hot-press platens were coated with FREEKOTE 700-NC release agent before each tests to prevent material sticking to the platens and ease demoulding. The samples were placed against one edge of the picture frame, covering half of the bottom platen and the upper platen was moved down until a contacting force was measured. The MTS machine was set in force control mode. The contacting force (80-100N) was low compared to the applied force during the test (1 to 20 kN), ensuring no flow during the heating phase. The platens were then heated to 400 °C in about 15 min. Force control allowed for a compensation of the thermal expansion of the setup. An additional stabilization time of 10 min ensured isothermal conditions during the tests. A closing force according to the test matrix given in Table 6-1 was then applied in a one second ramp and maintained during 5 min. The press was cooled down using compressed air. The cooling rate was not controlled but measured to be approximately 15 °C/min. Finally, when the

temperature dropped below 143 °C, which corresponds to the glass transition temperature of PEEK, the press was opened and the sample ejected. Sample length, width and thickness were measured prior and after each squeeze flow test using a micrometer and caliper.

Table 6-1 shows the test matrix used to perform the tests described in this chapter. Three different strands size were tested and three different load levels were used for each strand size. The load levels are such that the material reaches the other end of the picture frame only at the highest load level.

Table 6-1: Experimental test matrix for the squeeze flow model validation

Strand scale	Strand Length (mm)	Strand Width (mm)	Applied Load (kN)
Small	6.35	3.18	1, 2, 5
Medium	12.7	3.18	2, 5, 10
Large	25.4	6.35	5, 10 ,20

6.5 Experimental results and model validation

In this section, the experimental and modelling results obtained following the procedures presented in section 6.3 and 6.4 are presented and discussed.

6.5.1 Viscous parameters determination

The equivalent viscosity and yield stress of the ROS melt depend on the strand size. For the three different strand size tested, these two parameters were determined by manually fitting the experimental and modelled sample height evolutions for the highest load level. The obtained

parameters, given in Table 6-2, were then used as input to predict the sample height reduction for the other two load levels.

The viscosity values found increased with strand size, where the viscosity of large and medium strands were respectively five and four times higher than the viscosity of small strands (42 and 30 compared to 8kPa-s). The yield stress values also increased with strand size, but less drastically. It increased by 15% between small and medium strands and by 86% between medium and large strands.

In this study, small and medium strands had the same width (3.18 mm), but medium strands were two times longer (12.7 compared to 6.35 mm). By comparing the viscosity and yield stress values found for these two strand size, it is clear that the strand length strongly affected the melt viscosity. Indeed, strands twice as long resulted in viscosity values four times higher. Whereas, for the yield stress values, the difference between small and medium strands was less significant. However, the yield stress values found for large strands were significantly higher, than small and medium strands. Large strands were longer than small and medium strands, but also wider, suggesting that the yield stress was more affected by strand width than strand length.

Table 6-2: Summary of the viscous parameters determined using the model

Parameter	Small Strands	Medium Strands	Large Strands
Applied Load F (kN)	1, 2, 5	2, 5, 10	5, 10, 20
Viscosity η_0 (kPa-s)	8	30	40
Yield Stress τ_Y (kPa)	12.6	14.5	27.1

Figure 6.4 shows a comparison of the experimentally measured and predicted sample height for the three load levels tested, for the medium strands case. The R^2 coefficient was over 97% for all the nine test cases. A good agreement was observed between predicted and measured sample height as a function of time, especially for the final sample height. Also, the model predicts the plateau behaviour of ROS that was observed in a previous study and was not captured by purely viscous models [89]. The viscosity values that were found determined the sample height reduction rate $dh(t)/dt$ in the first seconds of the squeeze flow test, whereas the yield stress values influenced the onset of the plateau and the final strain value. When the load level is relatively low, such as the 2kN load case shown in Figure 6.4, the sample height reduction is lower and the yield stress value restricts the final strain to only 20%. For medium strands, at a load of 10kN, most of the flow occurred in the first 30 seconds and the final strain calculated using equation (6.14) was nearly 50%.

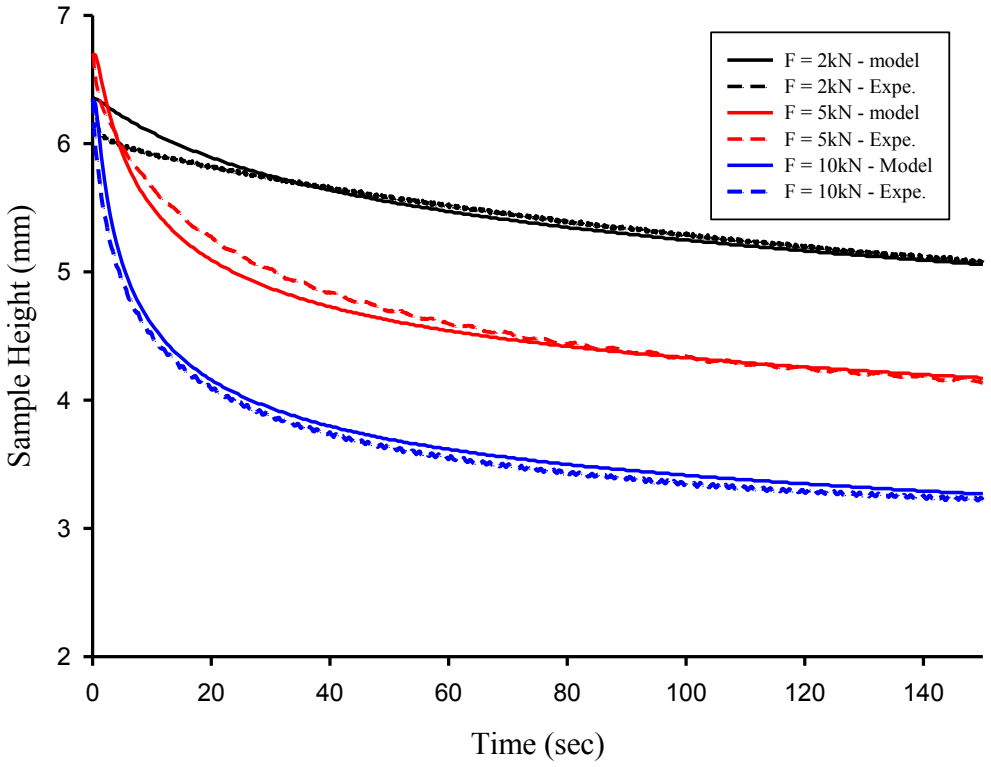

Figure 6.4: Comparison of Sample height model prediction and experimental measurements for medium strands. The model is accurate to predict the final sample height.

6.5.2 Flow front visualization

The flow front position was tracked using the level-set interface between ROS and air as defined in section 6.3.2. The level-set position was smoothed for numerical implementation. The average X and Y coordinates of the interface were extracted at each time step as contour plots. Figure 6.5 shows the predicted progression of the flow interface as a function of time for the 10kN load case with medium strands. The mesh deforms according to the prescribed deformation in the thickness direction (equation (6.1)), and the level-set interface advances with time in the in-plane direction. Since symmetry boundary conditions were used, half of the flow profile was modelled and is shown on Figure 6.5.

At $t = 0\ s$, the interface position corresponds to the right edge of the ROS sample position (0,0508 m). Then, when the load is increased to 10kN at $t = 1\ s$, the flow advances following a plug-flow profile and the velocity is maximum at the symmetry plane. Then, the flow front velocity slowly reduces as the sample height decreases. At $t = 300\ s$, the average position of the flow front has almost fully reached the right boundary and the out-of-plane strain is nearly 50%. The dashed line represents the average final X-position of the flow front that was measured experimentally for the 10kN load case with medium strands. Overall for the nine test cases, the final flow front position is consistent with experimental measurements, with less than 10% difference.

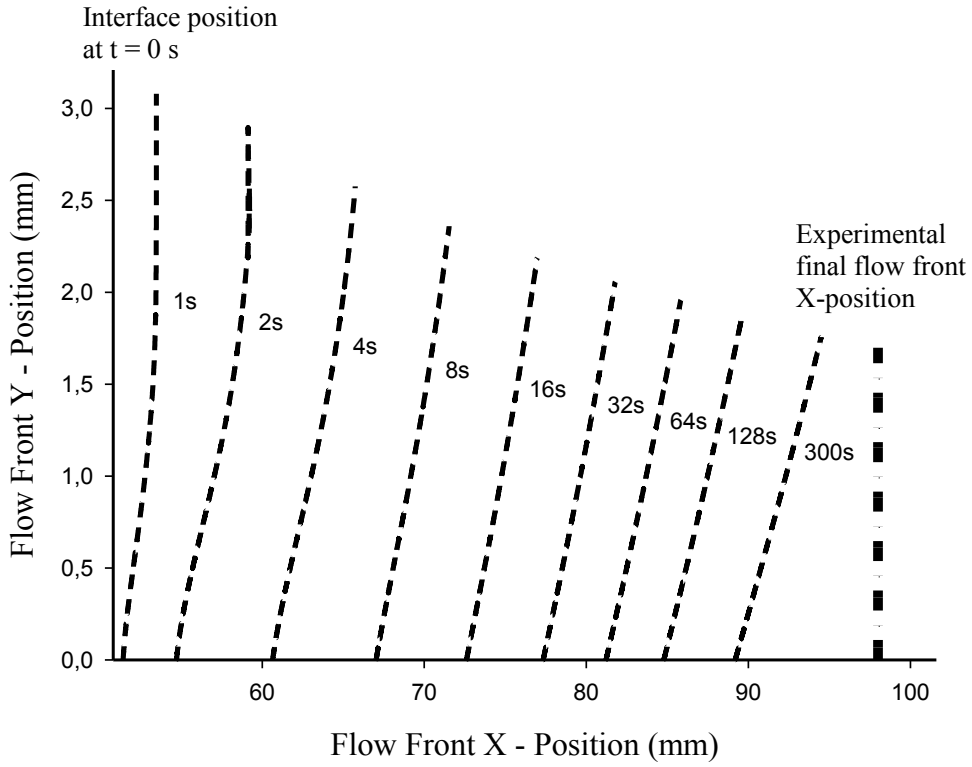

Figure 6.5: Progression of the flow interface position as a function of time for a closing force of 5kN with small strands. In this case, the mould cavity is almost filled with ROS after approximately 300s for the given case shown here.

Figure 6.6 shows a comparison of the flow front position for the first two seconds of the simulation, for the three strand size used in this study, and the 5kN load case. Since the initial height of each sample was slightly different, the Y-position was normalized with respect to the initial sample height, where 1 corresponds to half of the initial sample height. The flow front progressed more quickly for smaller strands, since the viscosity and yield stress were lower. For small strands, after 1 second the flow front progressed more than large strands did after 2 seconds. Also, the shape of the plug flow profile in the first seconds is strongly influenced by the strand size. For medium and large strands, the flow profile is more uniform, while for small strands the deformation is much larger in the middle of the sample, especially after 2 seconds.

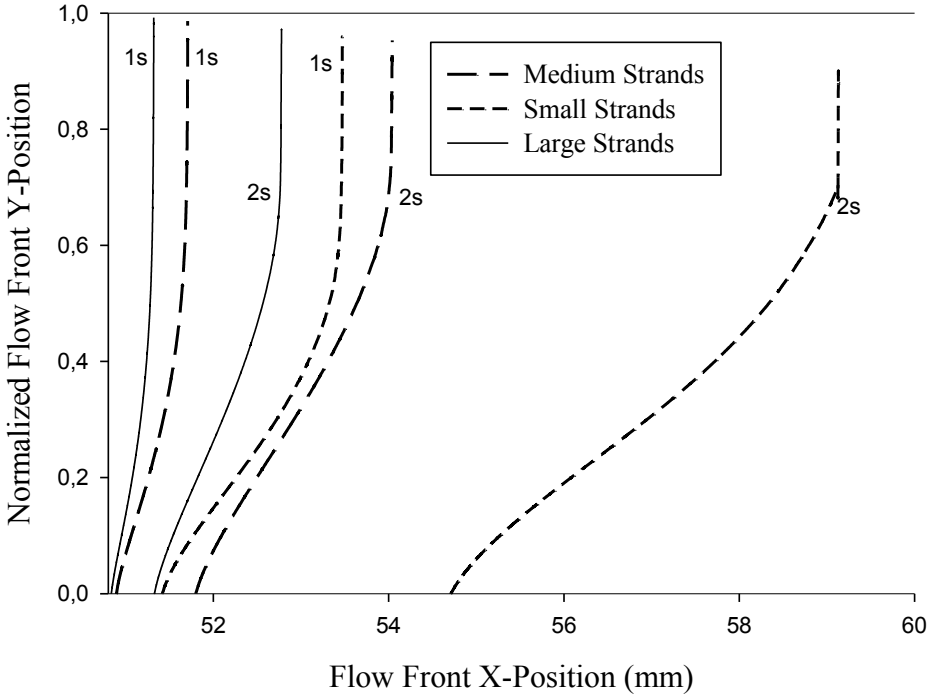

Figure 6.6: Comparison of the flow interface position during the first two seconds for small, medium and large strands for the 5 kN load case. A Plug-Flow profile can be observed during the first seconds.

The flow progression and its final position is also consistent with experimental measurements, as shown on the photograph of Figure 6.7c). Figure 6.7a) and b) also show a top view of the deformed samples for the medium strand case, respectively for the 2 and 5kN load levels. Overall, the final flow front position matches the experimental results for all the cases. Nevertheless, some edge effects were experimentally observed, due to material sticking on the edges of the picture frame used to restrict the flow to one direction. This edge effect was not considered in the model, but overall the average final flow position was consistent.

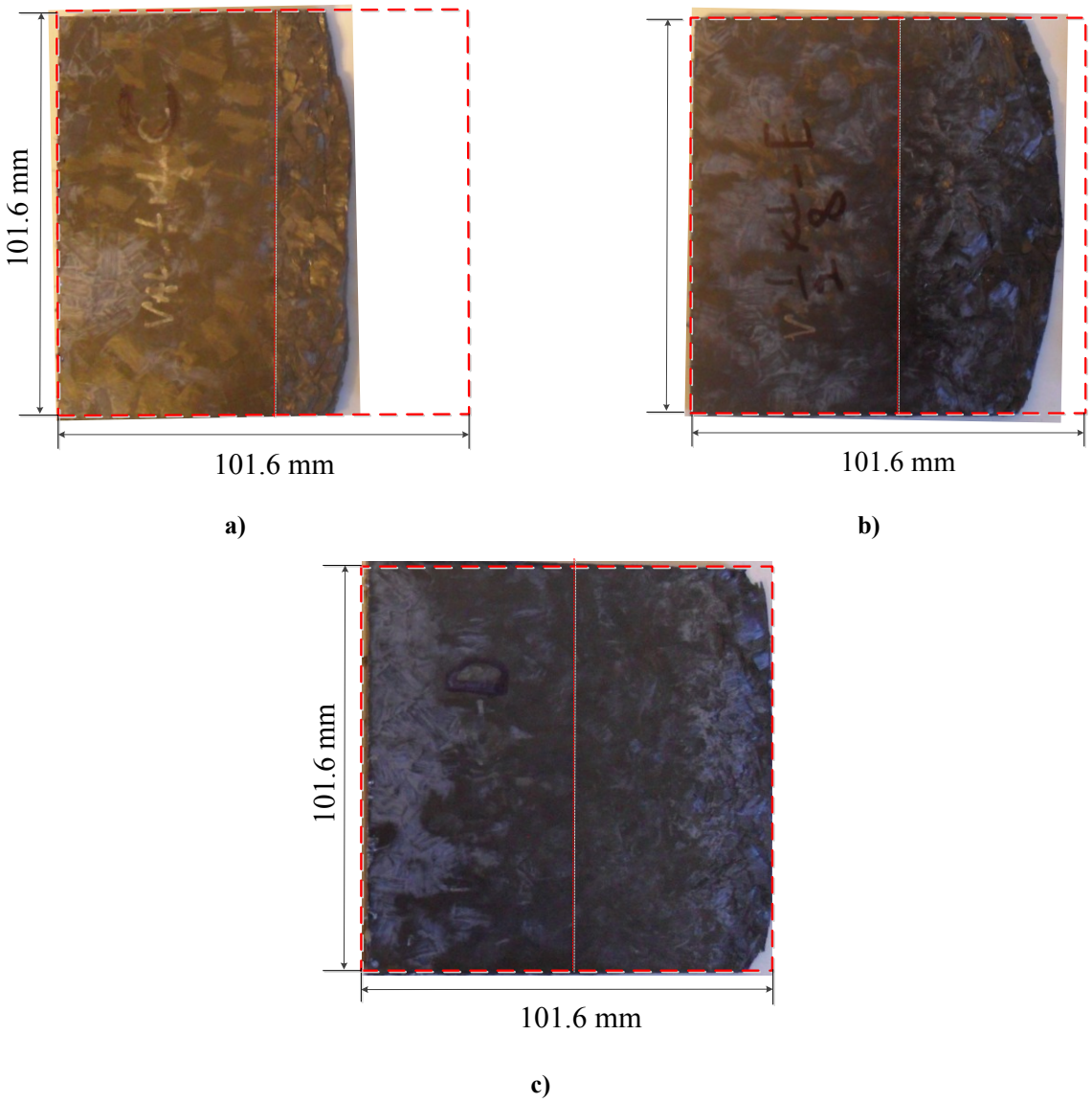

Figure 6.7: Photograph of the medium strands samples after the squeeze flow test. a) 2.5 kN b) 5 kN c) At 10 kN the whole tool cavity was filled, except for small empty regions in the corners.

6.5.3 Strand size effect on viscosity and yield stress

Figure 6.8 shows a comparison of the sample experimental and predicted sample height as a function of time, for the three load levels, for small strands. Again, the average error was below 3% between the predicted and experimentally measured values. By comparing Figure 6.4 and 6.8, for medium and small strands respectively, it is clear that strand length has a significant effect on the material viscosity and yield stress behaviour. For a load level of 5kN, the slope,

corresponding to the closure rate $dh(t)/dt$, is much higher in the first seconds for small strands than for medium strands. For small strands, 75% of the total deformation already occurred after 20 seconds, while for medium and large strands it takes around 40 and 60 seconds, respectively, to reach a similar level of deformation.

This behaviour is due to the equivalent viscosity η_0 that influences the initial closure rate $dh(t)/dt$. For a given load level, an increase of η_0 led to a decrease of $dh(t)/dt$. As mentioned earlier, the value found for the viscosity of medium and large strands was around 4 and 5 times higher compared to small strands. This shows the influence of the strand size on the viscosity, and thus, the flow rate in the first seconds of the squeeze flow test.

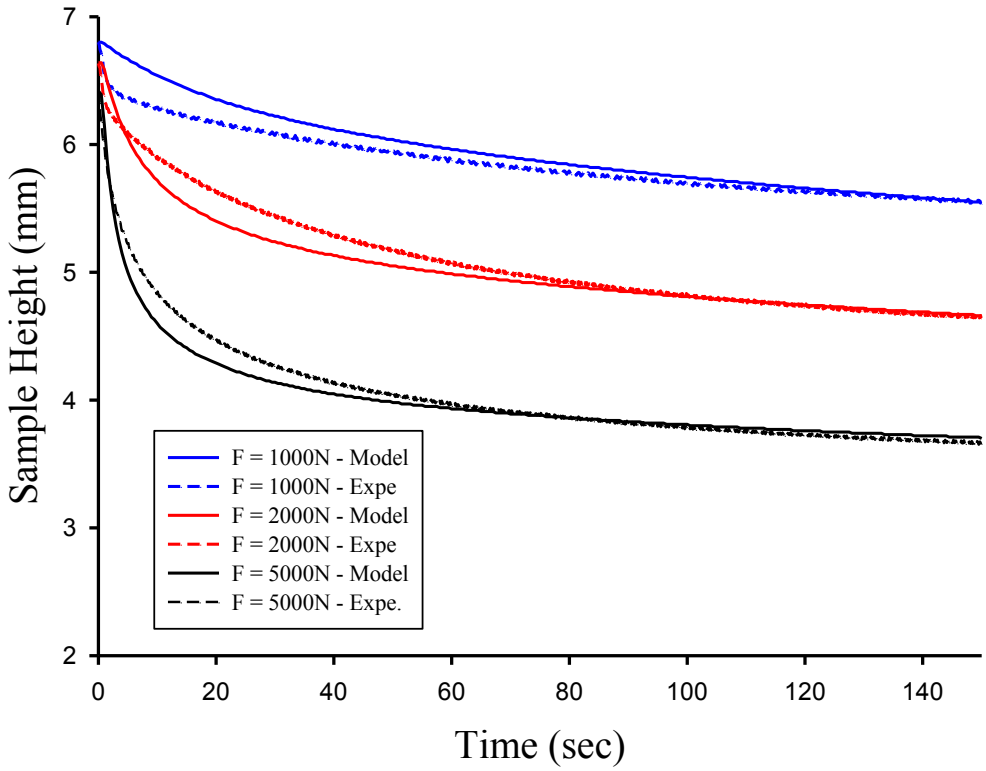

Figure 6.8: Comparison of sample height model prediction and experimental measurements for small strands. The viscosity and the yield stress values are lower for small strands.

Finally, Figure 6.9 shows a summary of the final strain achieved for the three load levels tested in this study, and the three different strands size, based on equation (6.14). The experimental results were compared with the predicted values. Again, agreement was found for the final predicted strain values with a R^2 of 99%. It is important to note that the strain was restricted to a maximum of 50% in this study, because of the cavity dimension.

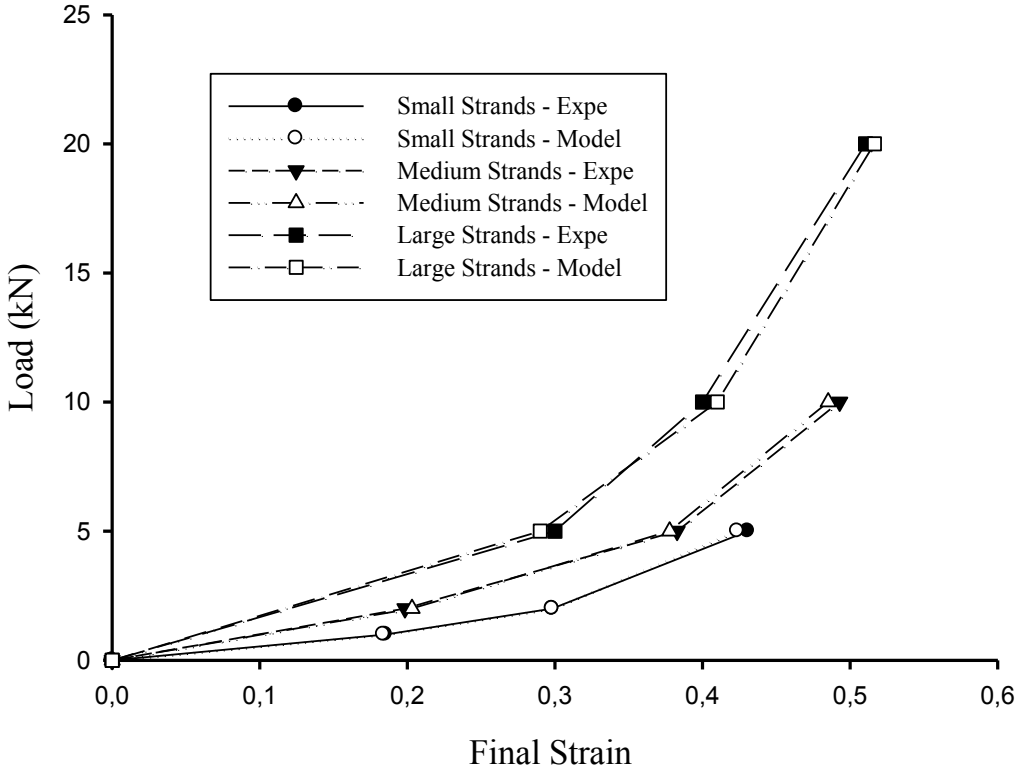

Figure 6.9: Comparison of Load vs. Strain for experimental results and model prediction. A maximum of 50% strain is achieved since the flow was restricted using the picture frame.

The strand size effect is clearly shown on Figure 6.9: under a load of 5kN the final strain reached for large strands is around 0.26 while for small strands it is above 0.4. This shows that the strand size has a large effect on the yield stress, and thus, the final strain. This yield stress increased with strand size was observed on similar materials. Indeed, authors showed that the yield stress of short fibre suspensions and fibre bundle suspensions was greatly affected by the fibre or bundle aspect ratios. They found that larger bundle suspensions have higher yield stress [55, 57]. It is also known that for fibre bundle suspensions, fibre-fibre interactions such as dry and

lubricated friction mechanisms are affecting the composite melt viscosity and yield stress. So, it is believed that these mechanisms are likely to affect the yield stress behaviour of ROS composites as well. The aspect ratio and dimension increases between small, medium and large strands leads to larger contact areas between the strands, and therefore, higher friction components, which directly influences the yield stress.

Using the predictive model developed in this study, the strand size increase resulted directly in an increase of the viscosity and yield stress values that were determined. Finally, the viscoplastic behaviour proved accurate at predicting the experimental final strain in squeeze flow of ROS. The model is used in the next section to construct design charts that predict the processing of ROS simple flat parts.

6.5.4 Coefficients of Friction model prediction and comparison with experimental data

This sub-section shows a first effort done to relate the material yield stress to the inter-ply friction mechanism. From the results of some studies found in the literature [55, 57], a reasonable first approximation is to assumed that the yield stress τ_Y is simply a function of the effective normal pressure P_{eff}, and the coefficient of friction c_f:

$$\tau_Y = c_f P_{eff} \tag{6.19}$$

where P_{eff} is defined as the effective pressure on the sample, similar to the definition used in Chapter 3, section 3.4, but adapted to the case presented here:

$$P_{eff} = \frac{F}{W \cdot L(t)} \tag{6.20}$$

where W is the sample width, $L(t)$ the sample length and F the applied load. In this study, a constant yield stress value was considered for each strand size tested. So, using the yield stress

definition (6.19), it is possible to relate the coefficient of friction c_f to the yield stress and the effective pressure:

$$c_f = \frac{\tau_Y \cdot W \cdot L(t)}{F} \tag{6.21}$$

Also considering material incompressibility, $L(t)$ is directly calculated from $h(t)$, which leads to the following expression for c_f:

$$c_f = \frac{\tau_Y \cdot W \cdot h_i \cdot L_i}{F \cdot h(t)} \tag{6.22}$$

Using the definition of equation (6.22), the predicted coefficient of friction can be calculated at each time step and increases when $h(t)$ decreases.

However, as shown in the previous chapter, the coefficient of friction strongly depends on many parameters, mainly normal pressure, pulling velocity and ply orientation. So, it is challenging to incorporate all these effects in the yield stress definition. As a first approximation, the coefficients of friction were then calculated only based on equation (6.22).

Figure 6.10 shows a comparison between the coefficients of friction predicted for the three load levels used for model validation, for small and medium strands, and the experimental results obtained from the study presented in Chapter 5, at 5 and 20 bar. The predicted coefficients of friction were taken at the final time step of each of the six nominal cases, where the coefficients of friction are maximum. The values were plotted with respect to the average velocity at that time, which are very low (around 0,001 mm/s) Even though there is some variability in the experimental results, the calculated coefficients of friction are in the order of magnitude of the experimental trends that was found. It shows that, indeed, the yield stress is related to the coefficient of friction, which is highly variable depending on processing conditions. However, an extensive characterization of this inter-ply coefficient of friction under various processing

conditions, and ply orientations coupled with a more accurate definition of the yield stress, would be a next logical step to improve the accuracy of the model predictions.

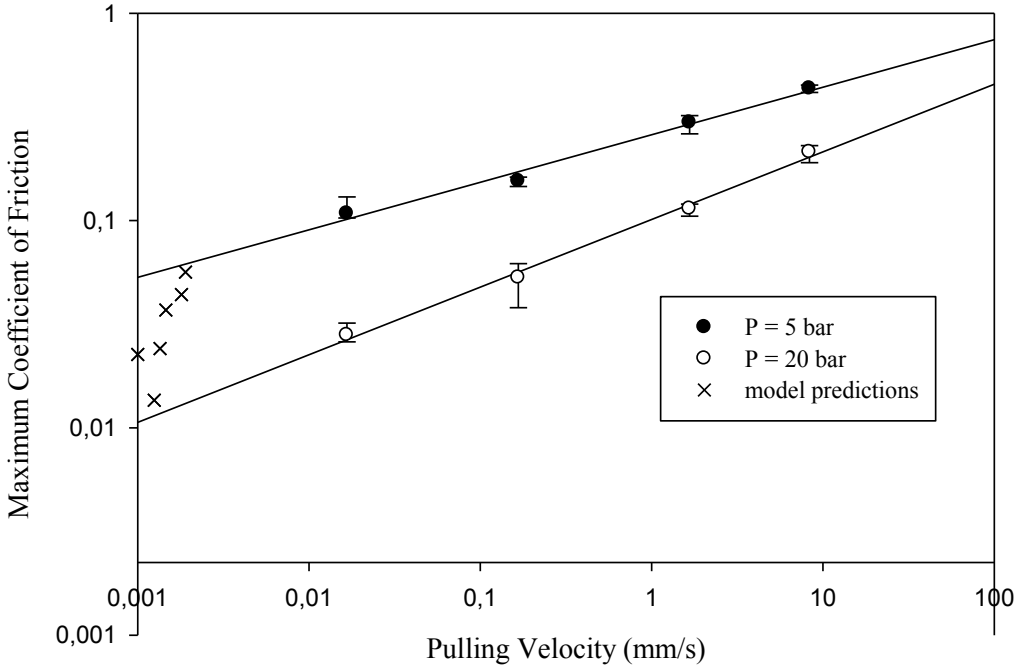

Figure 6.10: Comparison between the maximum coefficient of frictions measured experimentally and predicted with the model.

6.6 Applications

In this section, the model was used to perform a parametric study of the squeeze flow in order to predict the final strain, and thus, the flow distance, as defined in section 6.3.7. This provides a tool to improve the design of simple parts made with ROS composites.

6.6.1 Dimensional analysis

First, to identify the parameters that dictates the flow behaviour, a dimensional analysis was performed. Based on the material fluid behaviour (equation (6.5) to (6.9)), dimensionless variables were defined:

Dimensionless $x^*$and y^* coordinates were defined as:

$$x^* = \frac{x}{L_i}$$
$$y^* = \frac{y}{L_i} \quad (6.23)$$

Also dimensionless sample height h^* was defined as:

$$h^* = \frac{h}{h_i} \quad (6.24)$$

Dimensionless time t^* was defined as:

$$t^* = \frac{t}{t_c} \quad (6.25)$$

where t_c is the characteristic dwell time of a squeeze flow test (5min). When applying these dimensionless variables to the squeeze flow problems for given material properties (η_0, τ_Y) the system of equation (6.5) to (6.9) is reduced and the number of governing parameters can be reduced to only two: the aspect ratio between the initial sample height h_i and initial sample length L_i:

$$\frac{h_i}{L_i} \quad (6.26)$$

and the initial pressure applied on the sample:

$$\frac{F}{WL_i} \quad (6.27)$$

6.6.2 Design charts

Using the two parameters described by equation (6.26) and (6.27), twenty-five case studies were generated using the model for each strand size, using h_i/L_i ratios of 0.05, 0.1, 0.15, 0.2 and 0.25,

and initial pressures of 5, 10, 20, 40 and 80 bars. For each strands size, the charts were generated using the viscosity parameters determined in the previous section (see Table 6-2).Figure 6.11, 6.12 and 6.13 are respectively presenting the design charts for the different strand size. Isovalues of the out-of-plane final strain calculated using equation (6.14) are plotted for each combination of the aspect ratio h_i/L_i and the initial pressure F/WL_i.

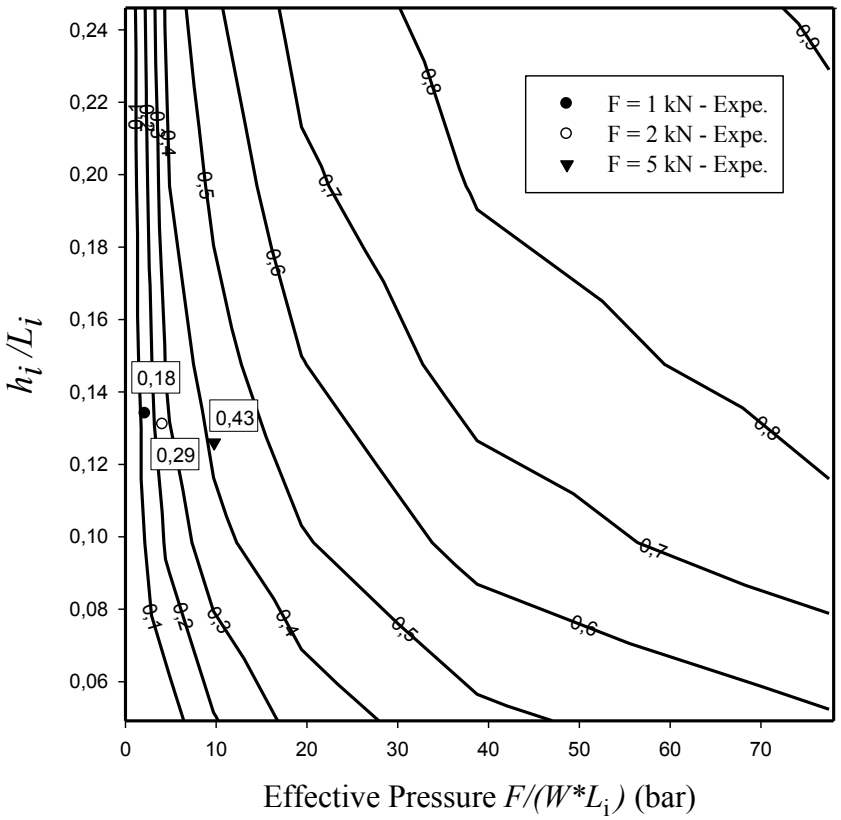

Figure 6.11: Design chart for small strands (6.35 x 3.18mm). The z values corresponds to the out-of-plane final strain obtained for a given effective pressure and initial sample height over length aspect ratio. The strain values measured experimentally are indicated for the three load level.

The initial sample aspect ratio h_i/L_i and the initial pressure F/WL_i was calculated for the nine experimental test cases of this study. The aspect ratio ranges between 0.125 to 0.134 for the nine cases and the initial pressure between 3.88 bar (for 2kN) and 19.38 bar for 10kN load levels. Using the design charts of Figure 6.11 for small strands, the final strain can be predicted as a function of the initial pressure and aspect ratios. From the results showed in Figure 6.11, the final

strain values are approximately 0.15, 0.26 and 0.41 for the 1kN, 2kN and 5kN load cases, respectively. These values are in good agreement with the experimental final strain obtained for these three cases with an average relative error of 7% (see Figure 6.10). The final strain was also predicted for the medium and large strands test cases, as shown in Figure 6.12 and Figure 6.13.

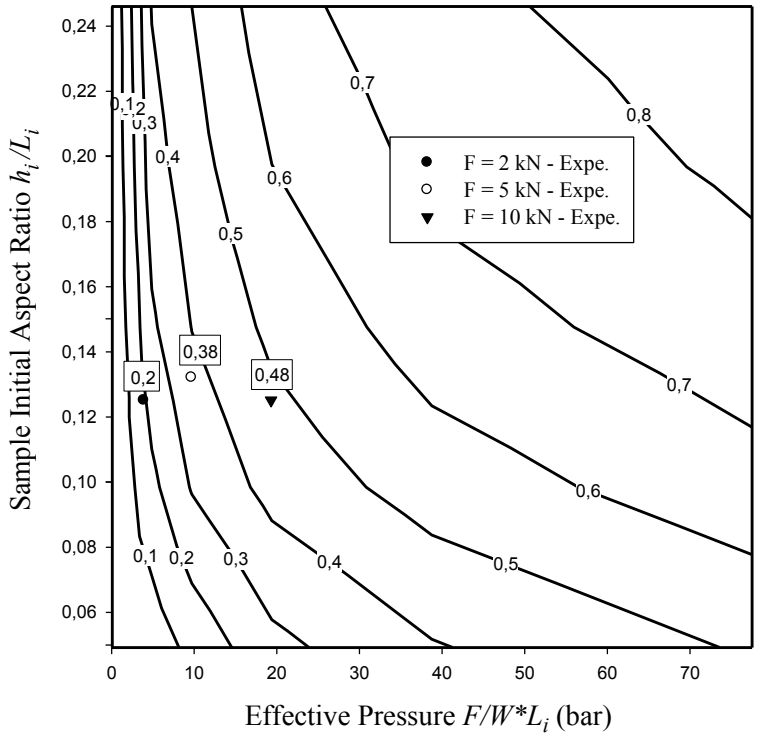

Figure 6.12: Design chart for medium strands (12.7 x 3.18mm). The z values corresponds to the out-of-plane final strain obtained for a given effective pressure and initial sample height over length aspect ratio. The strain values measured experimentally are indicated for the three load level.

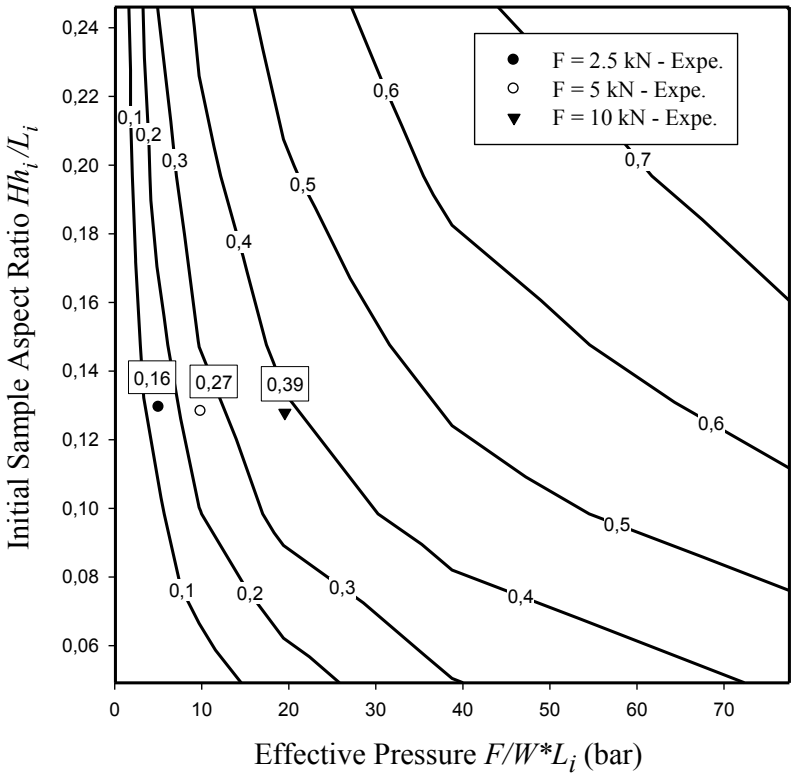

Figure 6.13: Design chart for large strands (25.4 x 6.35mm). The z values corresponds to the out-of-plane final strain obtained for a given effective pressure and initial sample height over length aspect ratio. The strain values measured experimentally are indicated for the three load level.

Overall, the relative error between the predicted final strain using the design charts and the experimental measurements was around 5% for the nine test cases. This difference between the predicted values and the experimental measurements is slightly higher using the design charts, compared with the validation cases presented earlier. This is due to the fact that charts were constructed based on different aspect ratios and initial pressures, compared to the validation cases presented earlier that were generated for the exact sample dimensions and load levels tested experimentally. It validates the dimensional analysis performed in this study, and shows that the squeeze flow is mainly governed by two parameters: the initial sample aspect ratio and the effective initial pressure. These design charts were accurate to predict the final strain of pre-consolidated flat samples deformed by squeeze flow, using different strand size and different load levels. This provides basic guidelines for the processing of ROS composite flat panels.

6.6.3 Case study: design of a ROS composite L-bracket using the charts

As an example of use for the charts, a case study of the actual design of an L-bracket made with ROS Carbon/PEEK is presented. This case study was based on the work of co-author and collaborators [19, 90], who studied the forming of a Carbon/PEEK ROS L-Bracket with a rib feature. Figure 6.14 presents a schematic of the L-Bracket mould and the ROS material initial positions, prior to compression moulding. It shows that initially, most of the mould is already filled with strands, but there are short shots in the flanges of the bracket that will be filled during moulding. This problem can be seen as the squeeze flow of a flat sample, if packing mechanisms are neglected and the composite melt is considered purely as a Bingham fluid. Based on the geometry of the L-Bracket tool and the material quantity, it was roughly estimated that 80% of the two flanges was already filled with material before moulding. So, a final strain of around 0.2 is required to completely fill the flanges. It is important to note that this estimate is based on visual observation only and the actual initial filling percentage is hard to measure accurately. So, this case study is a first proof of concept and further investigation would be required to validate the applicability of the charts to a wide range of dimensions.

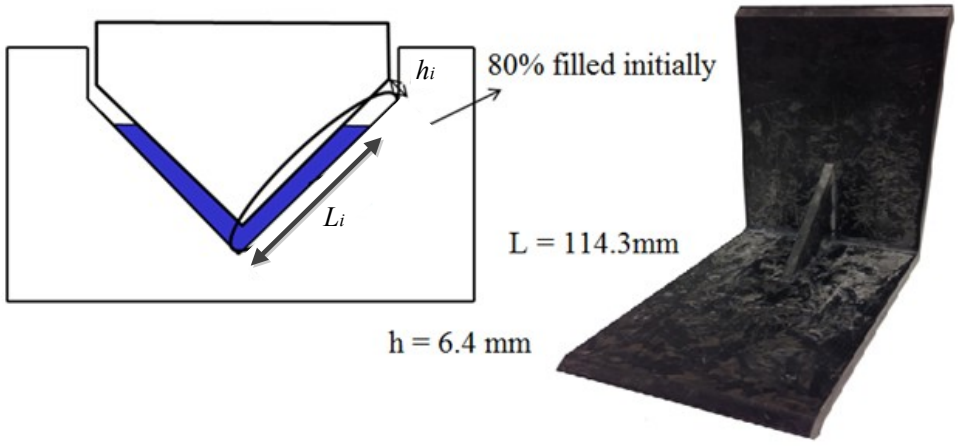

Figure 6.14: a)Schematic of the L-Shape mould and the initial material configuration prior to compression moulding. b) Photograph of the Carbon/PEEK ROS L-Bracket.

For this part, the final flange length is 114.3mm long, by 6.4mm thick, so the estimated initial length occupied by the material (prior to squeeze flow) L_i is 91.44mm (80% of 114.3mm) and

the estimated initial height h_i is 7.68mm (120% of 6.4mm), again by considering material incompressibility.

With those dimensions, the ratio between the initial material height and length h_i/L_i is around 0.08, and a final strain of 0.2 is desired. So, using the design charts of Figure 6.11, it shows that one needs to apply a minimum pressure of approximately 4 bar, if small strands are used. Also, if medium or large strands are preferred for the same geometric ratio of 0.08, the pressure needs to be increased to around 6 bar for medium strands and 15 bar for large strands. It shows the required pressure to completely fill a part, based on the part geometry and material initial placement. The minimum pressure predicted from the model is sufficient to completely fill the part; however, one might need to increase the pressure to ensure a good consolidation quality and low void content [19, 90].

6.7 Chapter conclusions

This chapter presented the development, implementation and application of a novel model to predict the squeeze flow of preconsolidated ROS Carbon/PEEK composites. The material was considered as a homogeneous viscoplastic medium. The fluid problem was solved using a modified Papanastasiou yield stress behaviour. An instrumented hot-press was used to perform squeeze flow tests under controlled conditions.

The experimental results showed good agreement with the model predictions: **ROS behave has a yield stress viscoplastic fluid with two governing parameters: the equivalent Newtonian viscosity and the yield stress value**.

The equivalent viscosity and the yield stress were obtained for three different strand sizes. **The larger the strands the higher the yield stress and the equivalent viscosity.** It suggests a strong relationship between the strand length and the equivalent fluid parameters.

The model was used to generate design charts that relate the geometrical and processing parameters (sample length, width, depth and applied load) to the final strain that can be achieved for this material. These design charts can be used as guidelines to predict the flow distance and avoid short shots where there are intricate part features.

Chapter 7

Conclusions

7.1 Scientific contributions

The research work presented in this thesis has led to different contributions to the knowledge and literature on the processing of ROS composites. The main contributions are presented hereunder.

1. **An extensive experimental characterization of the macroscopic squeeze flow of ROS composites was performed.** Squeeze flow tests have been performed on four different strand size, from small 6.35 by 3.18 mm strands to large 25.4 by 6.35 mm strands. The test was also performed on UD samples and a one dimensional model was adapted from the existing literature. It was found that both ROS and UD composites behave as a yield stress fluid when subjected to high pressure and large strain. The material follows a non-Newtonian behaviour in the first seconds of the test and starts to yield when subjected to large strain (> 50%).
2. **A new method for analyzing the meso-scopic and macro-scopic deformation mechanisms of ROS composites using X-Ray microtomography was developed.** Marker strands coated with conductive silver paint were incorporated in pre-consolidated ROS flat panels to track the changes in the meso and macro-structure. The samples were scanned before and after the squeeze flow tests under different load levels. It was found

that the material does not slip on the mould platen during squeeze flow. Also, transverse deformations at the strand scale were observed and quantified. Markers located at the bottom of the samples did not deform while top markers generally experienced the highest transverse deformations. The method allowed both two and three-dimensional analysis. It was also applied to a real three-dimensional ROS part.

3. **A two-dimensional FE model using an original mixed Eulerian-Lagrangian approach was developed to predict the squeeze flow of ROS composites.** The model was validated with experimental results and showed good agreement. It was used to determine the two material parameters governing the flow of ROS: the yield stress and the viscosity. The study showed that yield stress and viscosity both increases with strand size. The model is useful to predict the amount of pressure required to fill a certain cavity, based on the part aspect ratio and the material parameters. Design charts were generated using the model, these can provide basic guidelines for the processing of ROS parts. It was demonstrated using a simple case study, consisting of an L-Bracket. The model can predict the minimum pressure required to fill the part.

These contributions have directly led to scholarly literature on the processing of ROS composites, in the form of conference papers [13-15, 91] and submitted journal articles [89].

7.2 Future work

The results of this thesis highlighted several topics of interest for future work, the main ones are listed below:

1. **An automated image analysis procedure could be developed to extract markers position, orientation and deformation using the X-ray micrographs.** The work presented in Chapter 4 showed that relevant information on the macroscopic and mesoscopic flow mechanisms can be obtained using marker strands an microCT. All the measurements presented in this thesis were done manually using the image analysis software provided with the microCT equipment. However, this could be automated with an image analysis algorithm. This would improve the non-destructive inspection methods

for ROS composites. It could help to automate the inspection of complex parts and identify strands orientation and deformation at critical locations in the part.

2. **An extensive study of the inter-ply friction mechanism could be performed.** In the thesis, this mechanism was studied under a limited number of parameters, namely, the pull-out velocity and the normal pressure. However, due to the high sensitivity of the coefficient of friction on the test method and parameters, the test fixture needs upgrades to improve the results repeatability under a wider range of processing conditions. Thus, an extensive study for different ply orientations, processing temperature, normal pressure and pulling velocities could be performed to improve the understanding of this mechanism. It was found that the material yield stress is likely to depend on the inter-ply friction; thus, a better understanding of the latter mechanism would improve the overall knowledge on this material.
3. **The squeeze flow model may be extended to incorporate other deformation mechanisms.** Indeed, it was considered that the material was pre-consolidated prior to squeeze flow, and thus, pre-consolidation effects were not included in the model. In the actual compression moulding process, the bulk material is directly placed in the mould, and pre-consolidation effects and squeeze flow are likely to affect each other. The integration of both phenomenon in one model could lead to more accurate predictions of the flow behaviour, improve the understanding of ROS, and thus, help process optimization and complex parts design.
4. **The squeeze flow model may be extended for more complex geometries, such as T or L-shape parts.** As a first step, the model was developed to predict the forming of flat geometries and considered that material flowed in only one direction. However, when forming complex parts the material may undergo in-plane and out-of-plane flow, and thus, the present model cannot completely predict the forming of these complex shapes. An extension of the model to three-dimensional features would be a powerful design tool.

Appendix A - Nomenclature

A.1 List of symbols

c_f	Coefficient of friction
F	Force
F_n	Normal force
F_t	Tangential force
h_i	Initial sample height
h_f	Final sample height
$h(t)$	Sample height at time *t*
$dh(t)/dt$	Sample reduction rate at time *t*
I	Beam intensity of X-rays
I_0	Beam intensity of unattenuated X-rays
L_d	Flow distance
L_i	Initial sample length
L_f	Final sample length

$L(t)$	Sample length at time *t*
K	Consistency index in the Hershel-Bulkley model
m	Smoothing exponent in Papanastasiou model
n	Power law exponent and Carreau model exponent
P	Pressure
P_{eff}	Effective pressure
P_{min}	Minimum pressure
t	Time
t_c	Critical viscous time
t_{min}	Minimum time
V_x	Horizontal velocity component
V_y	Vertical velocity component
W	Sample width
α_μ	Viscous strain fraction
γ	Shear rate
ε	Strain
ε_f	Final strain
ε_{yy}^{th}	Transverse coefficient of thermal expansion

ε_t	Meso-scopic Transverse Deformations
η_0	Equivalent viscosity
$\eta_{att,ave}$	X-ray linear attenuation coefficient
λ	Time relaxation constant in Carreau model
μ	Newtonian fluid viscosity
$\boldsymbol{\sigma}$	Cauchy stress tensor
ρ	Density
τ_Y	Yield stress

A.2 List of acronyms

ALDF	Aligned Long Discontinuous Fibres
BMCs	Bulk Moulding Compounds
CF	Continuous Fibres
FPP	Frame Per Projection
ISVC	Inter-Strand Void Content
LDF	Long Discontinuous Fibres
PEEK	PolyEther Ether Ketone
PEKK	PolyEther Ketone Ketone
PP	Polypropylene

ROS	Randomly-Oriented Strands
SF	Short Fibres
SMCs	Sheet Moulding Compounds
UD	Unidirectional Fibres

Appendix B - Additional details on the instrumented hot press and flat panel moulds

This section provides the most relevant engineering drawings for the instrumented hot press machined parts and the flat panel mould used in Chapter 3, 4 and 6.

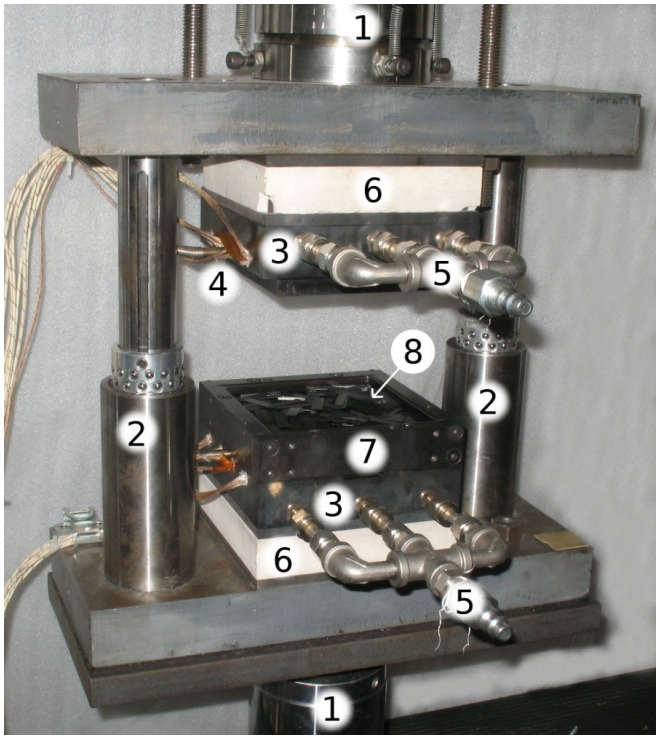

Figure B-1: Instrumented hot press. (1) MTS compressive fixture. (2) Ball-bearing die set to ensure alignment. (3) H13 steel 100mm x 100mm platens (4) 500W Heating cartridges. (5) Cooling channels using compressed air. (6) Ceramic layer to ensure thermal insulation. (7) A picture frame can be used to pre-consolidate flat panels. (8) Material placed inside the mould.

B.1 Instrumented hot press drawings

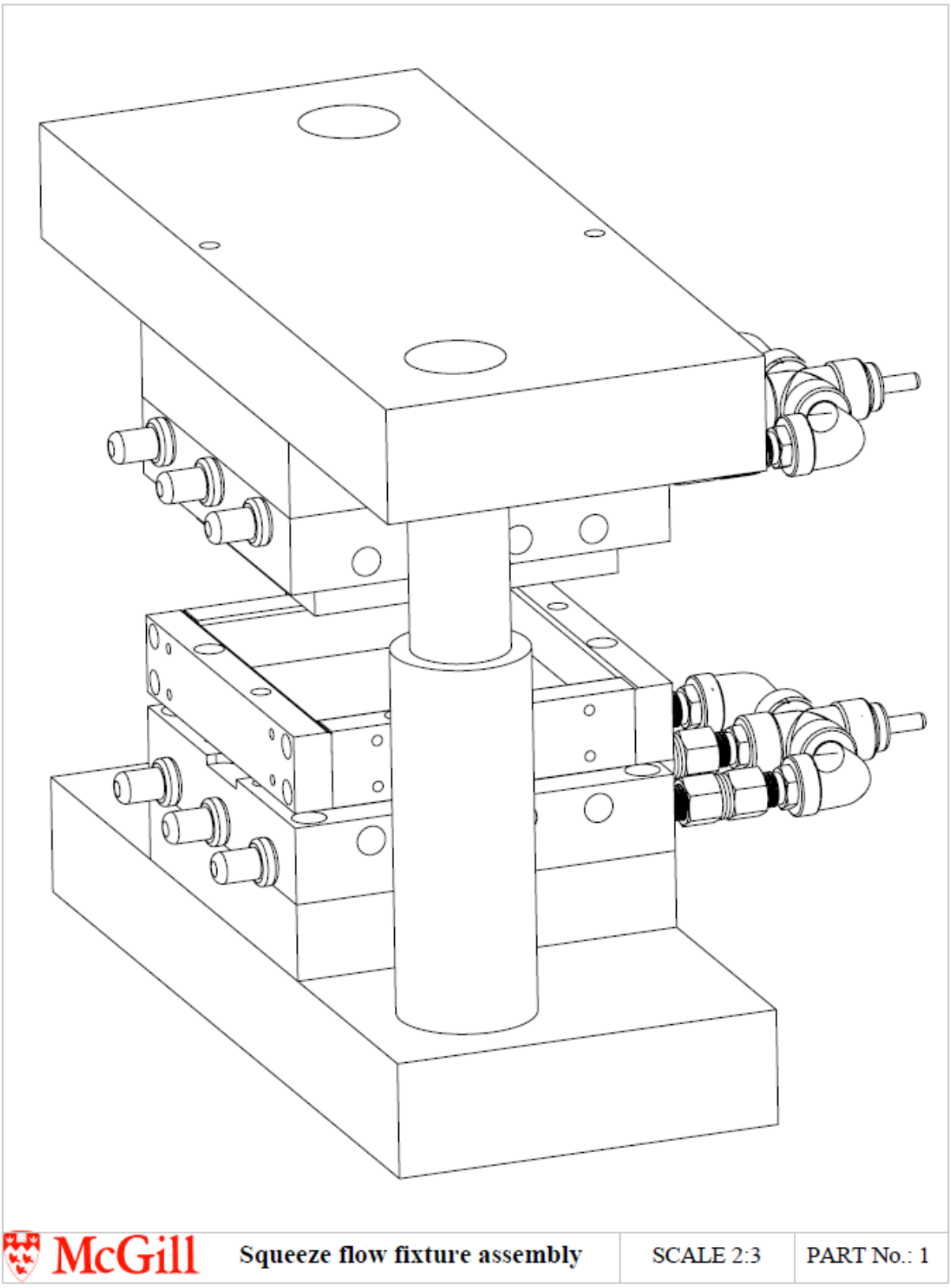

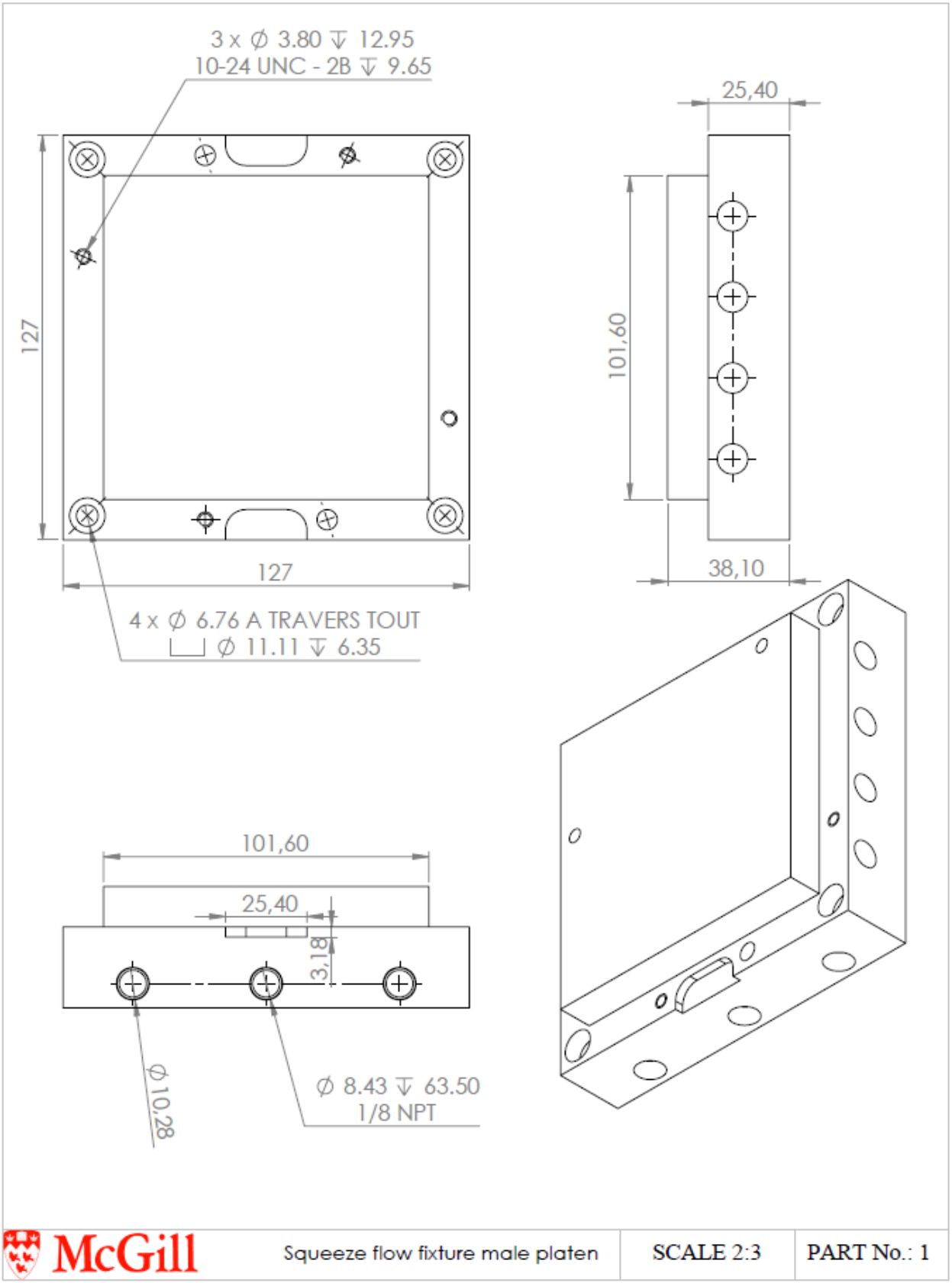
3 x ∅ 3.80 ↧ 12.95
10-24 UNC - 2B ↧ 9.65
25,40
127
101,60
127
38,10
4 x ∅ 6.76 A TRAVERS TOUT
⌴ ∅ 11.11 ↧ 6.35
101,60
25,40
3,18
∅10,28
∅ 8.43 ↧ 63.50
1/8 NPT
McGill
Squeeze flow fixture male platen
SCALE 2:3
PART No.: 1

B.2 Flat panel mould drawing

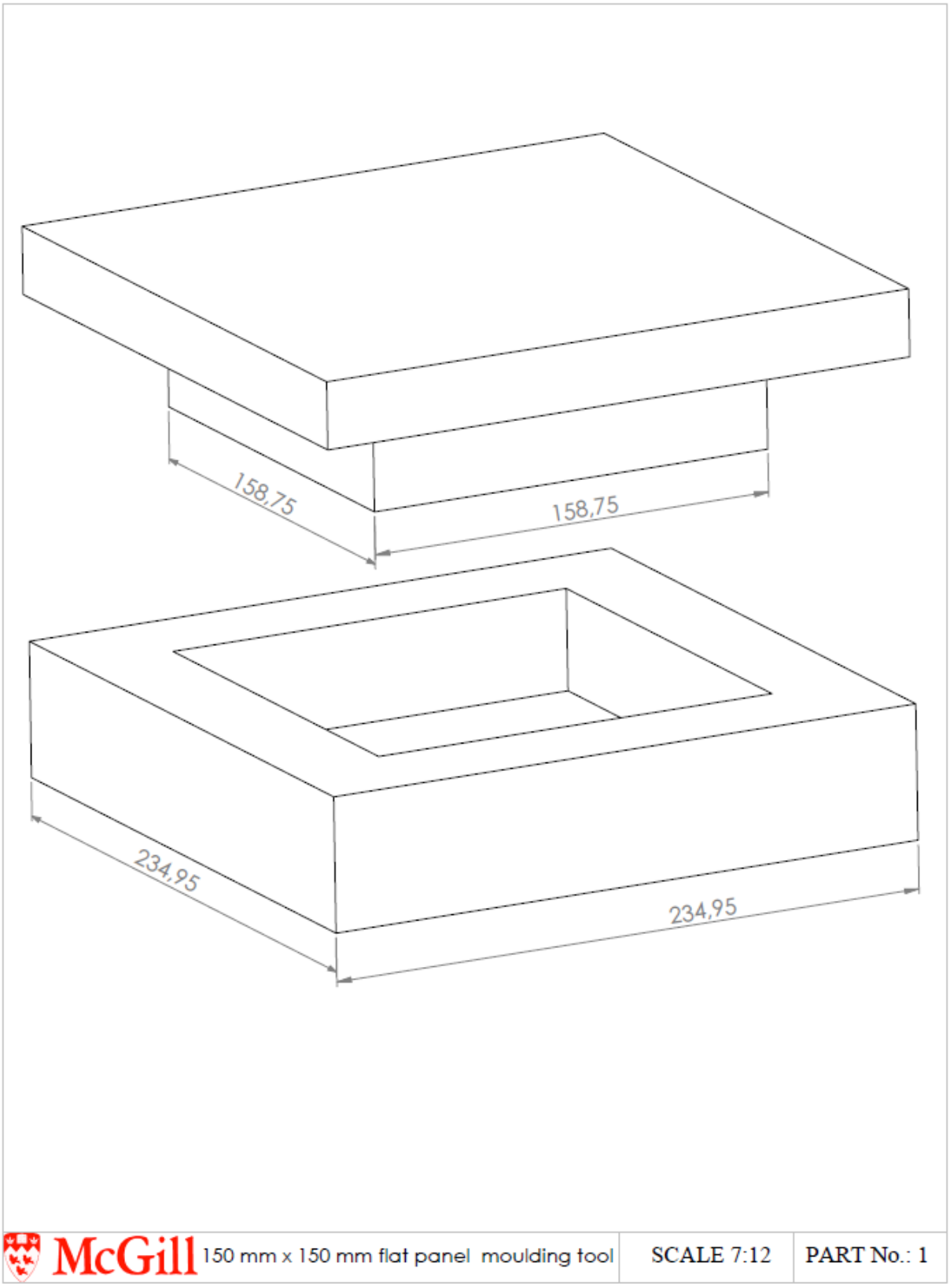

Appendix C - Micro-CT scan and reconstruction procedures

C.1 Experimental apparatus

As shown in Figure B-1, the XTek HMXST 225 computed tomography system consists of a X-ray microtomograph and a control computer. It consists of a secured test chamber and all the necessary hardware. The sample is positioned on a rotating table, inside the test chamber, with a 360° rotation range and 500 mm height range. The X-ray signal is emitted from a high power X-ray tube with a high voltage generator up to 225 kV. The signal is detected on a flat panel detector, which is 40cm by 40cm (or 2000x2000 pixels). It has a minimum resolution of 2µm at maximum magnification (100x).

Figure C-1 : Photograph of the XTek HMXST 225 computed tomography system

C.2 Procedures

The following procedures were used to scan and reconstruct the samples using the XTek HMXST 225 computed tomography system.

C.2.1 Scan

1) The system was powered on, and the XTek software, used for data acquisition, was opened.
2) The X-Ray generator was activated and a pre-heating time of thirty minute was allowed.
3) The ROS samples were mounted on a sample holder using the following configuration (see B-2): Three to six samples were stacked on top of each other and wrapped with duck tape. They were then placed on the sample holder and fixed with adhesive putty.
4) The mounted sample was placed in the scan chamber and fastened on the rotating stage.
5) The Xtek software was used to prepare the scan:
   a) A shading correction was performed to ensure optimal constrats and minimize light and shading effects.
   b) The sample was moved and rotated at 360 in order to ensure that all the sample remains inside the field of view for the full rotation range.
   c) The X-ray voltage and intensity were adjusted to obtain optimal contrast between the silver markers and the material. For all the results presented in this thesis, a voltage of 45kV and an intensity of 347µA were used.
   d) The number of frame per projection (FPP) was set to 4 for all the scans performed in this work. The higher the FPP is, the better the scan quality is, and also the scan time. For the samples tested in this study, 4 FPP gave similar results to 8 FPP and greatly reduced the scan time. Therefore, 4 FPP were used to perform all the scans presented in this thesis.
   e) No filter were used in this study; so, the filter option was set to no filter.
   f) The option "minimise ring artefacts" was set on for every scans. Those ring artefacts appear as a number of concentric rings superimposed on the structures being scanned [92].
6) The scan was started and allowed to complete. The scan time was around 5h for all the samples tested at 4 FPP. The datasets produced were around 20 Gb in average for each scan.

C.2.2 Reconstruction and data analysis

Two software were used to perform the reconstruction and data analysis, CT-Pro and ORS Visual, respectively.

1) The datasets was transferred from the acquisition computer to the reconstruction and data analysis computer.
2) The CT-Pro software was opened on the reconstruction computer and the scanned dataset was selected.
3) A quick look at the first and last slides was done to ensure they were identical. It was the case for all the scans performed. In the case of a major difference between them, due to sample motion during the scan, one would have to scan the sample again or the reconstruction would fail.
4) The software was used to find the center of rotation of the acquired dataset. This operation usually took around 5 to 10 minutes.
5) The region of interest was selected to perform the reconstruction seperately for each samples. Stacking samples prior to perform the scan allowed to perform only one scan for several samples, and reconstruct their dataset separately.
6) The reconstruction was then started, this process took between 5 to 15 minutes depending on the region of interest dimensions and produces 3D datasets of around 2Gb in size, to be analyzed with ORS Visual.
7) ORS Visual was opened and the reconstructed 3D dataset was opened.
8) The contrast was then adjusted to visualize the markers and performed all the analysis presented in this thesis.

Appendix D -Model Initial Values Approximation

In order to help the non-linear solver converging on the first time step, initial values for the velocity field $\vec{U}$ were approximated using the analytical solution obtained for a Newtonian fluid. Considering a two dimensional transverse flow and using the lubrication assumption, as shown in Shuler and Advani [60], one can relate the closure rate $dh(t)/dt$ to the applied load $F(t)$ and the Newtonian viscosity η. W, $h(t)$ and $L(t)$ are respectively the sample width, height and Length.

$$\frac{dh(t)}{dt} = \frac{F(t)}{8\eta W}\frac{h(t)^3}{L(t)^3} \tag{D.1}$$

The velocity field $\vec{U}$ is defined using the following notation for horizontal and vertical components.

$$\vec{U} = \begin{pmatrix} u(x,y) \\ v(x,y) \end{pmatrix} \tag{D.2}$$

The velocity vertical component $v(x,y)$ can directly be expressed as a function of the closure rate $dh(t)/dt$ and the initial sample height h_i.

$$v(x,y) = -\frac{dh(t)}{dt}\frac{y}{h_i} \tag{D.3}$$

Assuming a Newtonian behaviour, the horizontal velocity component $u(x,y)$ can be expressed using the following polynomial form:

$$u(x,y) = x(Ay^2 + By) \tag{D.4}$$

To determine constants A and B one first needs to apply incompressibility:

$$\langle u \rangle_0^{h_i} \times h_i = \frac{dh(t)}{dt} \times L_i \tag{D.5}$$

where $\langle u \rangle_0^{h_i}$ is the average horizontal velocity with respect to the vertical direction y and can be calculated using the following equation.

$$\langle u \rangle_0^{h_i} = L_i \left(\frac{\int_0^{h_0} (Ay^2 + By)dy}{h_i} \right) \tag{D.6}$$

This leads to:

$$\langle u \rangle_0^{h_i} = \frac{L_i}{h_0}\left(\frac{A{h_i}^3}{3} + \frac{B{h_i}^2}{2} \right) \tag{D.7}$$

Using the incompressibility equation one can express the constants as a function of the initial sample height h_i and closure rate $dh(t)/dt$:

$$\frac{Ah_i}{3} + \frac{\mathrm{B}}{2} = \frac{1}{h_i^2}\frac{dh(t)}{dt} \tag{D.8}$$

Moreover, the horizontal velocity being maximum at $y = h_i$, one can write:

$$\frac{\partial u(x,y)}{\partial y}\Big|_{\text{at y} = h_0} = 0 \tag{D.9}$$

Therefore, by first substitution of equation (D.4) into (D.9), and by applying the first order derivative in y, one can obtain:

$$2h_i A + B = 0 \tag{D.10}$$

By substitution of (D.8) into (D.10), one can obtain constants A and B:

$$A = -\frac{3}{2h_i^2}\frac{dh(t)}{dt} \tag{D.11}$$

$$B = \frac{3}{h_i^2}\frac{dh(t)}{dt} \tag{D.12}$$

By substitution of equation (D.11) and (D.12) for constants A, and B, respectively, into equation (D.4), an analytical expression for $u(x,y)$ can be obtained:

$$u(x,y) = \frac{3x}{h_i^2}\frac{dh(t)}{dt}\left(y - \frac{y^2}{2h_i}\right) \tag{D.13}$$

This later equation was used to approximate the initial solution for the horizontal velocity field. This was useful to help the non-linear solver converging on the first time step.

REFERENCES

1. Airbus, A340 carbon composite spoiler made with RTM, in *Composites World*. 2003.

2. V. Brachos, V. Borbone, and G. Robblee. The emergence of thermoplastic composite materials through cost-effective molding techniques. In *Proceedings of the International SAMPE Symposium and Exhibition*, Long Beach, CA, United-States, 2008.

3. P.E. Bourban, *et al.*. Integrated Processing of Thermoplastic Composites. *Composites Science and Technology*, 58:633-637, 1998.

4. J.P. Nunes, *et al.*. New thermoplastic matrix composites for demanding applications. *Plastics, Rubber and Composites*, 38(2-4):167-172, 2009.

5. R.K. Okine, Analysis of Forming Parts from Advanced Thermoplastic Composite Sheet Materials. *Journal of Thermoplastic Composite Materials*, 2:50-76, 1989.

6. N. Tsuji, G.S. Springer, and I. Hegedus. The Drapability of Aligned Discontinuous Fiber Composites. *Journal of Composite Materials*, 31(5):428-465, 1997.

7. M. Tuttle, T. Shifman, and B. Boursier. Simplifying certification of discontinuous composite material forms for primary aircraft structures. In *Proceedings of the International SAMPE conference*, Seattle, WA, USA, 2010.

8. U.K. Vaidya and K.K. Chawla. Processing of fibre reinforced thermoplastic composites. *International Materials Reviews*, 53(4):185-218, 2008.

9. I.Y. Chang and J.F. Pratte. LDF^{TM} Thermoplastic Composites Technology. *Journal of Thermoplastic Composite Materials*, 4:227-252, 1991.

10. C.T. Sun, I. Chung, and I.Y. Chang. Modeling of elastic-plastic behavior of LDF™ and continuous fiber reinforced AS-4/PEKK composites. *Composites Science and Technology*, 43(4):339-345, 1992.

11. P. Feraboli, *et al.*, Characterization of Prepreg-Based Discontinuous Carbon Fiber/Epoxy Systems. *Journal of Reinforced Plastics and Composites*, 28(10):1191-1214, 2008.

12. P. Feraboli, *et al.*, Stochastic laminate analogy for simulating the variability in modulus of discontinuous composite materials. *Composites Part A: Applied Science and Manufacturing*, 41(4):557-570, 2010.

13. M. Selezneva, *et al.* Compression Moulding of Discontinous-fibre Carbon/PEEK composites: study of mechanical properties. In *Proceedings of the SAMPE Conference*. Baltimore, MD, United-States, 2012.

14. G.P. Picher-Martel and P. Hubert. Squeeze flow behavior of Carbon/PEEK randomly oriented strands under transverse compaction. In *Proceedings of the American Society for Composites Conference*. Arlington, TX, United-States, 2012.

15. G.P. Picher-Martel, A. Levy, and P. Hubert. Squeeze flow of Randomly-Oriented Strands thermoplastic composites. In *Proceedings of the 19th International Conference on Composite Materials*, Montréal, Canada, 2013.

16. J. van Wijngaarden, Jongbloed A., and d.V. J. Thermoplastic Compound Compression Molding. In *Proceedings of the SAMPE Conference*. Seattle, WA, United-States, 2010.

17. Greene, Tweed and Aerolia validate thermoplastic aerospace part, In *Composites Worlds Magazine*, 2014.

18. N. Eguèmann, *et al.* Compression Molding of Complex Parts for theAerospaceWith Discontinuous Novel And Recycled Thermoplastic Composite Materials. In *Proceedings of the 19th International Conference on Composite Materials*. Montréal, Canada, 2013.

19. D. LeBlanc, *et al.* Compression molding of complex parts using randomly-oriented strands thermoplastic composites. In *Proceedings of the SAMPE Technical Conference*. Seattle, WA, United-States, 2014.

20. D. Bhattacharyya, ed. *Composite Sheet Forming*. Composite Materials Series, ed. R.B. Pipes. Vol. 11., Elsevier: Newark, 1997.

21. D. Purslow and R. Childs. Autoclave moulding of carbon fibre-reinforced epoxies. *Composites*, 17(2):127-136, 1986.

22. I. Fernández, F. Blas, and M. Frövel. Autoclave forming of thermoplastic composite parts. *Journal of Materials Processing Technology*, 143-144:266-269, 2003.

23. D. Walczyk and C. Munro. Double-diaphragm forming of advanced composite shapes with active tool shape and temperature control. In *Transactions of the North American Manufacturing Research Institution of SME*, 2009.

24. M.A. Zampaloni, F. Pourboghrat, and W.-R. Yu. Stamp Thermo-hydroforming: A New Method for Processing Fiber-reinforced Thermoplastic Composite Sheets. *Journal of Thermoplastic Composite Materials*, 17:31-50, 2004.

25. R.H.W. ten Thije. Finite Element Simulations of Laminated Composite Forming Processes. Thesis. Twente University of Technology, Deventer, The Netherlands, 2007.

26. J. Sun, *et al.* Interply friction of carbon fiber/epoxy prepreg stacks under different processing conditions. *Journal of Composite Materials*, 2013.

27. R.H.W. ten Thije, *et al.* Tool-ply friction in thermoplastic composite forming. *International Journal of Material Forming*, 1(1):953-956, 2008.

28. U. Sachs, *et al.* Friction in Forming of UD Composites. In *Proceedings of the 14th International ESAFORM Conference on Material Forming*, Belfast, Ireland, 2011.

29. R.H.W. ten Thije and R. Akkerman. A multi-layer triangular membrane finite element for the forming simulation of laminated composites. *Composites Part A: Applied Science and Manufacturing*, 40(6-7):739-753, 2009.

30. F.O. Sonmez and H.T. Hahn. Analysis of the On-Line Consolidation Process in Thermoplastic Composite Tape Placement. *Journal of Thermoplastic Composite Materials*, 10(6):543-572, 1997.

31. E.L. Wang and T.G. Gutowski, Laps and gaps in thermoplastic composites processing. *Composites Manufacturing*, 2(2):69-78, 1991.

32. X. Gagné-Brulotte, Aspects of In-situ Consolidation of Thermoplastic Laminates Manufactured by Automated Tape Placement: A Material Deformation Study. (Thesis) *Mechanical Engineering Department*, McGill University, Montreal, Canada, 2012.

33. I.Y. Chang and J.K. Lees, Recent Development in Thermoplastic Composites: A Review of Matrix Systems and Processing Methods. *Journal of Thermoplastic Composite Materials*, 1:277-296, 1988.

34. J. Schuster and K. Friedrich, Fatigue testing of thermoformed bidirectional LDF™-composites. Applied *Composite Materials*, 1(1):55-68, 1994.

35. I. Taketa, T. Okabe, and A. Kitano, Strength improvement in unidirectional arrayed chopped strands with interlaminar toughening. *Composites Part A: Applied Science and Manufacturing*, 40(8):1174-1178, 2009.

36. I. Taketa, *et al.* Flowability of unidirectionally arrayed chopped strands in compression molding. *Composites Part B: Engineering*, 42(6):1764-1769, 2011.

37. P. Feraboli, et al., Notched behavior of prepreg-based discontinuous carbon fiber/epoxy systems. *Composites Part A: Applied Science and Manufacturing*, 40(3):289-299, 2009.

38. P. Feraboli, *et al.* Defect and damage analysis of advanced discontinuous carbon/epoxy composite materials. *Composites Part A: Applied Science and Manufacturing*, 41(7):888-901, 2010.

39. T.L. Greene. Discontinuous Long Fibre Composites for Complex Shape Metal Replacement. In *Proceedings of The Composite and Advanced Materials Exposition (CAMX)*, Orlando, FL, United-States, 2014.

40. M.H. Kilic. A nonlinear 3D micromechanical and structural framework for analysis of discontinuous longfiber thermoplastic composites. In *Proceedings of The Composite and Advanced Materials Exposition (CAMX)*, Orlando, FL, United-States, 2014.

41. J.H. Han, *et al.* Discontinuous Long Fibre vs. Continous Fiber Reinforced Composites in Impact Resistance and Residual Strength after impact. In *Proceedings of The Composites and Advanced Materials Exposition (CAMX)*, Orlando, FL, United-States, 2014.

42. N. Eguèmann. Study on the mechanical behaviour of Carbon fibre reinforced PEEK polymer with a layered discontinuous architecture. Ph.D. Thesis. Université de Franche-Comté, Besançon, France, 2013.

43. M.D. Wakeman, *et al.* Compression moulding of glass and polypropylene composites for optimised macro- and micro- mechanical properties—1 commingled glass and polypropylene. *Composites Science and Technology*, 58(12):1879-1898, 1998.

44. M.D. Wakeman, *et al.* Compression moulding of glass and polypropylene composites for optimised macro- and micro-mechanical properties II. Glass-mat-reinforced thermoplastics. *Composites Science and Technology*, 59(5):709-726, 1999.

45. M.D. Wakeman, *et al.* Compression moulding of glass and polypropylene composites for optimised macro- and micro- mechanical properties 3. Sandwich structures of GMTS and commingled fabrics. *Composites Science and Technology*, 59(8):1153-1167, 1999.

46. M.D. Wakeman, *et al.* Compression moulding of glass and polypropylene composites for optimised macro- and micro-mechanical properties. 4: Technology demonstrator Ð a door cassette structure. *Composites Science and Technology*, 60:1901-1918, 2000.

47. T.A. Osswald and C.L. Tucker. Compression Mold Filling Simulation for Non-Planar Parts. *International Polymer Processing*, 5(2):79-87, 1990.

48. P. Dumont, *et al.* Compression moulding of SMC: In situ experiments, modelling and simulation. *Composites Part A: Applied Science and Manufacturing*, 38:353-358, 2007.

49. S. Le Corre, *et al.* Rheology of highly concentrated planar fiber suspensions. *Journal of Rheology*, 49(5):1029-1058, 2005.

50. M. Sepehr, *et al.* Rheological properties of short fiber model suspensions. *Journal of Rheology*, 48(5):1023-1048, 2004.

51. M. Sepehr, G. Ausias, and P.J. Carreau. Rheological properties of short fiber filled polypropylene in transient shear flow. *Journal of Non-Newtonian Fluid Mechanics*, 123(1):19-32, 2004.

52. S. Toll and J.A.E. Månson, Dynamics of a planar concentrated fiber suspension with non-hydrodynamic interaction. *Journal of Rheology*, 38(4):985-997, 1994.

53. S. Toll and J.A.E. Månson, Elastic Compression of a Fiber Network. *Journal of Applied Mechanics*, 62(1):223-226, 1995.

54. A.C. Caba, A.C. Loos, and R.C. Batra, Fiber–fiber interactions in carbon mat thermoplastics. *Composites Part A: Applied Science and Manufacturing*, 38(2):469-483, 2007.

55. C. Servais, A. Luciani, and J.-A.E. Månson, Fiber–fiber interaction in concentrated suspensions: Dispersed fiber bundles. *Journal of Rheology*, 43(4):1005-1018, 1999.

56. C. Servais, V. Michaud, and J.-A.E. Månson, The packing stress of impregnated fiber mats. *Polymer Composites*, 22(2):298-311, 2001.

57. C. Servais, A. Luciani, and J.-A.E. Månson, Squeeze flow of concentrated long fibre suspensions: experiments and model. *Journal of Non-Newtonian Fluid Mechanics*, 104(2–3):165-184, 2002.

58. R. Luchoo, et al. Macro-scale Modelling of Discontinuous Fiber Composites. In *Proceedings of the 18th International Conference on Composite Materials*, Jeju Island, South Korea, 2011.

59. A. Levy and P. Hubert, Interstrand Void Content evolution in compression molding of Randomly Oriented Strands (ROS) of thermoplastic composites. *Composites Part A: Applied Science and Manufacturing*, (accepted).

60. S.F. Shuler and S.G. Advani, Transverse squeeze flow of concentrated aligned fibers in viscous fluids. *Journal of Non-Newtonian Fluid Mechanics*, 65(1):47-74, 1996.

61. O. Guiraud, *et al.* Rheometry of compression moulded fibre-reinforced polymer composites: Rheology, compressibility, and friction forces with mould surfaces. *Composites Part A: Applied Science and Manufacturing*, 43(11):2107-2119, 2012.

62. R. Akkerman, *et al.* Friction in Textile Thermoplastic Composites Forming. In *Recent Advances in Textile Composites*. 2010.

63. J.L. Gorczyca, *et al.* Modeling of Friction and Shear in Thermostamping of Composites – Part I. *Journal of Composite Materials*, 38(21):1911-1929, 2004.

64. U. Sachs, *et al.* A Friction-Test Benchmark with Twintex PP. *Key Engineering Materials*, 504-506:307-312, 2012.

65. J. Engmann, C. Servais, and A.S. Burbidge. Squeeze flow theory and applications to rheometry: A review. *Journal of Non-Newtonian Fluid Mechanics*, 132(1-3):1-27, 2005

66. R. Balasubramanyam, R.S. Jones, and A.B. Wheeler. Modelling transverse flows of reinforced thermoplastic materials. *Composites*, 20(1):33-37, 1989.

67. J.A. Goshawk, V.P. Navez, and R.S. Jones. Squeezing flow of continuous fibre-reinforced composites. *Journal of Non-Newtonian Fluid Mechanics*,73(3):327-342, 1997.

68. P.J. Carreau. Rheological Equations from Molecular Network Theories. *Transactions of The Society of Rheology*, 16(1):99-127, 1972.

69. D.N. Smyrnaios and J.A. Tsamopoulos. Squeeze flow of Bingham plastics. *Journal of Non-Newtonian Fluid Mechanics*, 100(1–3):165-189, 2001.

70. T.C. Papanastasiou and A.G. Boudouvis. Flows of viscoplastic materials: Models and computations. *Computers & Structures*, 64(1–4):677-694, 1997.

71. T.C. Papanastasiou. Flows of Materials with Yield. *Journal of Rheology*, 31(5):385-404, 1987.

72. E. Mitsoulis. Flows of viscoplastic materials: models and computations. *Rheology reviews*, 135-178, 2007

73. G. Karapetsas and E. Mitsoulis. Some experiences with the slip boundary condition in viscous and viscoelastic flows. *Journal of Non-Newtonian Fluid Mechanics*, 198(0):96-108, 2013.

74. P. Coussot, Yield stress fluid flows: A review of experimental data. *Journal of Non-Newtonian Fluid Mechanics*, 211(0):31-49, 2014.

75. E.C. Bingham. *Fluidity and Plasticity*. 1922, New-York: McGraw-Hill.

76. W.H. Herschel and R. Bulkley. Konsistenzmessungen von Gummi-Benzol-Loesungen. Kolloid Z., 39:291-300, 1926.

77. Casson, N. *Rheology of disperse systems*. 1959: Pergamon Press.

78. S.R. Stock. X-ray microtomography of materials. *International Materials Reviews*, 44(4):141-164, 1999.

79. F. Desplentere, *et al.* Micro-CT characterization of variability in 3D textile architecture. *Composites Science and Technology*, 65(13):1920-1930, 2005.

80. J.S.U. Schell, *et al.* Micro-computed tomography determination of glass fibre reinforced polymer meso-structure. *Composites Science and Technology*, 66(13):2016-2022, 2006.

81. P. Badel, *et al.* Simulation and tomography analysis of textile composite reinforcement deformation at the mesoscopic scale. *International Journal of Material Forming*, 2(1):189-192, 2009.

82. L.P. Djukic, *et al.* Contrast enhancement in visualisation of woven composite architecture using a MicroCT Scanner. Part 2: Tow and preform coatings. *Composites Part A: Applied Science and Manufacturing*, 40(12):1870-1879, 2009.

83. P.J. Schilling, *et al.* X-ray computed microtomography of internal damage in fiber reinforced polymer matrix composites. *Composites Science and Technology*, 65(14):2071-2078, 2005.

84. T. Centea and P. Hubert. Measuring the impregnation of an out-of-autoclave prepreg by micro-CT. *Composites Science and Technology*, 71(5):593-599, 2011.

85. D. LeBlanc. Compression moulding of complex parts using randomly-oriented strand thermoplastic composites. Master's thesis, McGill University, Montréal, Canada, 2014.

86. M. Scaramanga. Design of a Friction Measurement Apparatus for Carbon Fibre Composites. Bachelor Honours Thesis, McGill University, Montréal, Canada, 2013.

87. A.M. Murtagh, J.J. Lennon, and P.J. Mallon. Surface friction effects related to pressforming of continuous fibre thermoplastic composites. *Composites Manufacturing*, 6(3-4):169-175, 1995.

88. A.M. Murtagh, and P.J. Mallon. Chapter 5 Characterisation of shearing and frictional behaviour during sheet forming, In *Composite Materials Series*, p. 163-216, 1997.

89. G.P. Picher-Martel, A. Levy, and P. Hubert. Compression Molding of Carbon/PolyEther Ether Ketone Composites: Squeeze Flow Behavior of Unidirectional and Randomly-Oriented Strands. *Polymer Composites*, (under review).

90. D. LeBlanc, *et al.* Compression moulding of stiffened brackets using randomly-oriented strands thermoplastic composites. In *Proceedings of The Composites and Advanced Materials Exposition (CAMX)*, Orlando, FL, United-States, 2014.

91. A. Levy. and G.P. Picher-Martel. Modeling the Squeeze Flow of a Thermoplastic Composite Tape During Forming. In *Proceedings of the COMSOL Conference*, Boston, MA, United-States, 2012.

92. J.H. Kinney, *et al.* X-ray microtomography on beamline X at SSRL. *Review of Scientific Instruments*, 60(7):2471-2474, 1989.